Multi-Detector CT Imaging Handbook

Multi-Detector CT Imaging

Abdomen, Pelvis, and CAD Applications

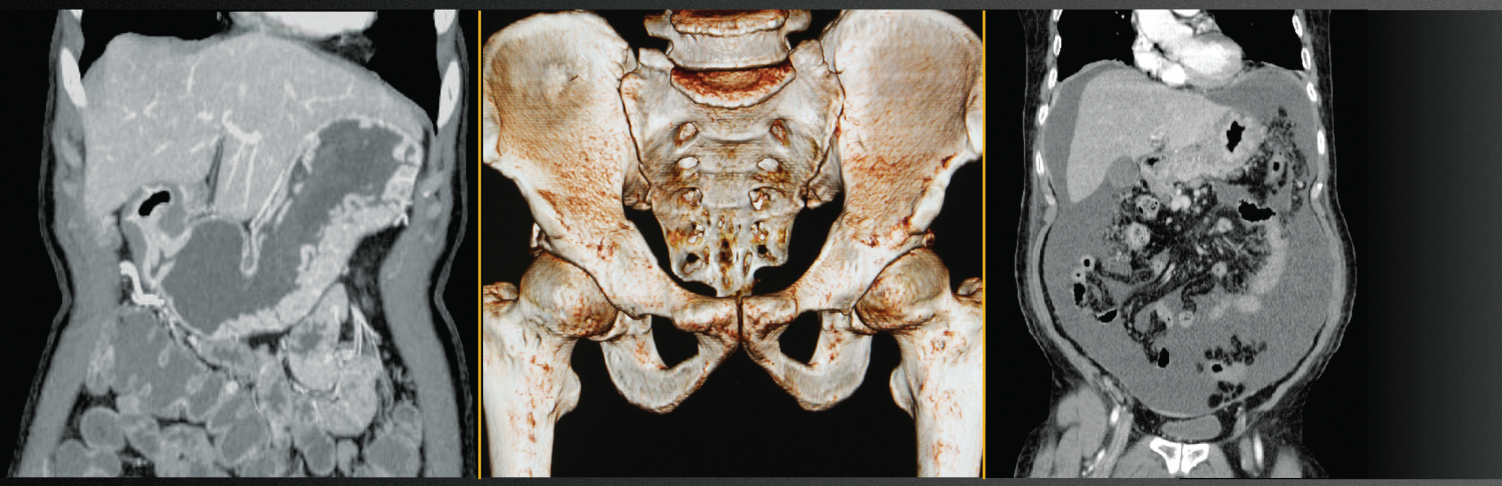

edited by
Luca Saba • Jasjit S. Suri

CRC Press
Taylor & Francis Group

Multi-Detector CT Imaging Handbook

Multi-Detector CT Imaging

Abdomen, Pelvis, and CAD Applications

Multi-Detector CT Imaging Handbook

Multi-Detector CT Imaging: Principles, Head, Neck, and Vascular Systems

Multi-Detector CT Imaging: Abdomen, Pelvis, and CAD Applications

Multi-Detector CT Imaging

Abdomen, Pelvis, and CAD Applications

edited by
Luca Saba • Jasjit S. Suri

CRC Press
Taylor & Francis Group
Boca Raton London New York

CRC Press is an imprint of the
Taylor & Francis Group, an **informa** business

CRC Press
Taylor & Francis Group
6000 Broken Sound Parkway NW, Suite 300
Boca Raton, FL 33487-2742

Version Date: 20130507

International Standard Book Number-13: 978-1-4398-9398-2 (eBook - PDF)

Luca Saba dedicates this book to his parents

Giovanni Saba and Raffaela Polla for their love.

Jasjit S. Suri dedicates this book to his children

Harman Suri and Neha Suri for their love.

Contents

Section III Muscle and Skeleton

Section IV Special Applications

Section V CAD Applications

Foreword

Medical imaging, and computed tomography (CT) in particular, have revolutionized medical care over the past four decades in ways unimaginable prior to the introduction of CT. The impact of CT extends over virtually every clinical field and region of the body, and through all aspects of care including screening, diagnosis and problem solving, monitoring disease progression and treatment responses, and directing minimally invasive procedural interventions. It is no wonder then, with the critical role CT plays, and with the rapid innovations in computer technology, that advances in the capabilities and complexity of CT imaging continue to evolve. An up-to-date complete and authoritative educational and reference volume covering the entire spectrum of CT is a difficult task to accomplish and lacking in the radiology literature. *Multi-Detector CT Imaging*, edited by Dr. Luca Saba and Dr. Jasjit Suri, excels in meeting this need.

Drs. Saba and Suri have brought together an outstanding collection of international authors recognized worldwide as leaders in their fields. Their extensive clinical experience and practical knowledge are logically presented, well organized, and brilliantly visualized. The two books in this set are amazingly complete in content, depth, and quality, yet read easily as an educational introduction or as a reference source.

The value of these books will be appreciated by readers in many ways. They cover all aspects of CT imaging, with technical principles and postprocessing methodologies comprehensibly presented, and extensive clinical specialty chapters easily searchable for specific information without need of an index. The value goes far beyond just a "how-to" or an encyclopedia of findings, however. The authors have uniformly put techniques, clinical findings, pathologic disease presentations, and clinical implications of imaging findings in practical perspective. The organization of the chapters is a wonderful progression that actually follows how the radiologist approaches unknown cases. Most chapters start with a review of imaging techniques for the organ or disease process. This is often followed with a practical discussion reviewing the spectrum of abnormal CT findings and their significance and differential diagnosis, followed subsequently by thorough material organized around understanding disease processes. Helpful correlative material with MRI and PET imaging is frequently presented to illustrate how these modalities complement each other.

This resource is a remarkable tool that will be of value to imaging professionals from every clinical vantage point and will serve well those experienced with CT or those using it to first learn about CT. I personally look forward to using this resource and having it available for our trainees, not only as an essential educational tool, but knowing that it will stimulate our community to further push the frontiers of CT imaging.

Richard L. Baron, MD
Dean for Clinical Practice
Professor of Radiology
University of Chicago Pritzker School of Medicine

Preface

The introduction of multi-detector row computed tomography (CT) in the early 1990s resulted in a fundamental and far-reaching improvement of CT imaging. For the first time, volumes of data could be acquired without misregistration of anatomical details, which indicated the development of 3D image processing techniques. In the last 20 years, CT technology has further improved with the introduction of systems up to 320-detector rows and with the development of dual-source and multispectral technology.

From these developments, the diagnostic potential of CT has impressively improved with an exceptional spatial resolution and the possibility to analyze with an exquisite level of detail several kinds of pathology. Thanks to the development of CT perfusion technique, functional brain imaging as well as liver imaging is now possible.

The purpose of this book is to cover clinical and engineering benefits in the diagnosis of human pathologies. It discusses the protocols and potential of advanced computed tomography scanners, explaining easily, but with an adequate level of detail, the role and potential of CT.

Acknowledgments

It is not possible to overstate our gratitude to the many individuals who helped to produce this book. In particular, Luca Saba would like to thank Professors Giorgio Mallarini and Giancarlo Caddeo, who first taught him the principles of computed tomography. Dr. Saba also thanks Stefano Marcia, Paolo Siotto, and Giovanni Argiolas and his many colleagues, residents, students, and friends for their continuous exchanges during these years. A special thanks also to Carlo Nicola de Cecco for his help. Finally, Dr. Saba would like to acknowledge the patience and understanding displayed by Tiziana throughout his work. Without her continuous encouragement, this book would not have been completed.

Jasjit S. Suri acknowledges Dr. Luca Saba for his continuous dedication in the field of computer tomography imaging and his willingness to participate in successfully launching this project. Dr. Suri also thanks his family, Malvika, Harman, and Neha, who are always a source of shine and laughter. Special thanks to all his friends and collaborators around the world who helped commercialize medical devices and healthcare imaging products over the course of years.

Both editors have received considerable support and cooperation from individuals at CRC/Taylor & Francis, particularly Michael Slaughter, Jessica Vakili, Joette Lynch, Michele Smith and from Dennis Troutman at diacriTech, each of whom helped to minimize the obstacles that the editors encountered.

Editors

Luca Saba earned his MD from the University of Cagliari, Italy, in 2002. Today, he works in the University of Cagliari School of Medicine. His research fields are focused on multi-detector row computed tomography, magnetic resonance, ultrasound, neuroradiology, and diagnostics in vascular sciences.

His works, as lead author, have appeared in more than 100 high impact factor, peer-reviewed journals such as the *American Journal of Neuroradiology*, *European Radiology*, *European Journal of Radiology*, *Acta Radiologica*, *Cardiovascular and Interventional Radiology*, *Journal of Computer Assisted Tomography*, *American Journal of Roentgenology*, *Neuroradiology*, *Clinical Radiology*, *Journal of Cardiovascular Surgery*, and *Cerebrovascular Diseases*. He is a well-known speaker and has spoken over 45 times at national and international levels.

Dr. Saba has won 12 scientific and extracurricular awards during his career. He has presented more than 430 papers and posters at national and international congresses (RSNA, ESGAR, ECR, ISR, AOCR, AINR, JRS, SIRM, AINR). He has written eight book chapters, and he is currently serving as an editor of four books in the field of cardiovascular and neurodegenerative imaging.

He is a member of the Italian Society of Radiology, European Society of Radiology, Radiological Society of North America, American Roentgen Ray Society, and European Society of Neuroradiology.

Jasjit S. Suri earned his MS in neurological MRI from the University of Illinois, a PhD in cardiac imaging from the University of Washington and an MBA from the Weatherhead School of Management, Case Western Reserve University. He has worked as scientist, manager, senior director, vice president, and chief technology officer at IBM, Siemens Medical, Philips Healthcare, Fisher, and Eigen Inc.

He has written over 400 publications, 60 patents, 4 FDA clearances, and more than 25 books in medical imaging and biotechnologies (diagnostic and therapeutic). Dr. Suri has had a leadership role in releasing products in the men's and women's market in the fields of cardiology, neurology, urology, vascular, ophthalmology, and breast cancer.

Dr. Suri has received the President's Gold Medal and Fellow of American Institute of Medical and Biological Engineering from the National Academy of Sciences. He has won over 50 awards during his career. Dr. Suri is also a strategic advisory board member for more than half a dozen industries and international journals focused on biomedical imaging and technologies.

Contributors

Behnoush Abdollahi
BioImaging Laboratory
Bioengineering Department
and
Computer Engineering and Computer Science Department
University of Louisville
Louisville, Kentucky

Mohamed Abou El-Ghar
Urology and Nephrology Department
University of Mansoura
Mansoura, Egypt

Rita Agarwala
Department of Radiology
John H. Stroger Hospital of Cook County
Chicago, Illinois

Hirotaka Akita
Department of Diagnostic Radiology
Keio University School of Medicine
Tokyo, Japan

Luis Guzmán Álvarez
Department of Radiology
Hospital of Traumatology
Granada, Spain

Garyfalia Ampanozi
Institute of Forensic Medicine
University of Zurich
Zurich, Switzerland

J. Dámaso Aquerreta
Servicio de Radiología
Clínica Universidad de Navarra
Navarra, Spain

Davide Bellini
Department of Radiological Sciences, Oncology and Pathology
Sapienza University of Rome—Polo Pontino
Rome, Italy

Jonathan W. Berlin
Department of Radiology
North Shore University Health System
University of Chicago
Evanston Hospital
Evanston, Illinois

Ashu Seith Bhalla
Department of Radiology
All India Institute of Medical Sciences
New Delhi, India

Michael A. Blake
Division of Abdominal Imaging and Interventional Radiology
Massachusetts General Hospital
Boston, Massachusetts

Carlo Catalano
Department of Radiological Sciences
Sapienza University of Rome
Rome, Italy

Heang-Ping Chan
Department of Radiology
University of Michigan
Ann Arbor, Michigan

Ali Cahid Civelek
Radiology Department
School of Medicine
University of Louisville
Louisville, Kentucky

Ian Crosbie
Department of Radiology
Mater Misercordiae University Hospital
Dublin, Ireland

Carlo Nicola De Cecco
Department of Radiological Sciences, Oncology and Pathology
Sapienza University of Rome—Polo Pontino
Rome, Italy
and
Department of Radiology & Radiological Sciences
Medical University of South Carolina
Charleston, South Carolina

Maurizio Del Monte
Department of Radiological Sciences
Sapienza University of Rome
Rome, Italy

Michele DiMartino
Department of Radiological Sciences
Sapienza University of Rome
Rome, Italy

Rossella DiMiscio
Department of Radiological Sciences
Sapienza University of Rome
Rome, Italy

Lars C. Ebert
Institute of Forensic Medicine
University of Zurich
Zurich, Switzerland

Ayman El-Baz
BioImaging Laboratory
Bioengineering Department
University of Louisville
Louisville, Kentucky

Jorge Elias Jr.
Abdominal Imaging Section
University of Sao Paulo at Ribeirao Preto School of Medicine
Ribeirao Preto, Brazil

Ahmed Elnakib
BioImaging Laboratory
Bioengineering Department
University of Louisville
Louisville, Kentucky

Robert Falk
Medical Imaging Division
Jewish Hospital
Louisville, Kentucky

Elliot K. Fishman
Department of Radiology
Johns Hopkins University School of Medicine
Baltimore, Maryland

Patricia M. Flach
Institute of Forensic Medicine
University of Zurich
and
Institute of Diagnostic and Interventional Radiology
University Hospital Zurich
Zurich, Switzerland

Thomas Flohr
Siemens Healthcare Computed Tomography
Forchheim, Germany

and

Institute for Diagnostic Radiology
Eberhard Karls University Tübingen
Tübingen, Germany

Jurgen J. Fütterer
Department of Radiology
Radboud University Nijmegen Medical Centre
Nijmegen, the Netherlands

María del Mar Castellano García
Department of Radiology
Hospital of Traumatology
Granada, Spain

Daniel Gieger
Department of Radiological Sciences
Sapienza University of Rome
Rome, Italy

Georgy Gimel'farb
Department of Computer Science
University of Auckland
Auckland, New Zealand

Ajit H. Goenka
Imaging Institute
Cleveland Clinic
Cleveland, Ohio

Richard M. Gore
Department of Radiology
North Shore University Health System
University of Chicago
Evanston Hospital
Evanston, Illinois

Ali Guermazi
Department of Radiology
Boston University School of Medicine
Boston, Massachusetts

Pankaj Gupta
Department of Radiology
All India Institute of Medical Sciences
New Delhi, India

Lubomir Hadjiiski
Department of Radiology
University of Michigan
Ann Arbor, Michigan

Daichi Hayashi
Boston University School of Medicine
Boston, Massachusetts

Matthew T. Heller
Division of Abdominal Imaging
University of Pittsburgh Medical Center
Pittsburgh, Pennsylvania

Franco Iafrate
Department of Radiological Sciences, Oncology and Pathology
Sapienza University of Rome—Polo Pontino
Rome, Italy

Mohamed Jarraya
Department of Radiology
Boston University School of Medicine
Boston, Massachusetts

R. Brooke Jeffrey
Department of Radiology
Stanford University Medical Center
Stanford, California

Masahiro Jinzaki
Department of Diagnostic Radiology
Keio University School of Medicine
Tokyo, Japan

Satomi Kawamoto
Department of Radiology
Johns Hopkins University School of Medicine
Baltimore, Maryland

Eiji Kikuchi
Department of Urology
Keio University School of Medicine
Tokyo, Japan

Karin Knesaurek
Department of Radiology
Division of Nuclear Medicine
Mount Sinai School of Medicine
New York, New York

Lale Kostakoglu
Department of Radiology
Division of Nuclear Medicine
Mount Sinai School of Medicine
New York, New York

Sachio Kuribayashi
Department of Diagnostic Radiology
Keio University School of Medicine
Tokyo, Japan

Andrea Laghi
Department of Radiological Sciences, Oncology and Pathology
Sapienza University of Rome—Polo Pontino
Rome, Italy

Katherine Leung
Department of Radiology and Diagnostic Imaging
University of Alberta
Edmonton, Alberta, Canada

Xiao-Feng Li
Radiology Department
School of Medicine
University of Louisville
Louisville, Kentucky

Concetta Lombardo
Department of Radiological Sciences
Sapienza University of Rome
Rome, Italy

Gavin Low
Department of Radiology and Diagnostic Imaging
University of Alberta
Edmonton, Alberta, Canada

Fabiano Lucchesi
Radiology Department
Barretos Cancer Hospital
Barretos, Brazil

John E. Madewell
Department of Diagnostic Radiology
University of Texas MD Anderson Cancer Center
Houston, Texas

Joaquín Martín
Sección de Radiología
Hospital Reina Sofía de Tudela
Navarra, Spain

Shaunagh McDermott
Division of Abdominal Imaging and Interventional Radiology
Massachusetts General Hospital
Boston, Massachusetts

Uday K. Mehta
Department of Radiology
North Shore University Health System
University of Chicago
Evanston Hospital
Evanston, Illinois

José M. Mellado
Sección de Radiología
Hospital Reina Sofía de Tudela
Navarra, Spain

Valdair Muglia
Abdominal Imaging Section
University of Sao Paulo at Ribeirao Preto School of Medicine
Ribeirao Preto, Brazil

Giuseppe Muscogiuri
Department of Radiological Sciences, Oncology and Pathology
Sapienza University of Rome—Polo Pontino
Rome, Italy

Geraldine M. Newmark
Department of Radiology
North Shore University Health System
University of Chicago
Evanston Hospital
Evanston, Illinois

Owen J. O'Connor
Division of Abdominal Imaging and Interventional Radiology
Massachusetts General Hospital
Boston, Massachusetts

Paul O'Sullivan
Department of Diagnostic Imaging
Bons Secours Hospital
Cork, Ireland

Evangelos N. Perdikakis
Department of Radiology
412 General Military Hospital
212 Mobile Army Surgical Hospital
Xanthi, Greece

Jonelle M. Petscavage-Thomas
Department of Radiology
Penn State Milton S. Hershey Medical Center
Hershey, Pennsylvania

Laura Pérez del Palomar
Servicio de Radiología
Hospital Royo Villanova
Zaragoza, Spain

Mark Pisaneschi
Department of Radiology
John H. Stroger Hospital of Cook County
Chicago, Illinois

Prabhakar Rajiah
Cardiovascular Imaging Laboratory
Cleveland Clinic
Cleveland, Ohio

Erick M. Remer
Imaging Institute
Cleveland Clinic
Cleveland, Ohio

Marco Rengo
Department of Radiological Sciences, Oncology and Pathology
Sapienza University of Rome—Polo Pontino
Rome, Italy

Pedram Rezai
Department of Radiology
John H. Stroger Hospital of Cook County
Chicago, Illinois

Frank Roemer
Department of Radiology,
University of Erlangen
Erlangen Germany

and

Department of Radiology
Boston University School of Medicine
Boston, Massachusetts

Fernando Ruiz Santiago
Department of Radiology
Hospital of Traumatology
Granada, Spain

Bernhard Schmidt
Siemens Healthcare Computed Tomography
Forchheim, Germany

Amar B. Shah
Department of Radiology
New York Medical College
Valhalla, New York

Shetal N. Shah
Imaging Institute
Cleveland Clinic
Cleveland, Ohio

Martin J. Shelly
Division of Abdominal Imaging and Interventional Radiology
Massachusetts General Hospital
Boston, Massachusetts

Robert I. Silvers
Department of Radiology
North Shore University Health System
University of Chicago
Evanston Hospital
Evanston, Illinois

Susana Solanas
Sección de Radiología
Hospital Reina Sofía de Tudela
Navarra, Spain

Erich Sorantin
Division of Paediatric Radiology
Department of Radiology
Medical University of Graz
Graz, Austria

Kalyanasundaram Srinivasan
Department of Radiology
All India Institute of Medical Sciences
New Delhi, India

Damien L. Stella
Department of Radiology
University of Melbourne
Royal Melbourne Hospital
Melbourne, Australia

Jasjit S. Suri
Biomedical Technologies, Inc.
Roseville, California

Kiran H. Thakrar
Department of Radiology
North Shore University Health System
University of Chicago
Evanston Hospital
Evanston, Illinois

Michael J. Thali
Institute of Forensic Medicine
University of Zurich
Zurich, Switzerland

Diana Tran
Department of Radiology
Bankstown Hospital
Sydney, Australia

Sabine Weissensteiner
Division of Paediatric Radiology
Department of Radiology
Medical University of Graz
Graz, Austria

Daniel R. Wenzke
Department of Radiology
North Shore University Health System
University of Chicago
Evanston Hospital
Evanston, Illinois

Minoru Yamada
Department of Diagnostic Radiology
Keio University School of Medicine
Tokyo, Japan

Yoshitake Yamada
Department of Diagnostic Radiology
Keio University School of Medicine
Tokyo, Japan

Section I

Gastro-Intestinal and Abdomen

1

Liver

Michele DiMartino, Rossella DiMiscio, Daniel Gieger, Maurizio Del Monte, Concetta Lombardo, and Carlo Catalano

CONTENTS

1.1 Introduction

Hepatic imaging is an important component of abdominal computed tomography (CT) examination and is crucial for a wide range of clinical applications: detection and characterization of primary or metastatic hepatic lesions, diagnosis of diffuse liver diseases, assessment of vascular and biliary patency or obstruction, tumor staging, monitoring treatment response, and pre- and postoperative evaluation for surgical resection. The introduction in clinical practice of multi-detector computed tomography (MDCT) from four detector row through 64 and more significantly improves the role of CT in the evaluation of liver disease. The main advantages of MDCT are the routine use of thinner sections that yield higher spatial resolution and decrease of gantry rotation time, which result in a significant reduced scan time. Reducing acquisition scan time makes it possible to acquire the entire liver volume with a multiphasic CT protocol during different vascular phases in a single, comfortable, breath hold. Sixteen and more slice CT scanners allow the acquisition of datasets of images with nearly isotropic voxels for multiplanar reconstruction, useful for a better evaluation of liver disease. In this chapter, we discuss the segmental and vascular anatomy of the live, technical parameters, contrast media application, and acquisition protocol of liver examination. In addition, CT imaging findings of main focal and diffuse liver disease are reviewed.

1.2 Liver Anatomy

The knowledge of segmental liver is useful for communicating the CT findings to the surgeon. The system proposed by Coinaud [1–2] and later modified by Bismuth provides the details needed for surgery and is easily applicable to axial imaging techniques such as CT, magnetic resonance imaging and ultrasound. The liver is divided into eight segments, except the caudate lobe and medial segment of the left lobe, segments are defined not only by the three vertical fissures described by the three major hepatic veins, but also by a transverse plane through the left and right portal-venous branches. The segment I is the caudate lobe, segments II–VIII are numbered clockwise looking at the liver ventrally (Figure 1.1). Each segment has an independent blood supply and biliary drainage. The amendment made by Bismuth IV divides the segment into subsegments higher (IVa) and lower (IVb).

The most common anatomic variation is the Riedel lobe, which is an extended, tongue-like, right lobe of the liver. It is not pathological; it is a normal anatomical variant and may extend into the pelvis. It is often mistaken for a distended gallbladder or liver tumor.

A liver located on the left is found in a full or partial situs viscerum inversus.

1.3 Vascular Anatomy and Variants

The hepatic artery carries only 25%–30% of the blood, which is related to the liver.

The common hepatic artery usually originates from the celiac trunk. After gastroduodenal artery originated behind the pylorus, it becomes the proper hepatic artery, which passes into the hepatoduodenal ligament to the anteromedial portal vein and anterior to the bile duct. At hepatic hilum, it divides into left and right branch. The middle hepatic artery that supplies the segment IV with equal frequency originates from the left or right hepatic artery (Figure 1.2).

The classical distribution of the hepatic arteries is only slightly more than half of the subjects, whereas 45% have one or more variants. The most common variants include the left hepatic branch that originates from the left gastric artery (10%–25%) (Figure 1.3) and the right hepatic branch that originates from the superior mesenteric artery (11%–17%) (Figure 1.4).

The Michel classification of hepatic artery variant anatomy is shown in Table 1.1 [3].

The portal vein divides at the hilum into two branches, right and left, which run next to the hepatic arteries and the bile ducts.

In the parenchyma of the right lobe, the right portal vein divides into anterior and posterior branches, which go to the corresponding liver segments (Figure 1.5).

The portal system can be affected by anatomical variants, such as the trifurcation of the portal vein hilum (8%–10%), other anomalies can be also recognized including agenesis or atrophy of one of the two main branches, with atrophy of the liver parenchyma (Figure 1.6).

In the classic anatomy, three main hepatic veins drain into the inferior vena cava (IVC) the left hepatic vein drains segment II and III, the middle hepatic vein drains segment IV, V, and VIII, and the right hepatic vein drains V, VI, and VII. In approximately 60% of the population, the middle and left hepatic veins join to form a common trunk (Figure 1.7).

The most common variant seen is an accessory right hepatic vein draining the segment VI directly into the IVC (Figure 1.8) [4].

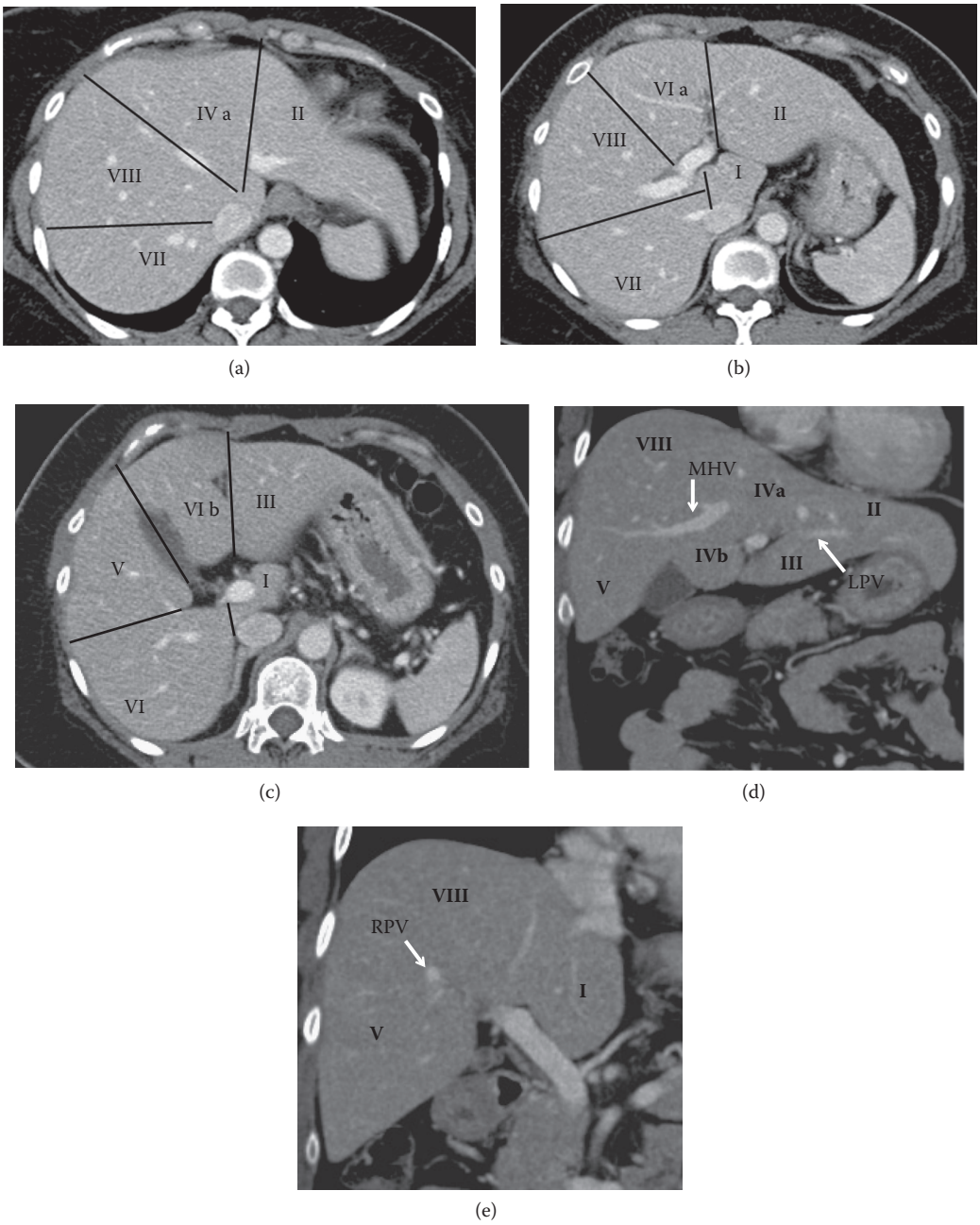

FIGURE 1.1
Segmental anatomy. (a–c) CT axial images show liver segment distribution according to the anatomic segmentation schemes of Couinaud and Bismuth. Falciform ligament plane separates medial (IV segment) from lateral (II—III segments) left lobe. Segmental anatomy. (d and e) CT coronal images show liver segment distribution according to the anatomic segmentation schemes of Couinaud and Bismuth.

1.4 Acquisition Parameters

As the number of detector channels increases, application of thin collimation has become a routine part of MDCT. The minimum section collimation of 16-, 32-, and 64-slice scanners range between 0.5 and 0.625 mm. This submillimeter feature allows for isotropic data acquisition. An isotropic voxel is cubic, having equal dimensions in the *x*-, *y*-, and *z*-axes. Since the *x*- and *y*-axes are determined by both field of view (FOV) and matrix size, isotropic voxel can be acquired only when slice thickness z-axis measures 0.75 mm or less. The major advantage of these nearly isotropic datasets is the ability to reformat images in multiplanar manner, with spatial resolution similar to that of axial images. Recent studies have shown the usefulness of multiplanar reformatted images in the detection of hepatocellular

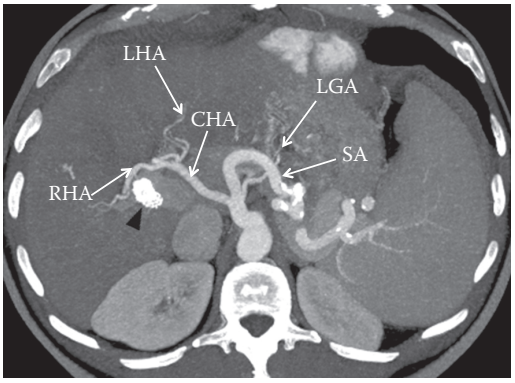

FIGURE 1.2
Normal hepatic arterial anatomy. Axial MIP image shows the normal anatomy of the hepatic artery: common hepatic artery (CHA), left hepatic artery (LHA), right hepatic artery (RHA), superior mesenteric artery (SMA), and splenic artery (SA). Note the presence of transjugular intrahepatic portosystemic shunt (TIPS) in patients with portal hypertension (arrowhead).

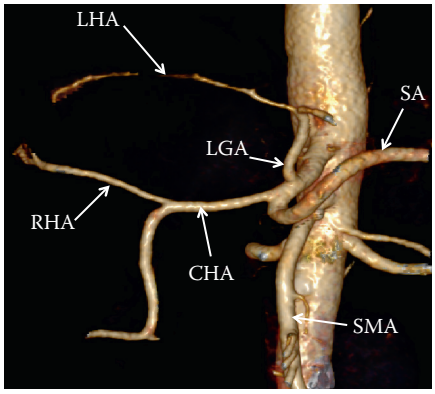

FIGURE 1.3
Variant hepatic arterial anatomy. Three-dimensional (3D) volume-rendered image from a multi-detector CT (MDCT) shows the left hepatic artery (LHA) arising from the left gastric artery (LGA). SA = splenic artery, CHA = common hepatic artery, SMA = superior mesenteric artery, RHA = right hepatic artery.

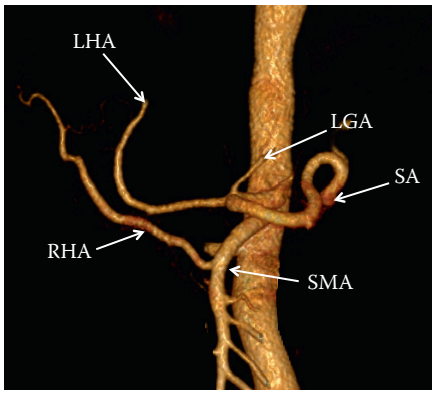

FIGURE 1.4
Variant hepatic arterial anatomy. Three-dimensional volume-rendered image from MDCT shows the right hepatic artery (RHA) arising from superior mesenteric artery (SMA). LGA = left gastric artery, LHA = left hepatic artery, SA = splenic artery.

TABLE 1.1

Hepatic Arterial Variants According to the Michel Classification

Type	Frequency	Description
I	55	RHA, MHA, and LHA arise from the CHA
II	10	RHA, MHA, and LHA arise from the CHA; replaced LHA from the LGA
III	11	RHA and MHA arise from the CHA; replaced RHA from the SMA
IV	1	Replaced RHA and LHA
V	8	RHA, MHA, and LHA arise from the CHA; accessory LHA from the LGA
VI	7	RHA, MHA, and LHA arise from the CHA; accessory RHA
VII	1	Accessory RHA and LHA
VIII	4	Replaced RHA and accessory LHA or replaced LHA and accessory RHA
IX	4.5	Entire hepatic trunk arise from the SMA
X	0.5	Entire hepatic trunk arise from the LGA

CHA = common hepatic artery, RHA = right hepatic artery, LHA = left hepatic artery, MHA = middle hepatic artery, SMA = superior mesenteric artery, LGA = left gastric artery.

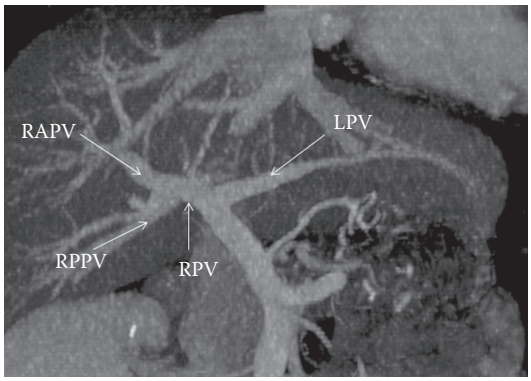

FIGURE 1.5
Normal portal vein (PV) anatomy. Coronal MIP image shows the PV branching into the left PV (LPV) and right PV. The latter divides into the right anterior (RAPV) and right posterior (RPPV) PV.

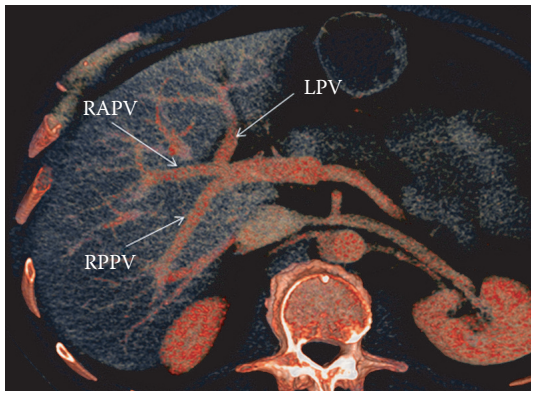

FIGURE 1.6
Portal vein (PV) trifurcation. 3D volume rendered (VR) from CT postcontrast image shows trifurcation of the PV into right anterior (RAPV), right posterior portal vein (RPPV), and left portal vein (LPV).

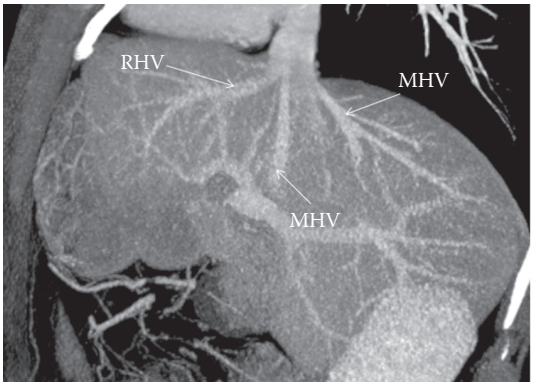

FIGURE 1.7
Normal hepatic veins anatomy. Coronal MIP image shows the confluence into inferior vena cava of the left hepatic vein (LHV), middle hepatic vein (MHV), and right hepatic vein (RHV).

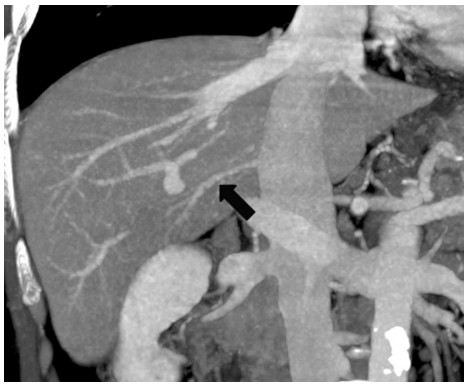

FIGURE 1.8
Accessory hepatic vein. Maximum intensity projection (MIP) from CT postcontrast image shows the presence of an accessory inferior right hepatic veinc (RHV) draining the VI segment directly into the inferior vena cava (IVC).

carcinoma (HCC) [5–6]. Owing to increased spatial resolution and reduced partial volume averaging, thinner-slice collimation also results in an improved ability to detect small hepatic lesion. However, no improvement in lesion detection was found with a collimation width less than 2.5 mm. Furthermore, hepatic imaging with thinner sections caused an increase in image noise, with significantly lower performance in the detection of hepatic lesions [7].

The typical acquisition parameters for liver MDCT are summarized in Table 1.2.

1.5 Contrast Administration

Contrast enhancement of the liver is affected by numerous factors, such as contrast medium volume and concentration, rate and type of injection, scan delay time, and body weight [8–10]. The magnitude of hepatic parenchymal enhancement is directly and almost linearly related to the amount of total iodine mass administered (i.e., total contrast medium volume times concentration) [11–12]. The most important patient-related factor affecting the magnitude of hepatic enhancement is body weight, which shows a near-linear inverse relationship with the magnitude of enhancement: as body weight increases, the magnitude of hepatic parenchymal enhancement decreases. Therefore, when imaging large patients, the total iodine load should be increased to achieve a constant degree of hepatic enhancement. The iodine load can be increased by increasing the contrast medium concentration or volume or injection rate [13–14].

Insufficient hepatic parenchymal enhancement results in diminished conspicuity of a lesion [12]. With MDCT, 50 HU is commonly considered to be a diagnostically appropriate level of hepatic phase enhancement at abdominal CT. Iodine mass required to achieve this enhancement can be estimated by considering patient weight (i.e., maximum hepatic enhancement of 96 HU ± 19 per gram of iodine per kilogram of body weight). This suggests that approximately 0.5 g of iodine per kilogram is needed to achieve the maximum hepatic enhancement of 50 HU (35 g of iodine for a 70-kg patient). For routine abdominal CT (scanning at the portal-venout phase only), injection rates of 3 mL/s are sufficient. Improved lesion-to-liver contrast may be obtained either by a faster injection rate (e.g., 4–6 mL/s) or by an increased iodine concentration. Fast injections increase the magnitude of arterial enhancement and contribute to the increased separation (both time and magnitude) between the arterial and hepatic parenchymal enhancement phases. As a result, fast injections are desirable for multiphase hepatic imaging and the detection of hypervascular liver masses.

Abdominal and hepatic CT imaging has been commonly performed with a fixed-rate injection protocol regardless of the patient's weight [12–14]. This protocol, however, results in inconsistent degrees of contrast enhancement in patients of varying body sizes. This limitation can be overcome by use of contrast material injection protocol, having a fixed injection duration but with individually weight-adapted injection rates. The fixed injection duration protocol facilitates the achievement of consistent arterial and hepatic enhancements and the standardization of scan timing, and perhaps improves the depiction of hypervascular HCCs [15–17]. Iodine dose adjusted to patient weight of 0.5 g of iodine per kilogram injected over 25–30 seconds seems appropriate for dual-phase hepatic CT imaging, resulting in aortic enhancements of more than 250 HU and hepatic enhancements of 50 HU [17]. This protocol involves adjusting the iodine dose and injection rate to the patient's body weight

TABLE 1.2

MDCT Acquisition Parameters for Liver Examination

	4-slice MDCT	16-slice MDCT	64-slice MDCT
Detector configuration (mm)	4 × 1.5/1	16 × 1.5/0.7	64 × 0.625
kVp	120	120	120
Effective mAs	165	180	240[a]
Reconstruction algorithm	Soft tissue (B 30f)	Soft tissue (B 20f)	Soft tissue (B 20f)
Slice thickness (mm)	3 mm	3 mm	3 mm
Pitch	1.5	0.9	0.9
Rotation time (s)	0.5	0.5	0.5
Table speed (mm/rotation)	12.5	22/11	17.3

[a] By using CARE dose system Scan parameters using 4-, 16, and 64 slice MDCT (developed for Siemens scanner).

while fixing the total duration of the injection (e.g., for a 70-kg patient, 100 mL of 350 mg of iodine per milliliter of contrast material injected at 4 mL/s for 25 seconds). The recent development of double-syringe mechanical power injectors simplified the saline flush technique. Immediate injection of a saline bolus after contrast agent administration has been shown to increase the efficiency of contrast medium use by avoiding dispersion of contrast material within the injection tubing and venous system [18].

1.6 CT Protocol

The increasing speed of MDCT scanners has improved the ability to perform multiphasic examinations of the liver. Before contrast medium administration, the acquisition of precontrast scan is useful and recommended. First of all it is helpful to distinguish fluid lesions from solid tumors; moreover it is indicated for the diagnosis of acute hemorrhage of the liver, the valuation of diffuse liver disease (steatosis, hemochromatosis, detection and calcification of hepatic calcification (calcified metastases, hydatid cysts). Contrast-enhanced MDCT of the liver is regulated by a dual blood supply (75% from the portal vein and 25% from the hepatic artery), resulting in various phase enhancement. Following an intravenous bolus of contrast material, the hepatic artery enhances first approximately 15 seconds and reaches peak attenuation at 30 seconds. The contrast agent returns to the liver from the intraperitoneal organs through the portal system after 30 seconds. Liver parenchyma peak enhancement range from 60 to 70 seconds. The equilibrium phase, when the contrast agent is equally divided between intra- and extracellular space, occurs after almost 3 minutes. According to the different enhancement curves of the hepatic artery, portal vein, and hepatic parenchyma, four phases can be distinguished: early arterial, late arterial, portal venous, and delayed (Figure 1.9).

The early arterial phase begins with the arrival of contrast medium in the hepatic artery and ends before portal vein enhancement. The diagnostically useful early arterial phase with sufficient contrast enhancement begins 5–10 seconds after aortic contrast material arrival. The early arterial phase is useful primarily for angiographic imaging of abdominal arterial anatomy and is infrequently obtained for a diagnostic purpose. The late arterial phase is the preferred imaging phase for detecting hypervascular primary or metastatic neoplasms [19–23]. During this phase, hypervascular hepatic lesions enhance maximally, whereas hepatic parenchyma remains relatively unenhanced, commensurate with the relatively small contribution of the hepatic artery to the total hepatic blood supply. The acquisition of images during two arterial contrast phases does not seem to provide additional benefit for the detection of hypervascular focal liver lesion, so late arterial phase alone could be sufficient to reach this topic.

Portal-venous phase started after 60–70 seconds after contrast material injection, when the liver parenchyma reaches its peak enhancement. This phase is useful to well delineate portal and hepatic veins and bile ducts dilatation. Hypovascular tumors are well detected on this phase because of the maximum difference in liver-to-lesion contrast.

Delayed phase (or equilibrium) appears approximately after 180 seconds postcontrast agent administration, when the contrast diffuses into the liver parenchyma and the difference attenuation between vessels and liver parenchyma is minimal. Delayed imaging phase is useful for detecting and characterizing HCCs [24] and for characterizing cholangiocarcinoma (CCC) [25]. During this phase, HCCs typically appear as hypoattenuating, whereas CCCs often show delayed contrast enhancement relative to the background hepatic parenchyma.

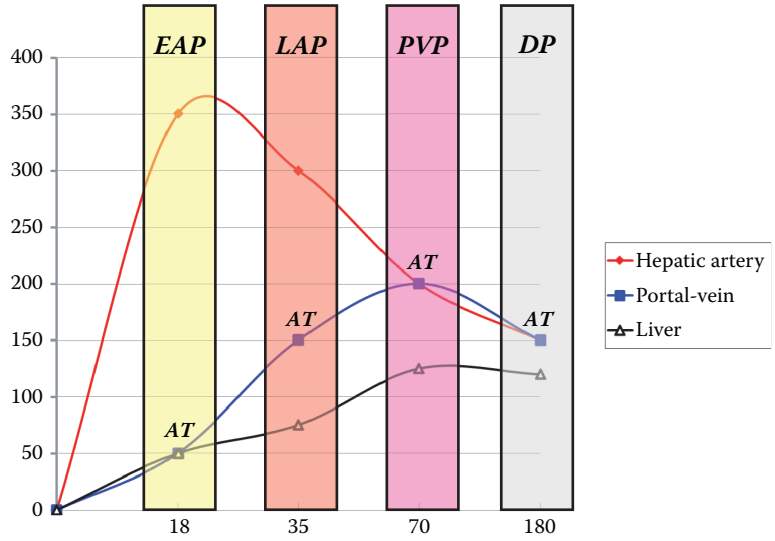

FIGURE 1.9
Different enhancement of hepatic artery, portal vein, and liver parenchyma after contrast medium administration and relative acquisition time of four different vascular phases. EAP = early arterial phase, LAP = late arterial phase, PVP = portal-venous phase, DP = delayed phase AT = acquisition time.

1.7 Reconstruction Parameters

As previously described, with the adventure of 16-slice and more scanners, it became possible to acquire images with a resolution of 1 mm or less, resulting in a nearly isotropic dataset. This three-dimensional (3D) volume can be used for two-dimensional (2D) or 3D post-processing. The most important techniques adopted for liver imaging are multiplanar reformation (MPR), maximum intensity projection (MIP), minimum intensity projection, and volume rendering (VR) [18].

MPR, representing a 2D reformatted plane other than the axial plane, is used to better visualize anatomic and pathologic findings (Figure 1.1a–e).

MIP is routinely used to evaluate hepatic arteries, portal vein and hepatic veins, since the projections display the greatest attenuation difference between vessels and adjacent tissue (Figure 1.2).

The VR technique allows the user to view the entire volume dataset in an appropriate 3D context, including a range type of abdominal tissue. These images are well appreciated by surgeons, since they offer true 3D view of vascular anatomy (Figures 1.3 and 1.4)

1.8 Dual-Energy CT

Dual-energy CT (DECT) is a novel CT technique that is becoming available in most advanced referral diagnostic units and it implies the application of two different energies to add, to the classic single energy MDCT study, information yielded from material differentiation because of the interaction between tissues and different energy levels [26]. DECTs deliver the two energy spectra by a dual tube configuration working at different voltages with intersecting radiation beams or by a single tube able of fast voltage switching. DECT is presently offered by major vendors and is transitioning from first generation apparatuses to second generation ones. Latest generation models overcome some limitations of the first-generations ones; for example, some of the earlier models had smaller FOV of the lower energy tube. As a matter of fact, from first experimental applications in the early 80s, DECT has undergone major technical advances in combination to CT technologic improvements [27,28], that made it suitable for the abdominal region investigation [29–32]. The application of this technique in liver CT imaging, although still under investigation, already showed advantages in the clinical setting.

DECT of the liver (Figure 1.10) can be considered as an interesting strategy to reduce radiation dose delivery to the patients, suitable especially in liver diseased populations undergoing multiple exams because of liver chronic illnesses. This concept is fundamental in a clinical scenario where cumulative exposure from CT ionized radiation is increasing [33] and reduction of patient dose delivery is a mandatory issue [34] to improve patient safety [35]. Dose reduction from DECT can be achieved by taking advantage of the possibility of virtual noncontrast (VNC) images (Figure 1.11) generation from a dual-energy acquired dataset applying a specific three-point algorithm that differentiates soft tissues,

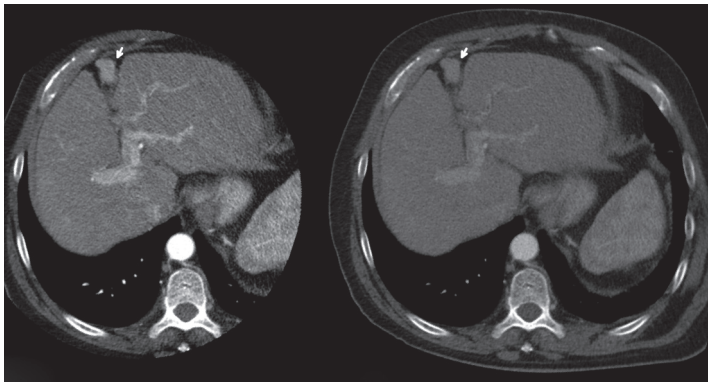

(a) (b)

FIGURE 1.10
Dual-energy late arterial phase liver axial images in a cirrhotic patient. On the left (a) the low energy (80 kVp) and on the right (b) the higher energy (140 kVp) acquisitions. Note the left liver hypertrophy and the recanalized paraumbilical vein (arrow), the latter as signs of cirrhosis and portal hypertension.

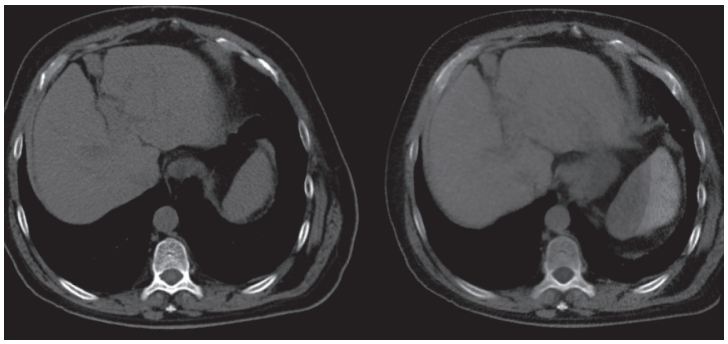

(a) (b)

FIGURE 1.11
Liver unenhanced (a) and virtual noncontrast (b) axial images. Note in the VNC image that the algorithm applies only to the area of superimposed energies. Therefore, because of the smaller field of view of the low-kVp tube, part of the volume, external to the liver area, is excluded.

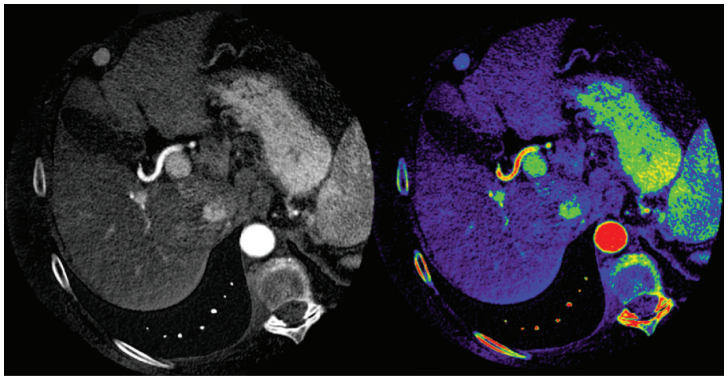

(a) (b)

FIGURE 1.12
Iodine only axial images. Color coding (b) can be applied to enhance liver vasculature or parenchymal lesions.

iodine, and fat. VNC images can therefore simulate true nonenhanced acquisitions. Investigations by Barrett et al. [36] and Zhang et al. [37] showed a 24.8% and 33% dose reduction, respectively, if the above technique is applied in a DECT of the liver. In addition, by the same algorithm, it is possible to achieve an iodine-only image dataset that eventually could be color coded, depicting the iodine distribution in the liver parenchyma, therefore, enhancing hypervascular liver lesions detection (Figure 1.12).

Advantage of a dual-energy liver acquisition is also the potential benefit arising from the acquisition of the low-kVp dataset, derived from one of the CT tubes, both in the identification and characterization of hypervascular liver tumors [38]. To understand the latter concept, the reader needs to keep in mind that kilovoltage (kVp) and milliampere second (mAs) are two important factors to be considered; mAs shares a linear relation with effective radiation dose, whereas kVp and effective radiation dose share an exponential one [39]. Iodine has specific K-edge characteristics presenting a spike at 33 keV (Figure 1.13). This intrinsic property can be taken in advantage to enhance hypervascular lesion conspicuity arising from the low-kVp acquisitions, although the latter benefit has a drawback in high image noise that needs to be compensated with higher mAs tube current values. To solve the latter drawback, different authors investigated low-kVp imaging of the liver and its ability to enhance hypervascular liver lesions in combination with iterative reconstruction (IR) methods, to lower the dose maintaining at the same time a good image quality. Presently, major CT manufacturers offer IR techniques (ASIR, MBIR, IRIS, AIDR, iDose) showing a significant lowering of patient dose delivery, up to 65%, when using a low-kVp iteratively reconstructed abdominal CT protocol [40–44]. We expect that this techniques combination (low-kVp protocols + IR) and the application of IR techniques to low-kVp acquisitions derived from DECT will be standard in the next future, for abdominal CT acquisitions.

Also DECT ability to evaluate iron deposition in a noninvasive manner is one of the interesting applications that are being investigated and showed positive results in recent literature both in phantom models [45] and in human liver transplant recipients [46].

The application of different energy spectra to the liver is a challenging and stimulating topic that is presently being investigated and in combination to future, technological advancements will yield different information that will help our diagnostic daily challenges and open new diagnostic frontiers in liver CT.

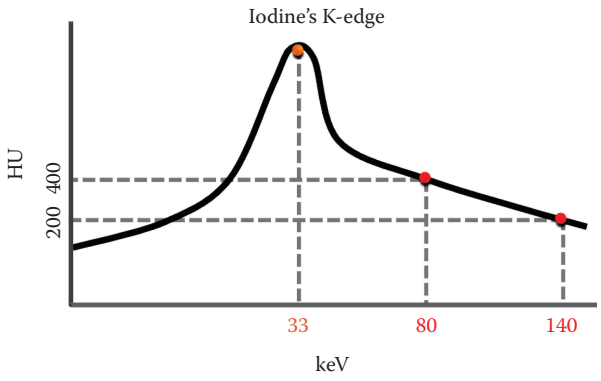

FIGURE 1.13
Graph representing the relation between iodine and different energy spectra. Note the iodine's K-edge at 33 keV.

1.9 Cystic Focal Lesions

1.9.1 Hepatic Cyst

Simple hepatic cyst is benign developmental lesion that do not communicate with the biliary tree. The current theory regarding the origin of true hepatic cyst is that they originate from hamartomatous tissue [47]. Hepatic cysts are common lesions and presume to be present in almost 5% of the population; they are more often discovered in women, almost always asymptomatic. Simple hepatic cysts can be solitary or multiple, with the latter being the more typical scenario. At histopathologic analysis, true hepatic cysts contain serous fluid and are lined by a nearly imperceptible wall consisting of cuboidal ephitelium, identical to that of bile ducts, and a thin rim of fibrous tissue. At unenhanced MDCT, hepatic cysts appear as a homogeneous hypoattenuated lesion (HU < 20), typical round or oval in shape and with well-defined wall, without contrast enhancement after contrast medium injection (Figure 1.14) [48].

1.9.2 Polycystic Disease

Autosomal dominant polycystic liver disease (ADPLD) is often found in association with renal polycystic disease. It is thought to result from progressive dilation of the abnormal ducts in biliary hamartomas as part of a ductal plate malformation at the level of the small intrahepatic bile ducts. The small bile ducts have lost continuity with the remaining biliary tree, which explains the noncommunicating nature of the cysts.

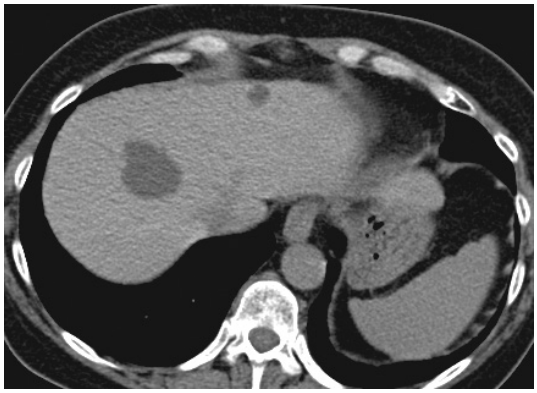

FIGURE 1.14
Simple cyst. Postcontrast CT image shows two homogeneous, rounded, well-defined, nonenhancing cystic lesions, which are consistent with simple bile duct cysts.

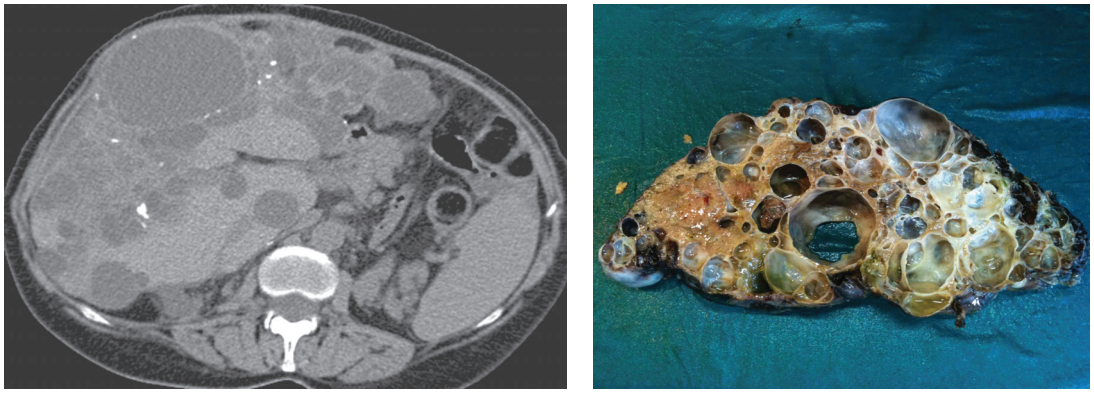

(a) (b)

FIGURE 1.15
Autosomal dominant polycystic liver disease. Precontrast CT image (a) shows multiple hepatic cysts with thin wall and regular margin; some wall calcifications may also be appreciable. Photograph of the hepatic specimen (b) shows numerous cysts that replace the hepatic parenchyma.

At imaging, it typically manifests as an enlarged and diffusely cystic liver, with the cysts varying from less than 1 cm to more than 10 cm in diameter. Calcification of the cystic walls has been reported (Figure 1.15) [49].

The leading complications in ADPLD are infection, compression, bleeding, or rupture of the cysts. Malignant degeneration is extremely rare. In selected cases of diffuse bilobar polycystic disease with massive hepatomegaly, percutaneous interventional alcohol ablation is as useful as an alternative to partial liver resection for liver transplantation [47].

Although the diagnosis of polycystic is easily made with CT, MRI is more sensitive for the detection of complicated cysts.

1.9.3 Cystic Metastases

Most hepatic metastases are solid but some have partially or complete cystic appearance. In general, two different pathologic mechanisms can explain the cyst-like appearance of hepatic metastases [50]. Hypervascular metastatic with rapid growth tumors may lead to necrosis and cystic degeneration (neuroendocrine tumor, melanoma, certain subtype of lung and breast carcinoma). Cystic metastases may also be seen in mucinous adenocarcinomas such as colorectal or ovarian carcinoma (Figure 1.16) [51]. Ovarian metastases commonly spread by means of peritoneal seeding rather than blood vessels; therefore, they appear as cystic serosal implants on the liver surface rather than intraparenchymal lesions.

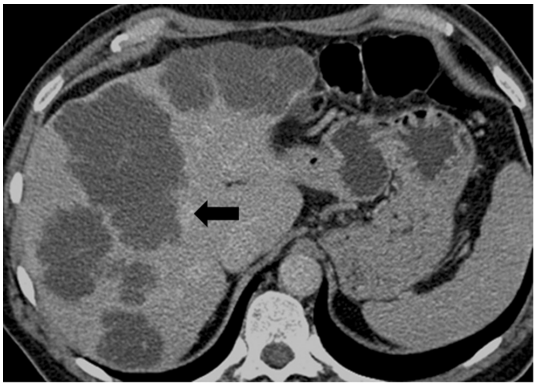

FIGURE 1.16
Cystic metastases. Postcontrast CT image acquired on portal-venous phase shows multiple cystic lesions from mucinous colorectal adenocarcinoma. In the central lesion, it is also visible a peripheral enhancing nodule (arrow).

1.9.4 Hepatic Abscesses

1.9.4.1 Pyogenic Abscess

Pyogenic abscesses may be caused by ascending cholangitis, gastrointestinal infection via the portal vein, disseminated sepsis via the hepatic artery, superinfection of necrotic tissue [52–53]. The clinical manifestations of pyogenic abscesses are highly variable. Patients may present with high fever, right-side abdominal pain, and rigors. Hepatic biochemical abnormalities are nonspecific, including slightly elevated total bilirubin and aminotransferase levels [52,54]. Early diagnosis and percutaneous treatment have markedly reduced the mortality rates [55].

Pyogenic abscesses appear as a solitary or multiple lesions ranging from few millimeters to several centimeters in diameter; when multiple may appear to cluster, or aggregate, in a pattern that suggested the beginning coalescence into a single larger abscess cavity [56].

At CT microabscesses appear as multiple hypoattenuated well-defined lesions. Faint rim enhancement and perilesional edema may be seen, findings that help differentiate them from hepatic cysts.

Large abscesses are generally well defined and hypoattenuating; they can be unilocular with smooth margins or complex with internal septa and irregular contour (Figure 1.17). Rim enhancement and presence of gas are relatively uncommon.

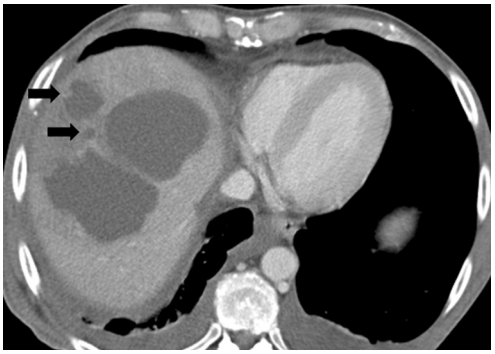

FIGURE 1.17
Hepatic pyogenic abscess. Postcontrast enhanced CT image shows a large multiloculated lesion in the right lobe of the liver surrounded by other smaller areas (arrows).

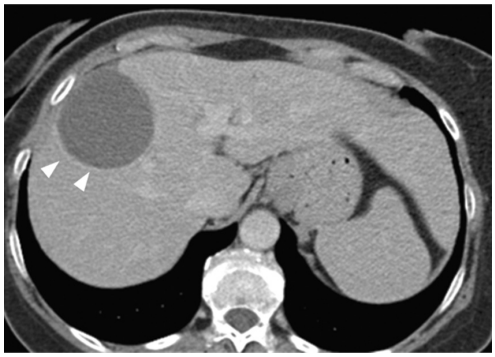

FIGURE 1.18
Amebic abscess. Contrast-enhanced CT scan shows a large, rounded, well-defined cystic mass in the right hepatic lobe. Note the slightly enhancement of the thin wall of the lesion (arrowheads).

Despite it has some characteristic finding, CT appearance of hepatic abscess is not specific and sometimes difficult to distinguish from hepatic metastases.

1.9.4.2 Amebic Abscess

Amebic liver abscess is the most common extraintestinal complication of amebiasis, occurring in 3%–9% of the cases. Patients usually show high fever and right-side abdominal pain. Histologic features of amebic liver abscesses include scant inflammatory reaction at the margins and a shaggy fibrin lining. Because of hemorrhage into the cavities, the abscesses are sometimes filled with a chocolate-colored, pasty material known as "anchovy paste." Secondary bacterial infection may make these abscesses purulent [57]. CT findings of amebic abscess are aspecific. It usually appears as a solitary oval or round mass located near the liver capsule [58]. At contrast-enhanced CT, amebic abscesses usually appear as rounded, well-defined lesions with attenuation values that indicate the presence of complex fluid (10–20 HU) [54]. An enhancing wall is common and somewhat characteristic for this lesion (Figure 1.18). The central abscess cavity may show multiple septa or fluid–debris levels and, rarely, air bubbles or hemorrhage [59–60]. Extra hepatic extension of amebic abscess is relatively common, and involvement of the chest wall, pleural cavity, pericardium, and adjacent viscera has been reported.

1.9.5 Echinococcus Disease

Hepatic echinococcosis is a severe and common parasitic disease that is endemic to the Mediterranean basin and in other countries such as Australia, New Zealand, Canada. It is generally caused by *Echinococcus granulosus*. The ingested embryos invade the intestinal mucosal wall and proceed to the liver through the portal vein system. Although the liver filters most of these embryos, those that are not destroyed become hydatid cysts [61].

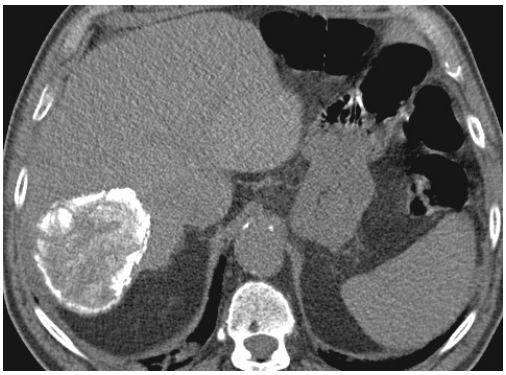

FIGURE 1.19
Hidatyd cyst. Unenhanced CT image shows a well-defined, rounded lesion, in the right lobe of the liver with wall calcifications.

Maturation of a cyst is characterized by the development of daughter cysts in the periphery as a result of endocyst invagination. At CT, hydatid cysts appear as a hypoattenuating uni- or multilocular cyst, with well-defined margins and thin or thick walls [62–64]. Generally, calcifications of the walls and/or septa may be seen [64] (Figure 1.19).

Treatment of hydatid cyst is often surgical because of the inadequate efficacy of medicine therapy.

1.9.6 Bile Duct Hamartoma

Biliary Hamartoma, also known as Von Meyenburg complex, are composed of one or more dilated bile duct-like structures lined by epithelium accompanied by a variable amount of fibrous stroma [49]. At pathologic analysis they appear as grayish-white nodular lesions that do not communicate with the biliary tree and are scattered throughout the liver parenchyma. They are typically multiple, round or oval, and small in size (less than 1.5 cm). It is difficult to distinguish them from simple cysts or microabscess (Figure 1.20) [65]. They also may be confused with liver metastases, however, the latest are more heterogeneous in size and attenuation.

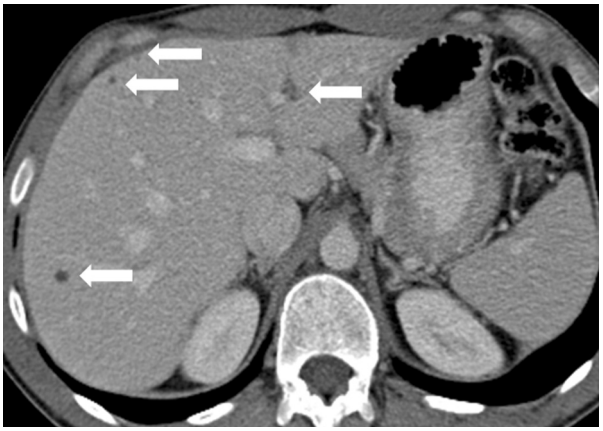

FIGURE 1.20
Biliary hamartoma. Postcontrast CT image during the portal-venous phase shows cystic-like lesion in the liver parenchyma without peripheral contrast enhancement (arrows).

At MDCT, biliary hamartomas are discovered as hypoattenuated small focal lesions, without contrast enhancement, although a peripheral enhancing rim has been described [66].

1.9.7 Biliary Cystadenoma and Cystadenocarcinoma

Biliary cystadenomas are rare, usually low growing, multilocular cystic tumors, that represent less than 5% of intrahepatic cystic lesions. They usually develop in middle-aged women and are considered premalignant lesions. They are single or multiple and the fluid within the lesion may be mucinous, serous, or hemorrhagic [67].

Polypoid, peduncolated masses are seen most commonly in cystadenocarcinoma than in cystadenoma. The MDCT features of cystadenoma and cyst-adenocarcinoma are: well-defined cystic lesions, with fibrous capsule, internal septa and rarely calcification (Figure 1.21). Wherever present, solid mass within the lesion shows enhancement after contrast medium injection [48–68].

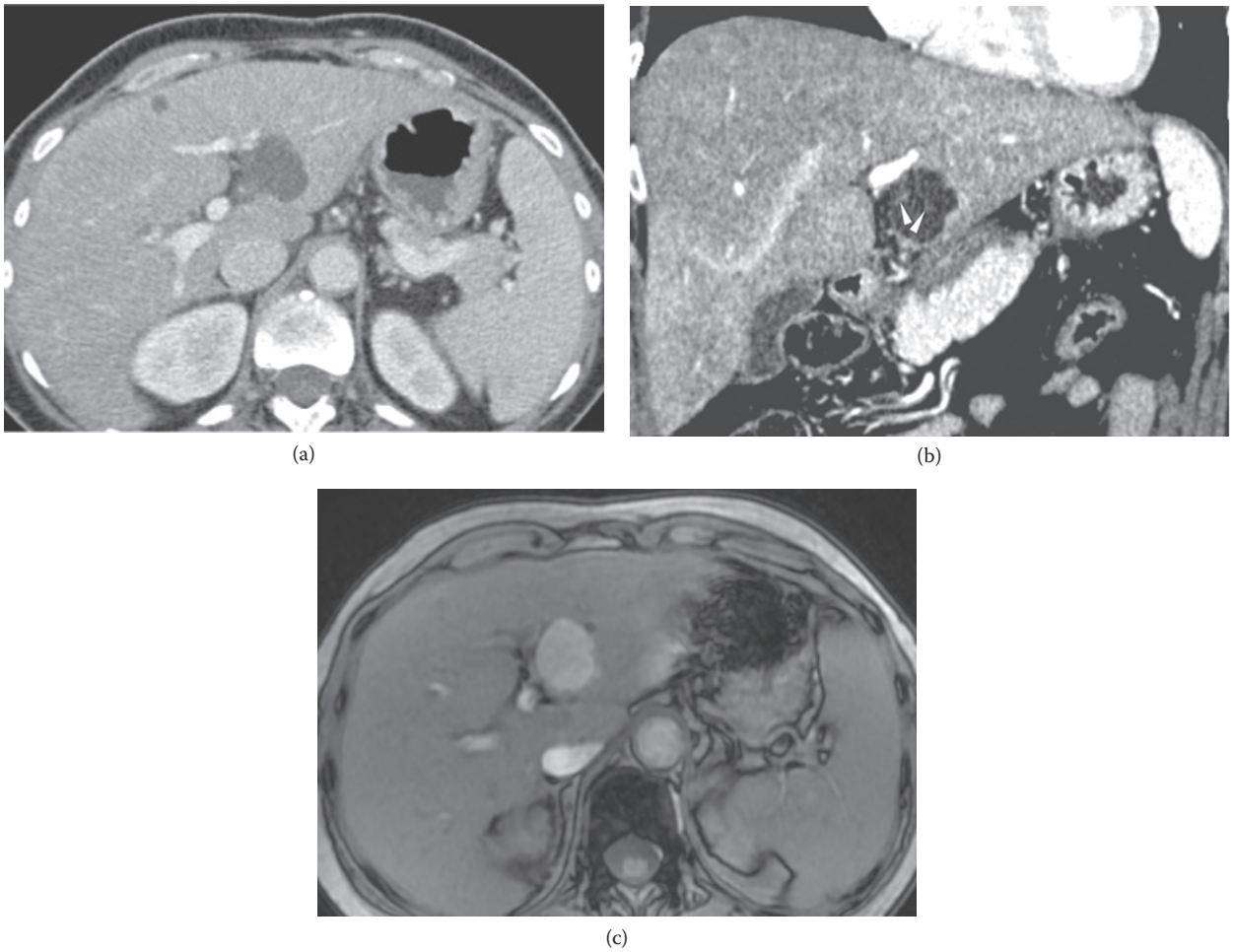

(a) (b) (c)

FIGURE 1.21
Biliary cystadenoma. Postcontrast CT images acquired on axial and coronal planes (a and b) show low-attenuation rounded lesion with regular margins and thin septa within the lesion (arrowheads). (c) Axial T1-weighted MR image shows proteinaceous content within the lesion.

1.10 Benign Focal Lesions

1.10.1 Focal Nodular Hyperplasia

Focal nodular hyperplasia (FNH) is a benign tumor caused by a hyperplastic response to a localized vascular abnormality and it is the second most common benign tumor after hemangioma [69]. FNH is common in young and middle-aged women; it's not associated to the assumption of oral contraceptives, but they have a trophic effect on growth.

The lesion is usually solitary, peripherally located, small in size (generally less than 5 cm) and sometimes with a cenral scar related to the presence of fibrous septa. Multiple FNHs are associated with multiorgan vascular malformations and such brain neoplasms [70].

The lesion is composed of hepatocytes, Kupffer's cells, and bile ducts, which are located in an abnormal order.

At unenhanced MDCT, FNH is usually either hypoattenuating or isoattenuating to the surrounding liver parenchyma. On the late arterial phase, FNH shows a strong enhancement because of its arterial supply. During the portal-venous and equilibrium phases the lesion is isodense to the surrounding liver [71]. The central scar, when present, shows delayed enhancement and washout because of the presence of mixomatous stroma (Figure 1.22) [72]. Sometimes, FNH presents a pseudocapsule related to the effective mass of the liver parenchyma and the inflammatory reaction [73]. In large lesions may be seen multiple feeding arteries, with central and septal vessels, and also ectatic draining veins (Figure 1.23) [74,75]. The differential diagnosis of FNH includes other hypervascular liver lesions such as hepatocellular adenoma, HCC, and hypervascular metastases. Therefore, distinction between FNH and other hypervascular tumors is crucial to ensure proper therapy.

1.10.2 Hepatocellular Adenoma

Hepatic Adenoma (HA) is a benign tumor which is often seen in young women with use of oral contraceptive. It arises from hepatocytes arranged in sheets of proliferated cells, with few Kupffer cells and absence of bile ducts [76]. Hepatocellular adenoma cells could present lipid and glycogen storage. It is typically a capsulated solitary lesion, although multiple lesions have been reported, with a tendency to spontaneous hemorrhage [77]. Since these lesions may also undergo malignant transformation to an HCC, it is considerate surgical [78] .

Unenhanced MDCT image may provide important clues such as fat or hemorrhage content (respectively hypo- or hyperattenuated areas) (Figure 1.24).

During the late arterial phase, hepatic adenoma enhances rapidly more than surrounding liver parenchyma. During the portal-venous phase and delayed phase, adenoma appearance is variable and not specific; most of them are nearly isoattenuating compared with surrounding liver parenchyma (Figures 1.24 and 1.25). Despite HA shows similar postcontrast pattern compared with FNH, the enhancement during the late arterial phase is higher for FNH [79]. With the introduction

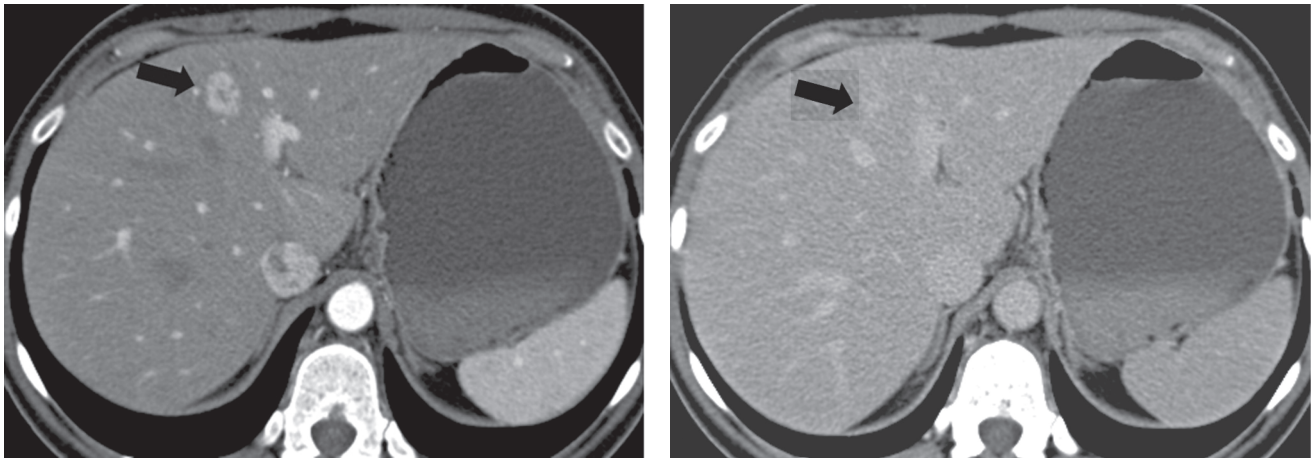

(a) (b)

FIGURE 1.22
Focal nodular hyperplasia. Postcontrast CT image acquired during the arterial phase (a) shows hypervascular lesion with a central scar (arrow). After 3 minutes during the delayed phase (b), the lesion is isoattenuating to the surrounding liver parenchyma with a slight enhancement of the central scar (arrow).

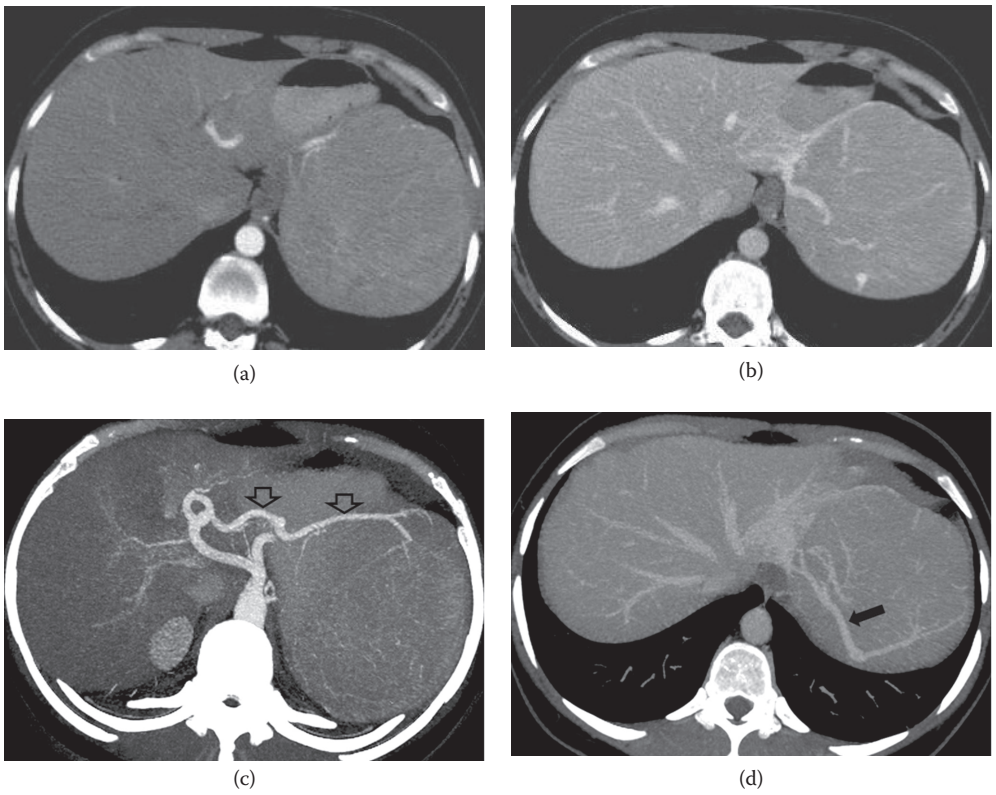

FIGURE 1.23
Focal nodular hyperplasia. Postcontrast images (a and b) acquired during the arterial and portal-venous phases show a hypervascular large mass on liver segment II (a), which becomes isoattenuating to the liver parenchyma on the delayed phase (b). Maximum intensity projection (MIP) images (c and d) show the abnormal arterial vascular supply (open arrows in c) of the lesion and a large drainage vein (arrow in d).

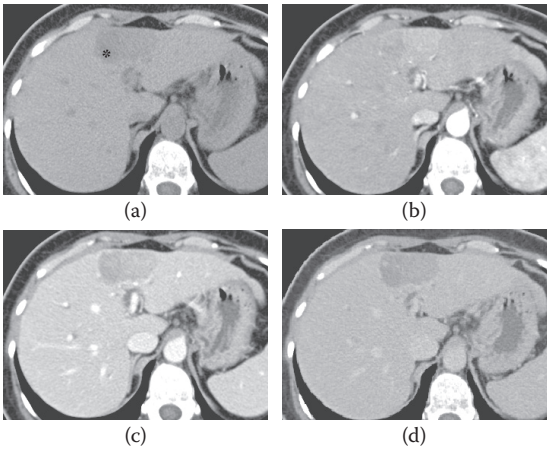

FIGURE 1.24
Hepatic adenoma. (a) Unenhanced CT image shows a rounded hypoattenuating area related to the presence of lipid storage (asterisk). On an arterial-phase CT scan (b), the tumor shows heterogeneous enhancement. (c and d) On a portal-venous and delayed CT scans the lesion becomes hypoattenuating to the surrounding liver parenchyma.

in clinical practice of liver specific contrast agent, MRI significantly increases its diagnostic performance in the differentiation of FNH from HA. Because of the presence of functional hepatocytes, FNH is hyper- to isointense on hepatobiliary phase, whereas because the absence of bile ductules, hepatic adenoma does not show uptake of the contrast agent (Figure 1.26) [80]. Because of different therapeutic management, a correct diagnosis is crucial between FNH and hepatic adenoma.

Large HAs may be heterogeneous than smaller lesions, and their CT appearance is less specific. Multiple adenomas in adenomatosis or glycogen disease may have a wide variety of imaging appearance, but CT characteristics of individual lesions are similar to those reported for solitary adenomas (Figure 1.27).

1.10.3 Hepatic Hemangioma

Hepatic hemangioma is a benign tumor composed of multiple vascular channels lined by a single layer of endothelial cells supported by a thin fibrous stroma [81].

Its vascular supply arises from a branch of the hepatic artery and presents slow flow. Most hemangiomas are asymptomatic, particularly those that are less than 4 cm. However, lesions greater than 4 cm can cause sign and symptoms sufficiently severe to require surgical treatment [82].

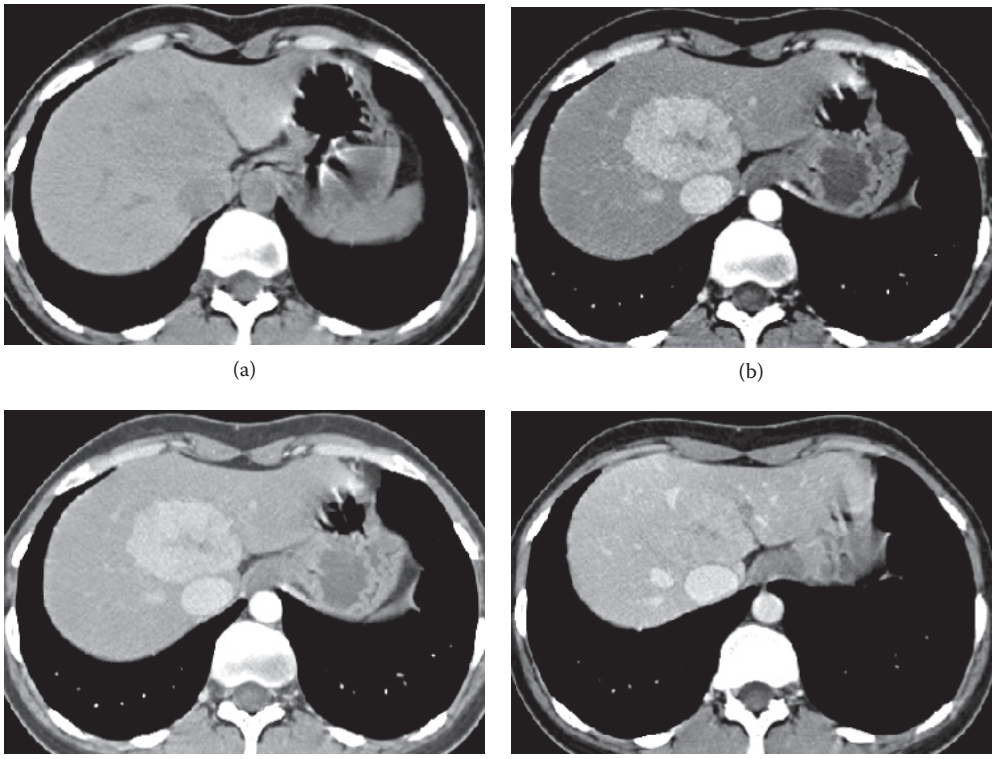

(a) (b) (c) (d)

FIGURE 1.25
Hepatic adenoma. Unenhanced CT image (a) shows a large rounded hypoattenuating mass in liver segment VIII. An Arterial-phase CT scan shows a heterogeneous hypervascular mass that becomes less evident on portal-venous and delayed phase (c and d).

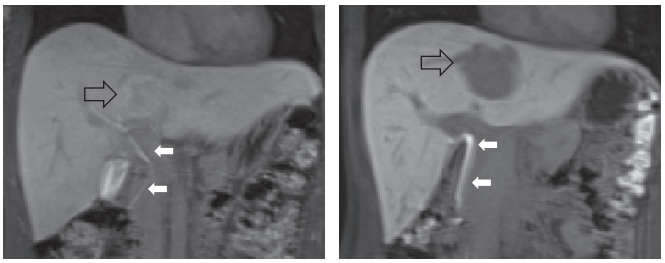

(a) (b)

FIGURE 1.26
Comparison of focal nodular hyperplasia (FNH) and hepatic adenoma (HA) during the MR imaging hepatobiliary phase. On the coronal T1-weighted MR image, FNH (open arrow in a) is iso- to hyperintense because of the presence of functional hepatocytes and bile structure nodule, whereas HA (open arrow in b) does not show uptake of contrast agent because the absence of bile ducts. Note the clear visualization of the main biliary duct on both images (arrows).

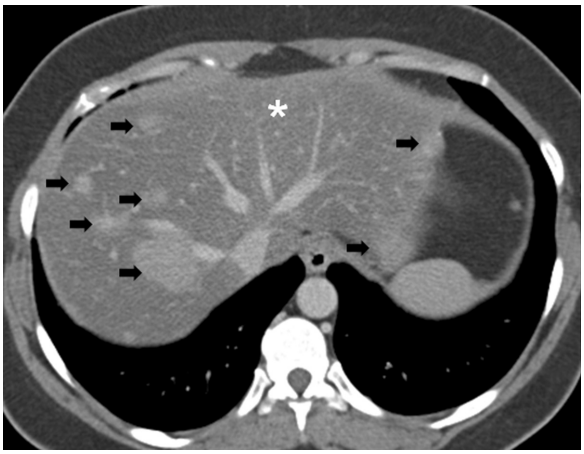

FIGURE 1.27
Hepatic adenomatosis. Postcontrast CT image on portal-venous phase shows multiple adenomas (arrowheads). The lesions appear hyperattenuating because of the underlying liver steatosis (asterisk).

At noncontrast MDCT, hemangioma shows the same clues that of vascular structures; it is hypodense to the surrounding liver parenchyma; but it should be iso- to hyperdense when liver steatosis is present [83]. Postcontrast images of hepatic hemangioma show a typical peripheral enhancement with slow progressive centripetal trend (Figures 1.28 and 1.29) [84]. Small flash-filling hemangiomas appear as high hypervascular lesion, which tends to become isoattenuating to the surrounding parenchyma on portal-venous and delayed phase, they could be misdiagnosed as arterial-portal shunt (Figure 1.30) [85].

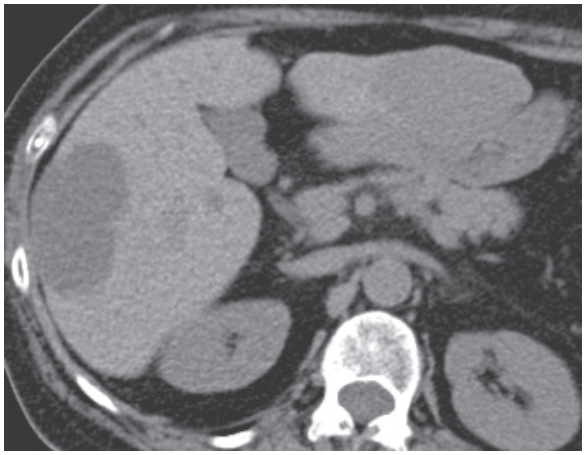

(a)

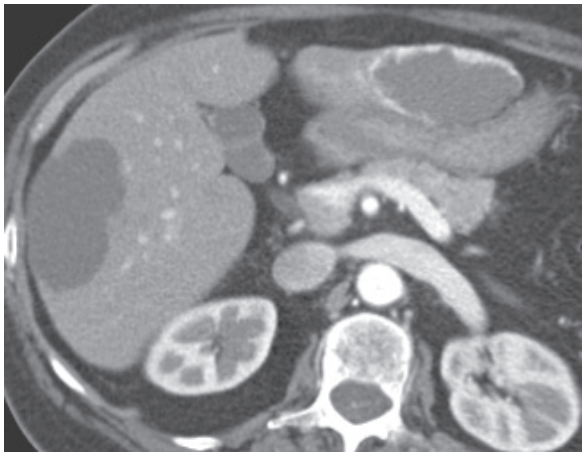

(b)

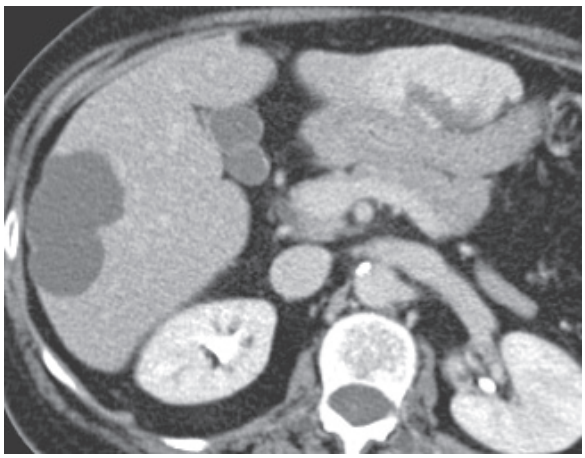

(c)

FIGURE 1.28
Hepatic hemangioma. (a) Unenhanced CT image reveals a focal liver lesion with an attenuation similar to that of vessels. (b) On arterial-phase CT scan the mass shows peripheral globular enhancement; (c) during the delayed phase the lesion is totally enhanced.

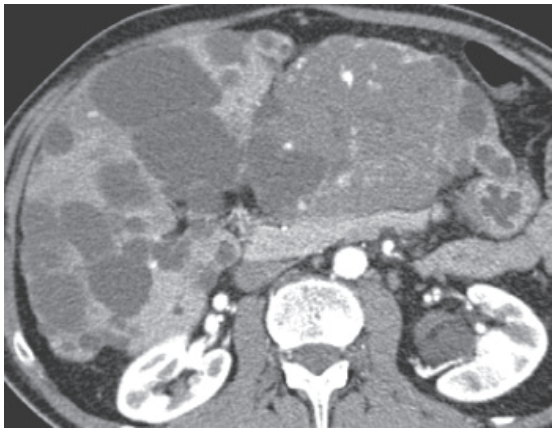

(a)

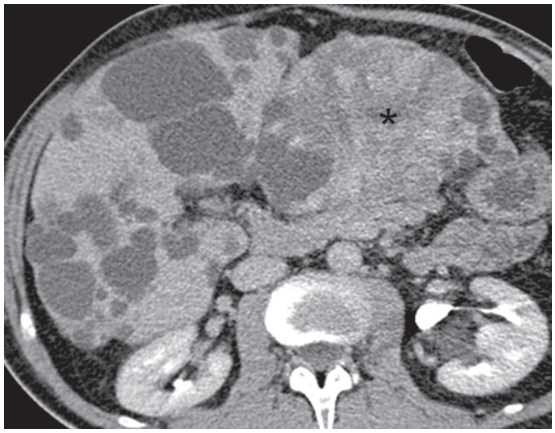

(b)

FIGURE 1.29
Hepatic hemangioma. Postcontrast CT images acquired on arterial (a) and delayed (b) phases show a large mass with typical peripheral enhancement with slow progressive centripetal enhancement. Note a central area because of the presence of fibrous tissue (asterisk).

1.11 Rare Benign Lesions

Primary leiomyoma of the liver is a rare benign tumor that affects both young and adults, with increased incidence in patients with acquired immunodeficiency syndrome or immunosuppressed state after organ transplantation [86]. It is composed of interlacing bundles of smooth muscle fibers. Clinical presentation may range from small incidentally discovered lesions to large palpable, upper abdominal masses. Although primary leiomyoma rarely degenerates into malignant lesion, liver resection is often required to yield a definite diagnosis. Results of imaging studies reported a marked enhancement of leiomyoma during the arterial phase, despite specific findings have not been shown (Figure 1.31). Further, hindering definitive diagnosis is the wide range of either

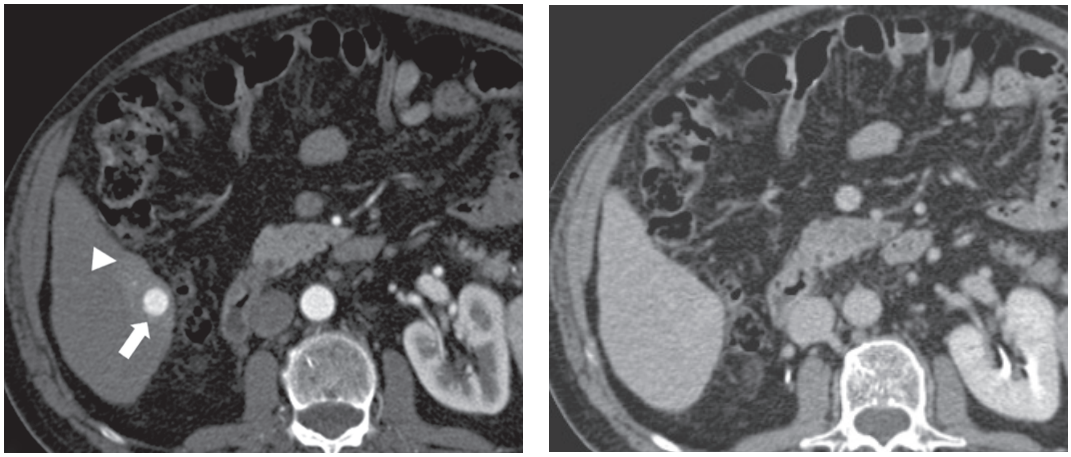

(a) (b)

FIGURE 1.30
Flash-filling hemangioma. (a) Postcontrast CT image acquired during the arterial phase show a hypervascular rounded small lesion with an attenuation similar to that of aorta (arrow). Note a tiny hypervascular area near the lesion related to an arteroportal shunt (arrowheads). (b) On the corresponding delayed phase the lesion becomes isoattenuating to the surrounded liver parenchyma.

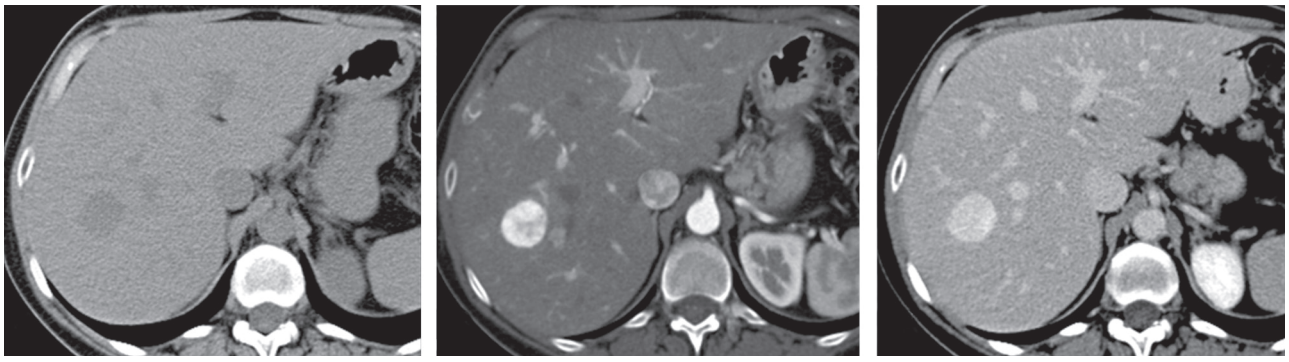

(a) (b) (c)

FIGURE 1.31
Leiomyoma. (a) Precontrast CT image shows a well-defined, rounded, hypodense lesion in the right hepatic lobe. (b and c) Postcontrast CT images acquired during the arterial and delayed phase show a hypervascular lesion with prolonged enhancement.

benign or malignant hypervascular liver lesions that could be included in any differential diagnosis [86–88].

Angiomylipoma is a benign, unencapsulated mesenchymal tumor that is composed of varying proportions of three elements: smooth muscle cells, thick-walled blood vessels, and mature adipose tissue. Angiomyolipoma can be classified on the basis of fat content into mixed, lipomatous, myomatous, and angiomatous types. At CT precontrast scan, it appears with a peripheral angiomyomatous tissue and a fatty component. Postcontrast images shows enhancement of both angiomyomatous and fatty components (Figure 1.32). It is difficult to distinguish angiomyolipoma from HCC with fatty infiltration; however, washout sign during delayed phase, typical of HCC, helps to the right characterization [89–90].

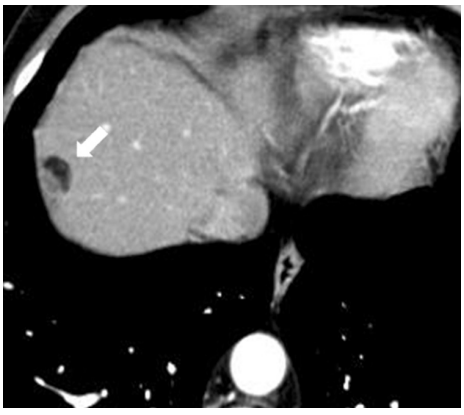

FIGURE 1.32
Angiomyolipoma. CT postcontrast image shows a well-circumscribed lesion with fat component (arrow).

1.12 Malignant Focal Lesions

1.12.1 Hepatocellular Carcinoma

HCC is the most common primary tumor of the liver and is the fourth most common tumor in men and the fifth most common in women [91,92]. It occurs primarily in subjects who have chronic liver disease or liver cirrhosis and is the primary cause of death among this group. The development of HCC may arise from de novo hepatocarcinogenesis or by means of a multistep progression from regenerative nodules, through dysplastic nodules to HCC.

Unfortunately, despite numerous technological developments and improvements in recent years, the sensitivity and specificity of MDCT in patients with cirrhosis is still relatively low, ranging between 33% and 70% [93–97]. The relatively poor diagnostic performance for the detection of HCC in cirrhotic liver is due principally to overlapping imaging features and thus, difficulties in differentiating dysplastic nodules from small HCC and to problems associated with diagnosing arterially enhancing nodules smaller than 2 cm in diameter.

The CT appearance of HCC is extremely variable and depends on growth pattern (solitary, multifocal masses or infiltrating neoplasm) (Figures 1.33 through 1.35), size, and histologic composition. Up to 36% of HCC are associated with fatty infiltration, which may aid the identification on unenhanced (Figure 1.36) [98].

The majority of HCCs are hypoattenuating on precontrast scan: although unenhanced images seem to not add significant advantage in terms of HCC detection, they could play an important role in the differentiation of uncertain lesions such as siderotic nodules, focal confluent fibrosis, and focal sparing of fatty infiltration [99].

Typically, HCC is hypervascular during the arterial phase: small lesions show more homogeneous enhancement compared with larger neoplasms that are heterogeneous because of the presence of necrosis and hemorrhage. During the portal-venous phase, HCC becomes iso- to hypoattenuating to the surrounding liver. On delayed phase, the tumors washout more rapidly than hepatic parenchyma. Based on recent guidelines, these diagnostic criteria are sufficient for a noninvasive diagnosis of HCC (Figure 1.33).

Several studies recommended the utility of delayed phase in a CT protocol of cirrhotic liver because of its ability to significantly improve the detection and characterization of HCC, especially, for smallest nodules [99–102].

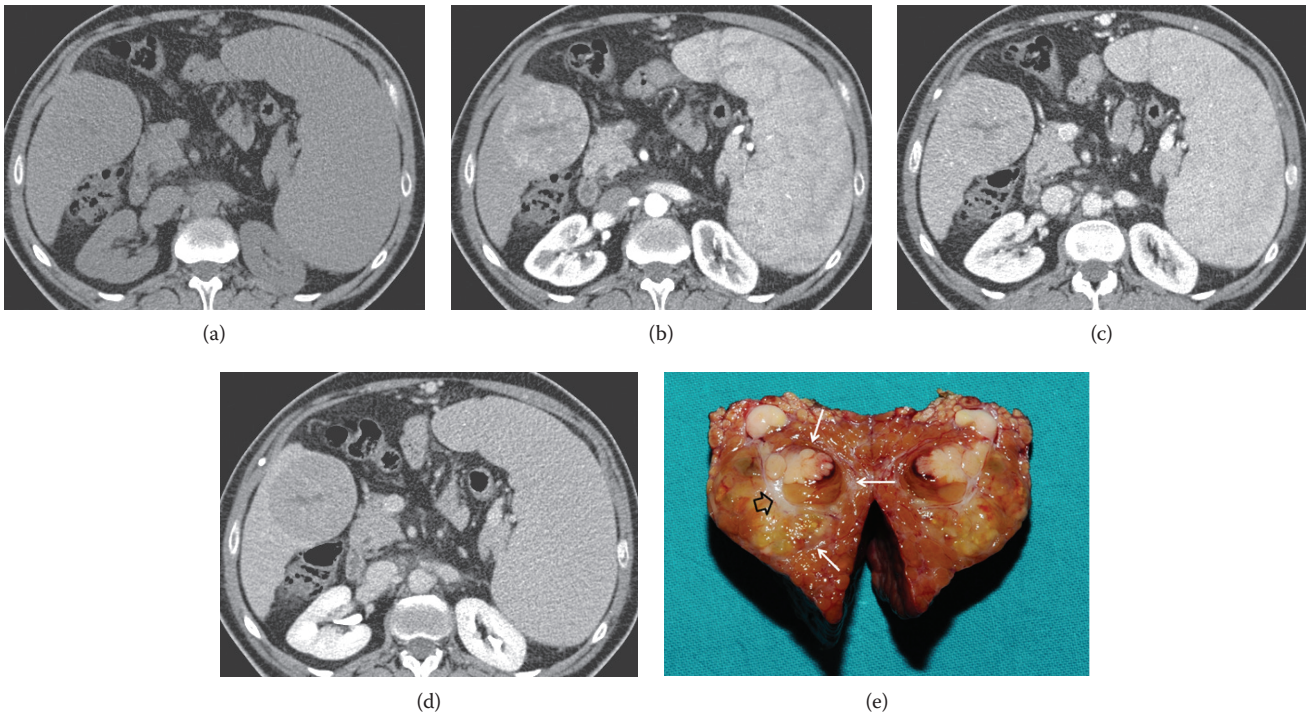

FIGURE 1.33
Hepatocellular carcinoma (HCC). Unenhanced CT image (a) shows a hypoattenuating lesion in liver segment five. (b) Postcontrast CT images reveal during the late arterial phase a hypervascular lesion which becomes isoattenuating during the portal-venous phase (c) phase and hypodense during delayed phase (d). The lesion shows the so called "wash-out" sign that is typical for HCC. (e) Photograph of the gross specimen shows an encapsulated lesion (arrows) within fibrous septum (open arrow). (Courtesy of M. Rossi, MD.)

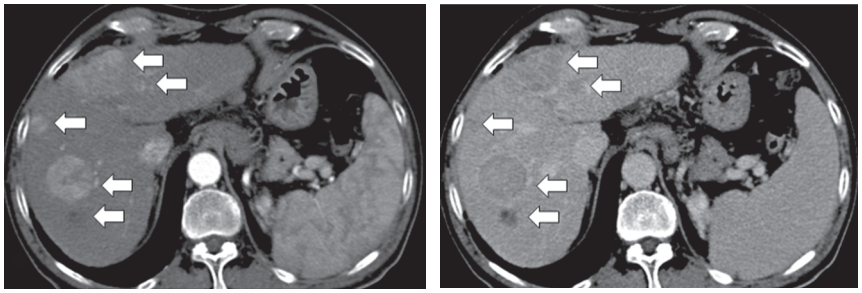

(a) (b)

FIGURE 1.34
Multifocal hepatocellular carcinoma. (a and b) Postcontrast CT images acquired during arterial and delayed phase reported multiple hypervascular masses with washout after three minutes of contrast medium injection typical for HCCs (arrows).

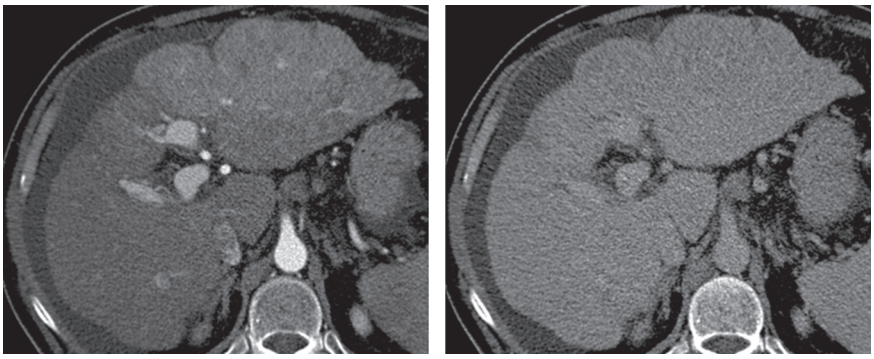

(a) (b)

FIGURE 1.35
Infiltrative hepatocellular carcinoma. (a) Postcontrast CT images acquired during arterial phase show a large hypervascular area that englobes all the left liver lobe, modifying its anterior surface, which shows irregular margins. (b) On delayed phase this area is slightly hypoattenuating to the right liver lobe.

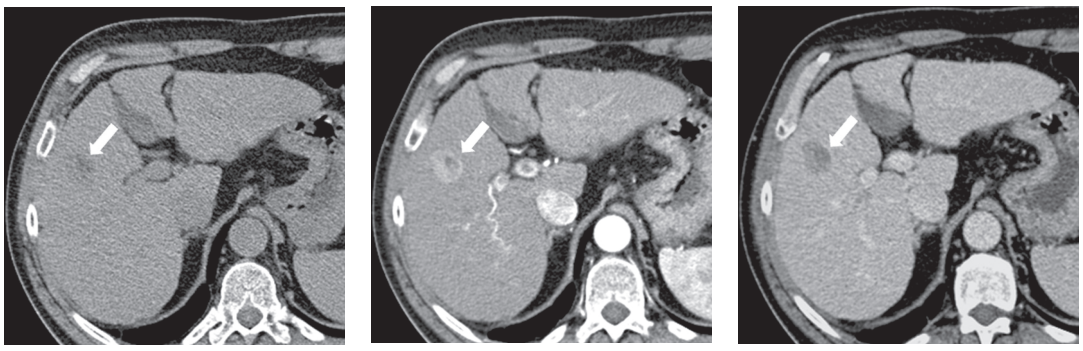

(a) (b) (c)

FIGURE 1.36
Hepatocellular carcinoma. (a–c) Pre- and postcontrast CT images reveal typical HCC in liver segment five with a small area of adipose tissue density. Generally, presence of fat tissue within the tumor is associated to well-differentiated neoplasm.

HCC could also present atypical findings such as ipervascular lesion without washout or hypovascular tumor (Figure 1.37). Hypovascular nodules are not uncommon and they usually represent early stages like displastic nodules with focal HCC or well-differentiated small HCCs. They show little or any enhancement during the arterial phase. They may also be poorly visualized on later scans as iso- to hypodense lesion. It has been recently shown that hypervascular HCCs without washout represent almost 45% of hypervascular nodules encountered in cirrhotic liver. As well as, of 12% of large (>2 cm) hypovascular nodules discovered in explanted liver, 66% are HCCs [103].

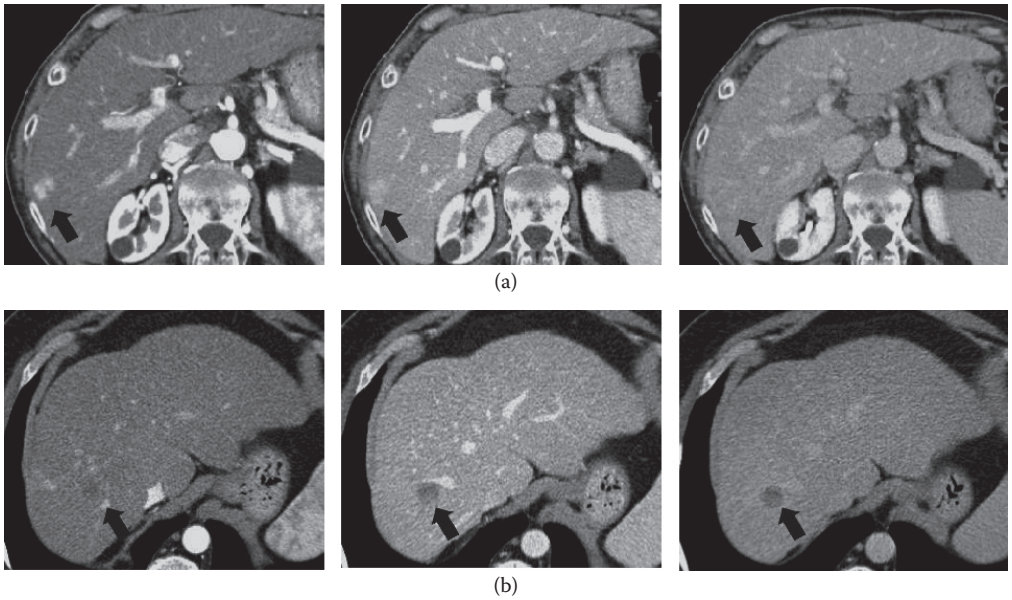

FIGURE 1.37
Hepatocellular carcinoma with atypical findings. (a) Pre- and postcontrast CT images of hypervascular HCC without washout sign. (b) Pre- and postcontrast CT images of hypovascular HCC.

Moreover, HCC could present a tumor capsule, which may be visible on delayed phase.

Thrombosis of portal-venous branches occurs in up to 40% of HCCs and is frequently caused by direct tumor invasion: these tumor thrombi are only moderately hypoattenuating and enhance irregularly after contrast administration during the arterial phase (Figure 1.38). The invasion of the hepatic veins is less common and may cause occlusion leading to a Budd–Chiari syndrome.

Despite, HCC develops mainly in patients with cirrhosis caused by virus B and C infection or alcohol abuse; it has been recently shown that nonalcoholic fatty liver disease (NAFLD) is one of the most common causes of liver chronic disease and it has a high risk to develop HCC. Recently, CT imaging findings of HCC in this particular patients' population have been described [104]. The neoplasm usually manifests as a large, hypervascular, solitary mass characterized by smooth and capsulated margins and central necrotic area (Figure 1.39).

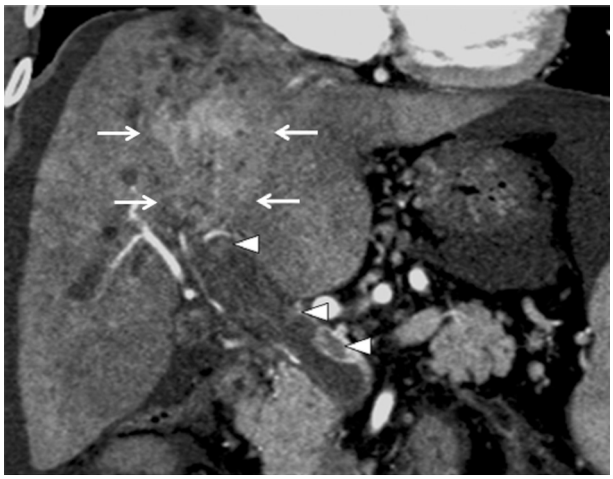

FIGURE 1.38
Diffuse hepatocellular carcinoma with neoplastic involvement of portal vein (PV). Coronal postcontrast CT image show a diffuse ill-defined hypervascular mass in liver segment VIII (arrows) with thrombus into the PV. Note the enlargement of the PV and its tiny enhancement (arrowheads).

1.12.2 Intrahepatic Cholangiocarcinoma

CCC is the most common primary tumor of the bile ducts. Patients usually present painless and jaundice due to biliary obstruction. It should be classified as peripheral or hilar. A tumor originating from the primary bile duct branches is considered at the hilum; moreover a lesion that arises at the confluence of the left and right hepatic ducts is referred as a Klatskin tumor. Predisposing factors for CCC include ulcerative colitis, Caroli disease, sclerosing cholangitis, and congenital biliary abnormalities. The role of MDCT imaging is to establish tumor extension and its resectability. The CT appearance of intrahepatic CCC is classified into three types: mass-forming, periductal infiltrating, and intraductal. Peripheral tumors usually appear as well-defined or irregular mass-forming lesion along the course of dilated intrahepatic ducts, usually with liver capsule retraction. On CT, during

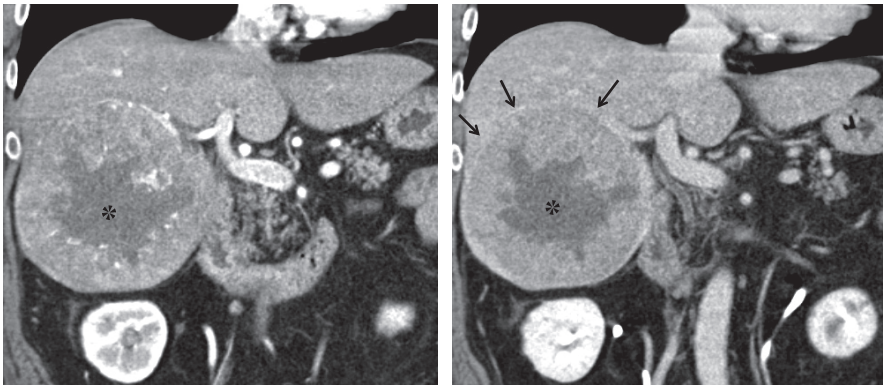

(a) (b)

FIGURE 1.39
Hepatocellular carcinoma in nonalcoholic fatty liver disease (NAFLD). (a) Postcontrast CT image during arterial phase shows a faintly hyperattenuating mass with a central hypoattenuating necrotic area (asterisk). (b) Contrast-enhanced image during delayed phase shows washout of the solid component and a peripheral capsule (arrows).

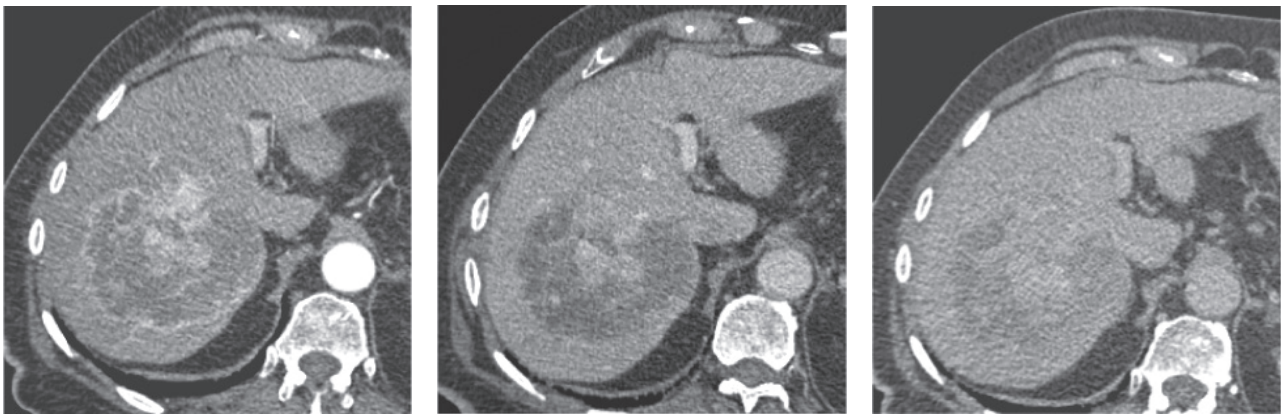

(a) (b) (c)

FIGURE 1.40
Peripheral cholangiocarcinoma. (a and b) Postcontrast CT image during arterial and portal-venous phases show a low-attenuation mass with rim enhancement. (c) On delayed phase CT scan, the mass looks smaller because of the enhancement of the central zone.

both late arterial and portal-venous phase, CCC shows as a hypoattenuating mass with incomplete peripheral rim enhancement [105–107]. The central portion of the tumor may show prolonged enhancement and be hyperattenuating on delayed phase (10 minutes) because of slow washout related to the large amount of fibrous tissue (Figure 1.40) [108]. Hilar CCC typically takes one of the three shapes: infiltrative, exophytic, or polypoid (Figure 1.41). The most common type is the periductal infiltrating form. Postcontrast CT images of infiltrating hilar CCC may detect focal duct wall thickening, which appears hyperattenuating relative to liver parenchyma during the portal-venous phase or delayed [109]. A supplementary CT finding of hilar carcinomas includes lobar atrophy because of either severe or long-standing ductal obstruction.

1.12.3 Metastases

One of the major indications for hepatic MDCT is the detection of metastatic liver disease, which is by far the most common malignant tumor in patients without cirrhosis. The CT image appearance of liver metastases may vary widely depending on the histologic nature of the lesion, size presence of necrosis or calcification. The type of MDCT protocol for depiction of liver metastases depends on the degree of primary tumor vascularization.

Most hepatic metastases are hypovascular and arise from primary tumor of gastrointestinal tract, pancreas, urothelium, lung, head, and neck, as well as gynecologic tumors. During the portal-venous phase, these lesions are typically hypoattenuating owing to superior enhancement of adjacent liver parenchyma, so most authorities recommend a single-CT scan during

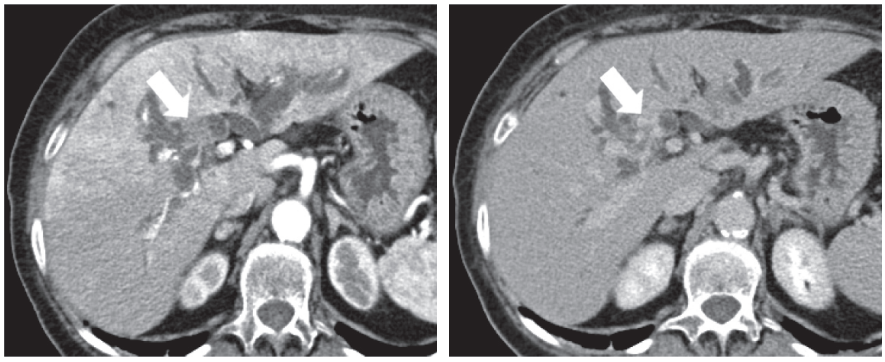

(a) (b)

FIGURE 1.41
Polypoid hilar cholangiocarcinoma. (a) Postcontrast CT image during the arterial phase shows a hypoattenuating mass at the hepatic hilum, mainly in segment IV (arrow). Both intrahepatic ducts are dilated. (b) Postcontrast CT image during delayed phase (8 minutes) show an enhancement of the lesion because of the presence of fibrous stroma.

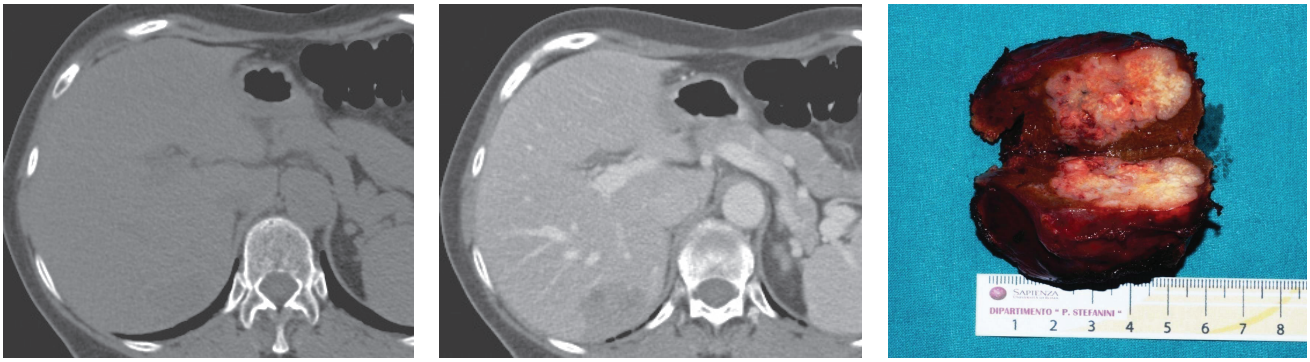

(a) (b) (c)

FIGURE 1.42
Hypovascular metastasis. (a) Precontrast image shows a hypoattenuating subcapsular lesion in liver segment VII. (b) Postcontrast CT images during the portal-venous phase shows a hypoattenuating lesion to the surrounding liver. (c) Photograph of liver specimen reveals the malignant nature of the lesion. (Courtesy of M. Rossi, MD.)

the portal-venous phase for evaluation of hypovascular metastases (Figure 1.42). In the periphery of these metastases, there may be increased enhancement during either arterial or portal-venous phase, represented by a hypervascular rim or halo, which is been recently showed in almost 85% of hypovascular metastases (Figure 1.43) [110]. Several studies have shown that the additional use of precontrast or hepatic arterial phase does not improve the detection of hypovascular liver metastases [111–113]. The reported detection rate of hypovascular liver metastases for CT is ranging between 85% and 91% [110–114]. Precontrast images are useful in the detection of hemorrhage or calcification within the lesion: calcified metastases are more commonly associated with mucinous colorectal cancer; however, a wide variety of other primary tumors are associated with calcified liver metastases (renal cell carcinoma, breast carcinoma, chondrosarcoma) [115]. These calcifications may be central or peripheral in location and are founded in areas of reduced attenuation (Figure 1.44).

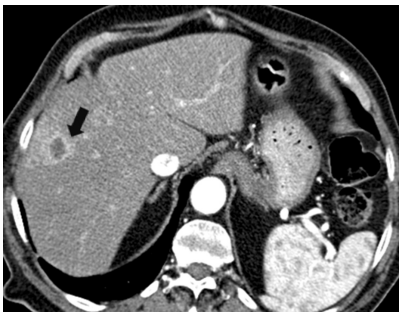

FIGURE 1.43
Hypovascular metastasis with rim enhancement. Transverse arterial phase CT scan of metastasis from a colo-rectal cancer depicts ring enhancement (arrows) with well-defined smooth inner margins surrounding central regions of low attenuation.

Few studies investigated the usefulness of smaller slice thickness in the identification of liver metastases: no more benefits have been reported for a slice thickness of 2.5 cm compared with 5 mm. It should suggest that lot of small lesions (≤15 mm) are benign [116]. However,

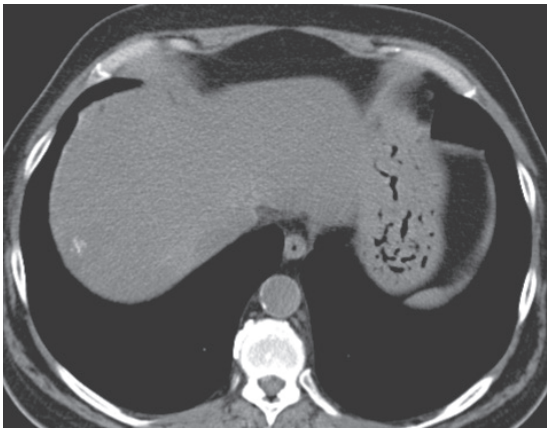

(a)

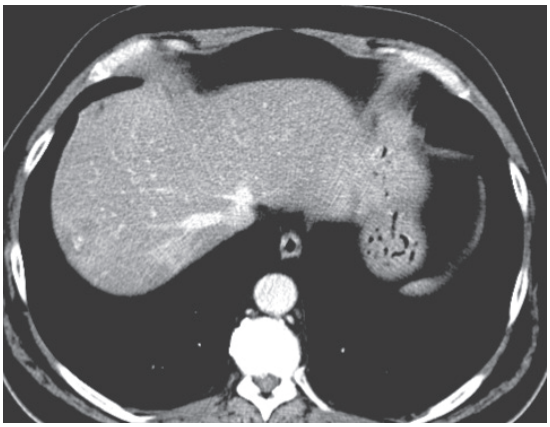

(b)

FIGURE 1.44
Calcified metastasis. (a) Precontrast CT image shows a calcified lesion within a hypoattenuating area. (b) Postcontrast CT image acquired during the portal-venous phase showed a hypodense focal liver lesion with a central calcification resulting a calcified metastasis from colorectal cancer.

further studies should be conducted to assess the optimal slice thickness for the identification of liver metastases.

Primary tumor that tend to be associated with hypervascular metastases include neuroendocrine tumors, renal cell carcinoma, thyroid carcinoma, melanoma, and occasionally breast cancer. The imaging protocol for hypervascular metastases is significantly different from hypovascular. Hypervascular lesions are typically hyperattenuating during the late arterial phase because of an earlier and increased contrast media uptake compared with adjacent liver parenchyma and becomes isoattenuating to liver parenchyma on subsequent vascular phases (Figure 1.45) [117,118]. These lesions are sometimes misinterpreted as FNH, hemangiomas, and focal fatty infiltration.

In the detection of liver metastases, CT and MRI have been shown to be effective for the detection and characterization of liver metastases, with slight, albeit nonsignificant, tendency for better overall diagnostic

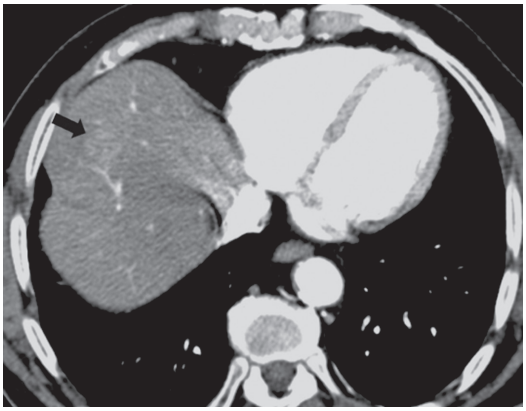

(a)

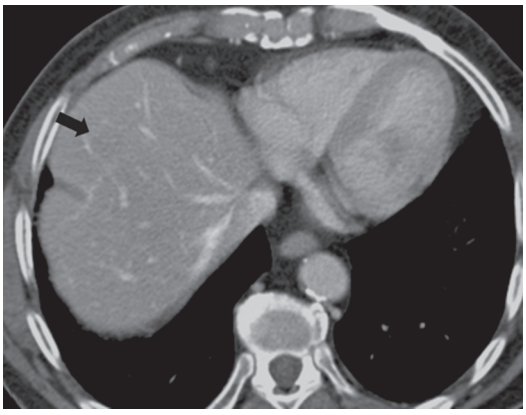

(b)

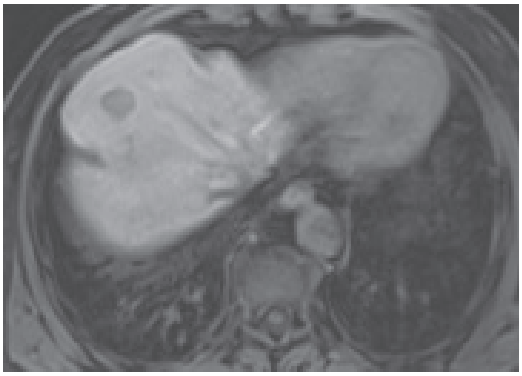

(c)

FIGURE 1.45
Hypervascular metastasis. (a) Postcontrast CT image acquired during the arterial phase show a hypervascular lesion in liver segment VIII. (b) On delayed phase, the lesion in slightly hypoattenuating compared to the surrounding liver parenchyma. (c) MR imaging acquired during the hepatobiliary phase helps to correctly characterize this lesion, indeed it shows a hypointense lesion to the surrounding parenchyma, which is a sign of absence of functional hepatocytes.

performance for the latter technique. Moreover, the introduction in clinical practice of hepatobiliary contrast agent significantly improves the diagnostic performance of MR in the detection of liver metastases (Figure 1.45) [119–121].

1.13 Rare Malignant Lesions

Epithelioid hemangioendothelioma is a primary malignant vascular tumor of the liver, characterized by the epithelioid appearance with neoplastic cells [122].

It should not be confused with infantile epithelioid hemangioendothelioma, which is benign and occurs exclusively in young children and resolves spontaneously in many cases [123]. Two-thirds of the patients are women; the clinical course is unpredictable and variable; however, most of the 40% have an extended survival at 5 years. It is usually constituted by multiple peripheral nodules, composed by a central hypocellular area and a peripheral hypercellular rim zone. Nodules may merge into a large mass; they often determine liver capsule retraction and rare calcifications may be present [124].

Unenhanced MDCT images show an area of homogeneous low attenuation compared to the surrounding liver. Postcontrast images show a central area of low density with peripheral rim enhancement. Some lesions have a second more peripheral hypodense zone that correlated with a thin avascular rim visible at histopathologic examination (Figure 1.46) [125].

Primary angiosarcoma of the liver is a malignant spindle cell tumor of endothelial cell derivation that can form poorly organized vessels, grow along performed vascular channels, and be arranged in sinusoidal or cavernous spaces or form solid nodules or masses [126]. It has an example of malignant transformation secondary to environmental exposure and has been associated with multiple chemical carcinogens including thorium dioxide, vinyl chloride, and arsenic [127]. The prognosis at the time of the diagnosis is infausted, with a median survival of only 6 months.

It could be present as a single large mass, multiple, or both; peripheral located nodules or mass may produce hemoperitoneum.

Nonenhanced CT shows a hypoattenuated lesion with iso- to hyperdense area because of the presence of hemorrhagic areas. After contrast agent administration, angiosarcoma reported a heterogeneous patchy enhancement; however, it has been also described in literature a vascular pattern similar to that of hepatic hemangioma [128]. Combined interpretation of pre- and postcontrast images helps to well characterize angiosarcoma from hemangioma; moreover, hemangioma show a centripetal wash-in, whereas nodular enhancement of angiosarcoma are generally central and irregular. Multiple nodular patterns should be mistaken as hypervascular metastases [129].

Primary lymphoma of the liver is a rare tumor, but its incidence is increasing. It is generally a non-Hodgkin type. It develops as a single, large, multilobulated mass (Figure 1.47).

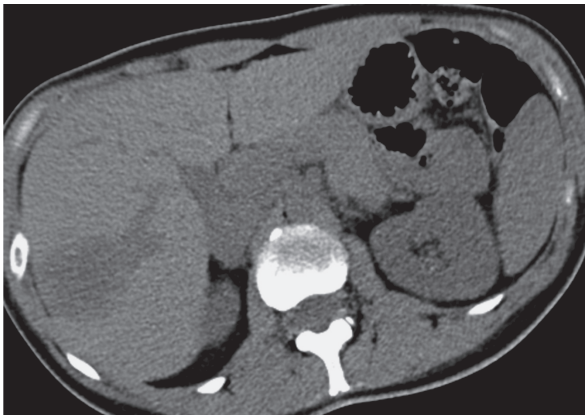

(a)

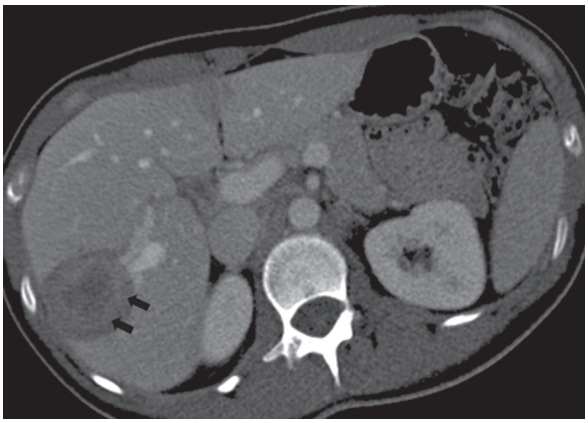

(b)

FIGURE 1.46
Hepitheliod hemangioendothelioma. (a) Unenhanced CT image shows a homogeneous hypoattenuating peripheral located lesion with tiny capsular retraction. Postcontrast CT image (b) shows tumor nodule with complex enhancement pattern consisting of a nonenhancing center, hypervascular rim, and low-attenuation outer halo (arrows).

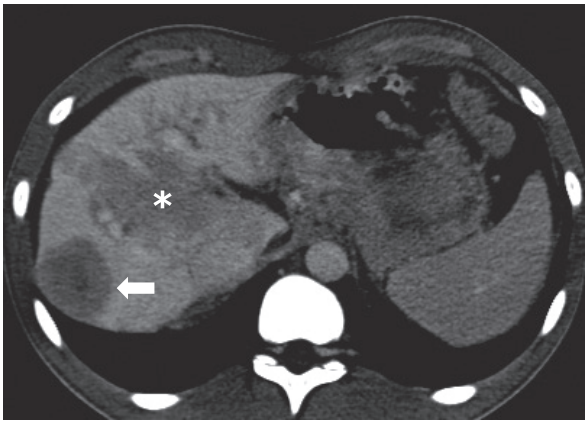

FIGURE 1.47
Hepatic lymphoma. Postcontrast CT image shows a large hypodense mass in the liver segment VII. Note a diffuse and heterogeneous area in the central segments because of the presence of acute hepatitis (asterisk).

Un-enhanced CT images show a hypoattenuting lesion; postcontrast scans reveal a hypodense mass. Sometimes thin rim enhancement or calcifications may be present.

Secondary liver lymphoma can have a greater variety of appearances and is more likely to be multiple or diffusely infiltrating lesions than a solitary lesion [131].

1.14 Vascular and Perfusion Disorders

1.14.1 Budd–Chiari Syndrome

Budd–Chiari syndrome is an uncommon disorder resulting from an obstructed hepatic venous outflow tract. The obstruction lesion is situated in the main hepatic veins, in the IVC or in both. It is classified as primary when it is caused by an intrinsic luminal web or thrombus, and secondary when it is caused by an extraluminal compression or neoplasm invasion [132]. Membrane or web arises from the wall of the vessels and may obliterate the lumen completely or partially. This type of lesion is believed to be a sequel of long-standing thrombosis. Hematologic abnormalities (factor V Leiden mutation, myeloproliferative disorders, antiphospholipid syndrome, etc.) are responsible for the majority of cases of Budd–Chiari syndrome [133]. The other factors include pregnancy immediate postpartum and use of oral contraceptives.

The secondary Budd–Chiari syndrome is caused by an extraluminal compression of a space occupying lesion or luminal invasion of malignant neoplasia (renal cell carcinoma, adrenal carcinoma, and HCC, primary leiomyosarcoma of IVC. As the hepatic vein constitutes the sole efferent vascular drainage of the liver, obstruction or increased pressure within these vessels result in an increased sinusoidal pressure, which leads in a delayed or reversed portal-venous outflow.

The portal-venous stasis and congestion cause hypoxemic damage in adjacent hepatocytes. Afterward, centrilobular fibrosis, nodular regenerative hyperplasia, and ultimately cirrhosis occur.

At unenhanced MDCT, acute form of Budd–Chiari syndrome show diffuse hypodensity of enlarged liver. Hepatic veins are narrowed and hyperdense thrombus may be seen [134]. Postcontrast MDCT images show an early enhancement of caudate lobe and central parenchyma around IVC with decreased liver enhancement peripherally (Figures 1.48 and 1.49). On delayed phase it could be observed a late enhancement of the previously hypodense areas leading to an almost homogenous areas or a hyperdensity of the peripheral parenchyma (flip-flop sign) (Figure 1.49b). In chronic stage, caudate lobe is often enlarged and main hepatic veins cannot be seen. The presence of regenerative nodules leads to a progression to cirrhosis and so the risk to develop HCC. Of about 40% of cases, the enhancement pattern of the liver is almost homogeneous; this is because of the more stable hepatic perfusion that occurs after the formation of intra- and extrahepatic collateral veins [135–136].

1.14.2 Passive Hepatic Congestion

Passive hepatic congestion is caused by stasis of blood within liver parenchyma because of a compromised venous drainage. It is a common complication of congestive heart failure and constrictive pericarditis, wherein elevated central venous pressure is directly transmitted from the right atrium to the hepatic veins [137].

On contrast-enhanced MDCT, liver parenchyma may present an inhomogeneous mottled, reticulated-mosaic pattern. Retrograde hepatic venous opacification on the initial bolus scans is also a transient finding indicative of elevated right heart pressure (Figure 1.50). Moreover, IVC and hepatic veins are enlarged (Figure 1.51) [138].

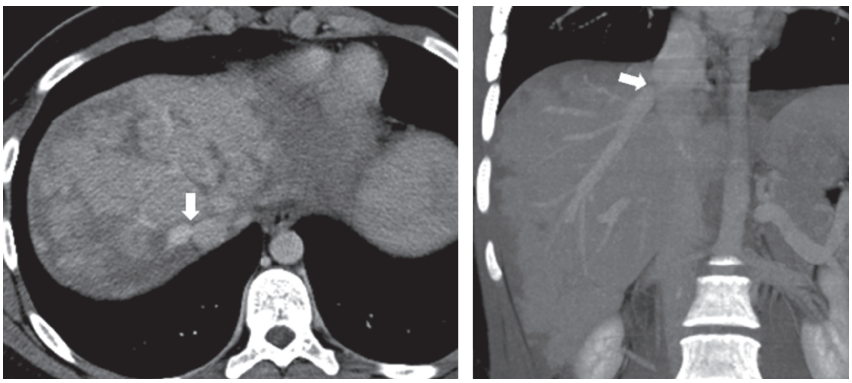

(a) (b)

FIGURE 1.48
Budd–Chiari syndrome. (a and b) Axial and coronal postcontrast CT images during the portal-venous phases show an inhomogeneous enhancement of liver parenchyma because of the obstruction of left and median hepatic veins. Note a diaphragm at the origin of the right hepatic vein (arrow).

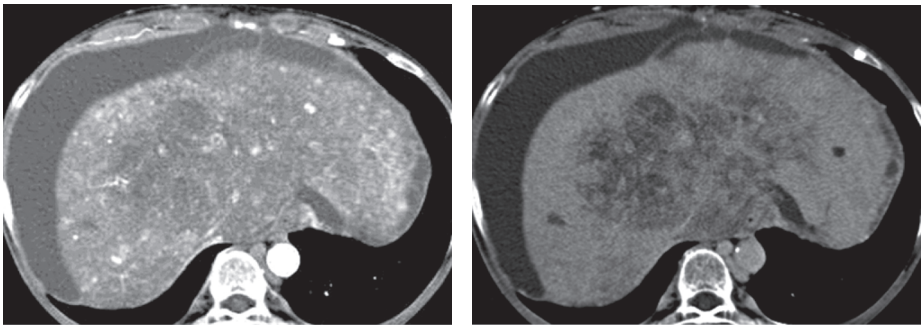

(a) (b)

FIGURE 1.49
Budd–Chiari syndrome. Axial postcontrast CT image acquired during the arterial phase (a) shows multiple hypervascular nodules in an enlarged liver. Postcontrast axial image acquired during the delayed phase (b) shows a low attenuation of the central part of the liver with accumulation of the contrast material from the capsular veins (flip-flop sign).

Other collateral nonspecific findings that could be present are cardiomegaly, ascites, and pleural effusions.

The parenchyma enhancement pattern is similar to that of Budd–Chiari syndrome but in this latest case the IVC and hepatic veins are not opacificated, and large regenerative nodules may be present [139].

1.14.3 Hereditary Hemorrhagic Telangiectasia (Osler–Weber–Rendu Syndrome)

Hereditary hemorragic telenagectasia (HHT) is a rare autosomal dominant, multisystem vascular disorder affecting many organ systems and occurring in approximately 10–20 individuals per 100,000 [140,141]. It is characterized by angiodysplastic lesions, in which there is direct communication between arteries and veins of varying sizes without an intervening capillary network [142].

Hepatic vascular lesions range from tiny telangiectases to transient perfusion abnormalities and large confluent vascular masses [143,144].

Focal hepatic lesions are often associated with arteriovenous, arterioportal, or portovenous shunts. Telangiectases are the most commonly seen hepatic lesion and can be focal or diffuse. They are hypervascular rounded masses, usually measuring only few millimeters in size. Coronal MIP images are helpful in appreciating telangiectases, especially when they exist in proximity to the large vessels.

Large confluent vascular masses are defined as large areas of multiple telangiectases that coalesce or large shunts that are directly visible; any enhancing lesion with a diameter larger than 10 mm is so called [143]. These lesions usually show early enhancement that is seen during arterial and portal-venous phases (Figure 1.52).

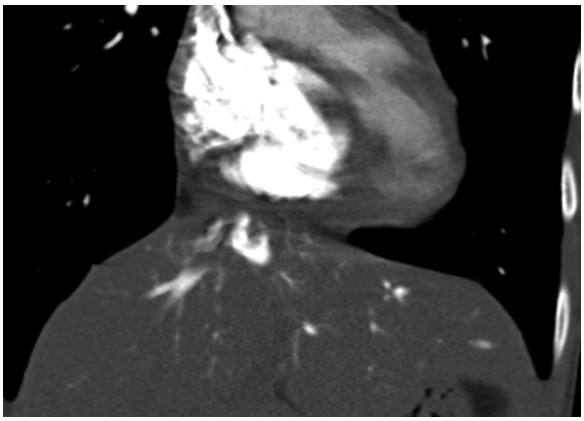

FIGURE 1.50
Hepatic congestion. Postcontrast coronal reformatted image acquired for the study of the pulmonary vessels shows retrograde enhancement of the inferior vena cava and the hepatic veins, which is a sign of elevated right heart pressure.

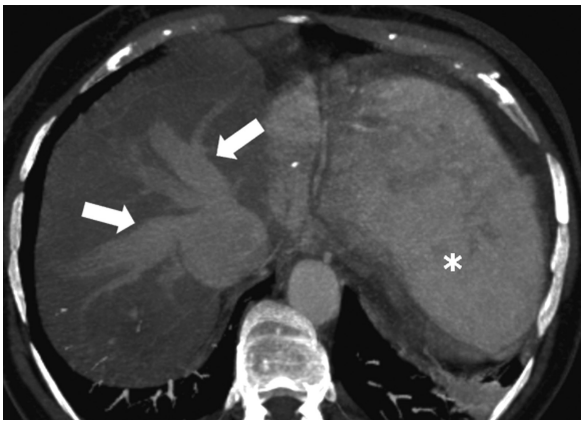

FIGURE 1.51
Hepatic congestion. Axial maximum intensity projection (MIP) image show the great dilatation of the inferior vena cava and the hepatic veins (arrows). Note the great volume of the heart (asterisk).

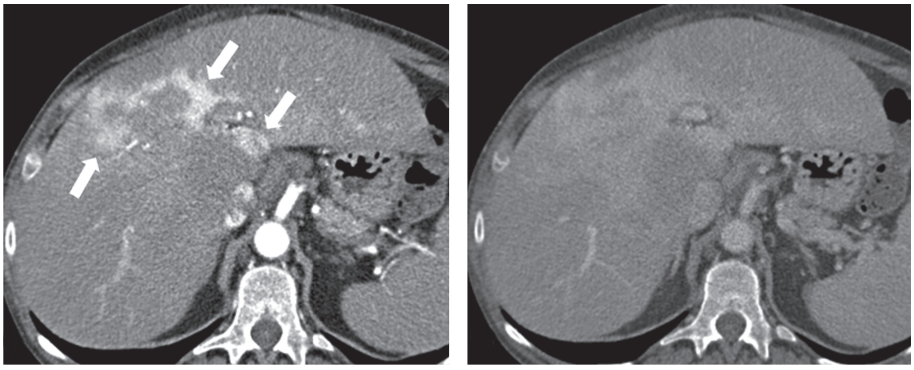

(a) (b)

FIGURE 1.52
Hereditary hemorragic telangiectasia: (a and b) Postcontrast CT images during arterial and portal-venous phase show large confluent vascular masses (arrows). The masses show delayed and persistent enhancement.

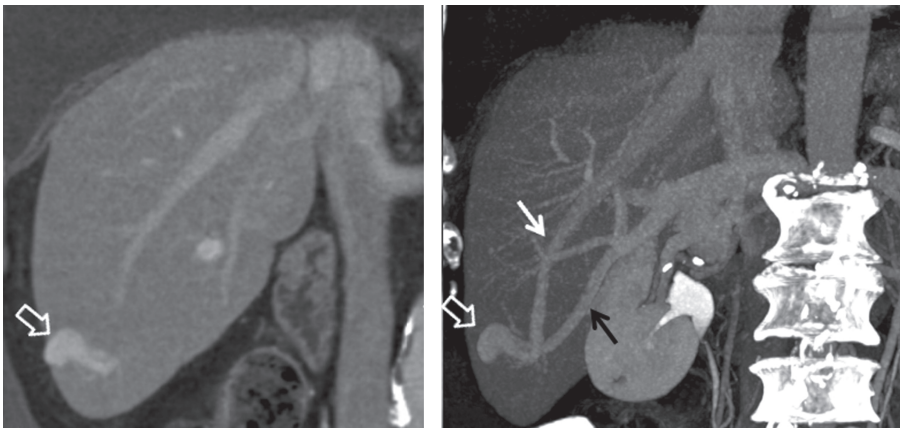

(a) (b)

FIGURE 1.53
Hereditary hemorragic telangiectasia. Coronal MPR and MIP images obtained in the portal-venous phase show porto-hepatic venous shunting, with the dilated portal vein (black arrow) communicating with the median hepatic vein (white arrow) through a focal vascular mass (open arrow).

Hepatic perfusion abnormalities are identified as an inhomogeneous attenuating pattern within the liver parenchyma. They are best seen during the early and late arterial phase, almost always disappearing in the hepatic parenchyma becoming homogeneous. In contrast to that seen in HHT, the perfusion abnormalities in the setting of cirrhosis usually are more focal, peripherally located, and wedge-shaped configuration on either coronal or axial projections.

With HHT, the perfusion abnormalities are frequently more diffuse and inhomogeneous or ill-defined [144–145].

Three types of hepatic vascular shunts exist in HHT: arteriovenous, arterioportal, and portovenous. Arteriovenous and arterioportal shunts are artery to vein shunts with early enhancement draining vein connecting to the hepatic vein or portal vein. Both are detected during the early arterial phase, with latter phases being less diagnostic. Portovenous shunts are seen in the hepatic phase, with a dilated portal vein branch (during the portal-venous phase) communicating with the large hepatic vein (Figure 1.53) [146].

1.14.4 Hepatic Infarction

Hepatic infarction is defined as areas of coagulation necrosis from hepatocyte death cells caused by local ischemia because of the obstruction of the circulation of the affected area by a thrombus or embolus.

It is uncommon because of the dual vascular supply from the hepatic artery and portal vein. Hepatic infarction may be iatrogenic (transarterial chemoembolization)

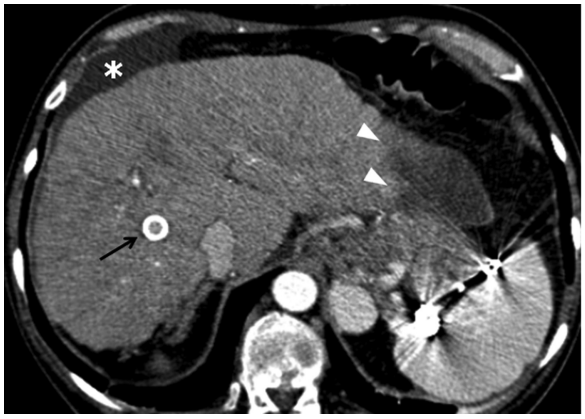

FIGURE 1.54
Hepatic infarction after HCC transarterial chemoembolization. Postcontrast CT image acquired during the arterial phase shows a hypodense, peripheral wedge-shaped area (arrowheads). Note a transjugular intrahepatic portosystemic shunt (arrow) for treatment of intractable ascites (asterisk).

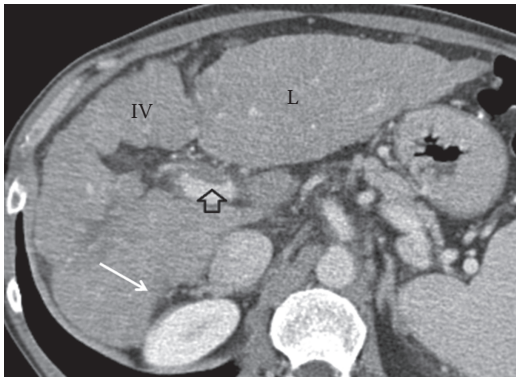

FIGURE 1.55
Cirrhosis. Postcontrast CT during portal-venous phase show the enlargement of hilar periportal space because of atrophy of medial segment of left lobe (IV). Liver also present irregular margins, enlargement of the left lobe (L) and a notch in posterior segments (arrow). Note the presence of portal vein thrombosis, which is a complication of liver cirrhosis (open arrow).

or posttraumatic (laceration of hepatic artery or portal vein). It can occur as a complication of liver transplantation; it may be secondary to vasculitis or infection [126]. Hepatic artery thrombosis leading to infarction most often occurs after liver transplantation has been reported in almost 3% of adult transplant recipients.

Unenhanced CT shows peripheral wedge-shaped, rounded, or irregularly shaped area of low attenuation of the liver. Bile leaks may be seen as a late sequel of large infarcts from ischemia necrosis of bile ducts epithelium. Gas formation has been described in sterile infarcts as well as infected ones [147].

Postcontrast images show a better defined area of lower attenuation to the surrounding liver (Figure 1.54). It manifests as perfusion defects in a geographic or segmental pattern with or without defined margins. Its enhancement pattern is patchy or heterogeneous because of nondisplaced vessels in the infarcted areas. Preservation of portal tracts is a feature worthy of emphasis because it helps to differentiate infarction from other causes of hypoattenuating foci (abscess, biloma) [139].

Focal steatosis is also included in the differential diagnosis; however, it develops in specific site and vascular structures are preserved.

1.15 Diffuse Liver Disease

1.15.1 Cirrhosis

Liver cirrhosis is a chronic response to repetitive hepatic insult, which is characterized by regenerative nodules and fibrosis [148]. The changes of cirrhosis occur cyclically with episodes of impaired circulation, injury inflammation, fibrosis, and regeneration. Obstruction of intrahepatic vascular bed by fibrosis and regenerative nodules results in portal hypertension. Liver cirrhosis could be classified into (1) micronodular, with nodule less than 3 mm and thin septa; (2) macronodular, with nodules more than 3 mm and thick septa, (3) mixed.

The main causes of liver cirrhosis include viral infection, such as hepatitis B and C and alcohol abuse. Secondary causes should be hemochromatosis, biliary obstruction, biliary primary cirrhosis, metabolic disorder, and storage disease. Complications of liver cirrhosis result in portal hypertension and development of hepatofugal portal flow via multiple portosystemic venous collateral channels, which lead to hepatic encephalopathy and variceal hemorrhage [149].

MDCT of the liver in cirrhotic patient should evaluate changes in liver morphology, complications of portal hypertension and exclude the risk of liver hepatocarcinogenesis.

A primary morphologic change on liver parenchyma is the enlargement of hilar periportal space because of atrophy of medial segment of left lobe (IV segment) [150]. Morphologic changes in advanced cirrhosis include the atrophy of the right lobe, the enlargement of the left and caudate lobe, a nodular liver contour, and widened fissures between liver segments, this latter aspect is detectable especially on alcoholic cirrhosis [151,152] (Figure 1.55).

Fifteen percent of patients with advanced cirrhosis develop an area of confluent fibrosis. CT appearance is a wedge-shaped area of lesser attenuation than adjacent liver parenchyma at pre-and postcontrast CT images (Figure 1.56)

CT extrahepatic findings of liver cirrhosis include portal vein thrombosis, ascitis, splenomegaly and portosystemic shunts (Figures 1.55 through 1.57).

Cirrhosis-associated hepatocellular nodules result from the localized proliferation of hepatocytes and their supporting stroma [153]. Most are benign regenerative nodules; however, regenerative nodules may progress along a well-described carcinogenic pathway to become dysplastic nodules or HCCs [154]. The imaging evaluation of cirrhosis-associated hepatocellular nodules therefore is important for their optimal management. There are four classes of lesions that are characteristically found in the cirrhotic liver; regenerative nodules, dysplastic foci, dysplastic nodules, and HCC. Regenerative nodules also may be classified according to size as either micronodules (<3 mm) or macronodules (≥3 mm). Giant regenerative nodules with a diameter of 5 cm have been described, but they are rare. Lesions with dysplastic features that do not satisfy the histologic criteria for malignancy or invasion are described as either (1) dysplastic foci (<1 mm in diameter) or (2) dysplastic nodules (≥1 mm in diameter). Dysplastic nodules usually occur in the setting of cirrhosis and may be classified as low or high grade, according to the degree of dysplasia. According to the latest guidelines from the American Association for the Study of Liver Diseases, dysplastic nodules should not be treated or managed as cancers, and patients with known or suspected dysplastic nodules should not be monitored more aggressively than patients without such nodules [155]. Regenerative nodules and low-grade dysplastic nodules are predominantly portally perfused and, after contrast medium administration, show enhancement similar to that of the surrounding liver (Figure 1.58) [156,157]. As dedifferentiation progresses within these nodules, angiogenic pathways are activated that induce new vessel formation, which manifests as an increased density of unpaired arteries and capillary units [156]. This development leads to an increasing shift from predominant venous perfusion to predominant arterial perfusion as low-grade dysplastic nodules and HCCs become high-grade lesions (Figure 1.59) [155].

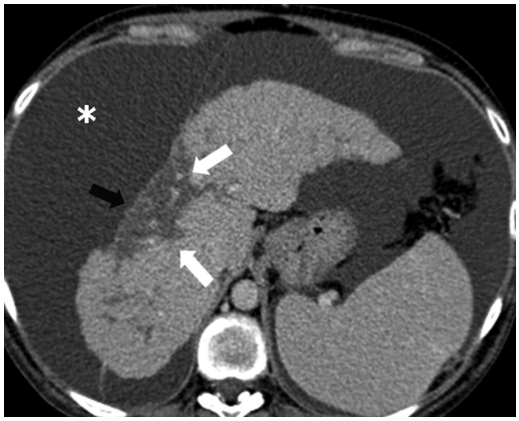

FIGURE 1.56
Confluent hepatic fibrosis in liver cirrhosis. Postcontrast CT scan shows wedge-shaped lesion (white arrow) of lower attenuation than adjacent liver parenchyma in the anterior segment of the right lobe. Deep retraction of liver capsule is seen (black arrow). Note the lot amount of intra-abdominal fluid (asterisk).

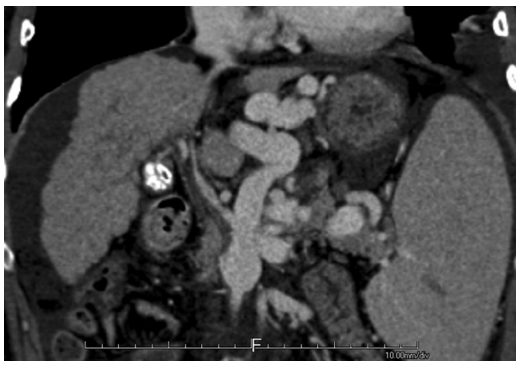

FIGURE 1.57
Complications in liver cirrhosis. Postcontrast CT image show portal hypertension signs such as thrombosis of portal vein, splenomegaly, and portosystemic venous collateral channels.

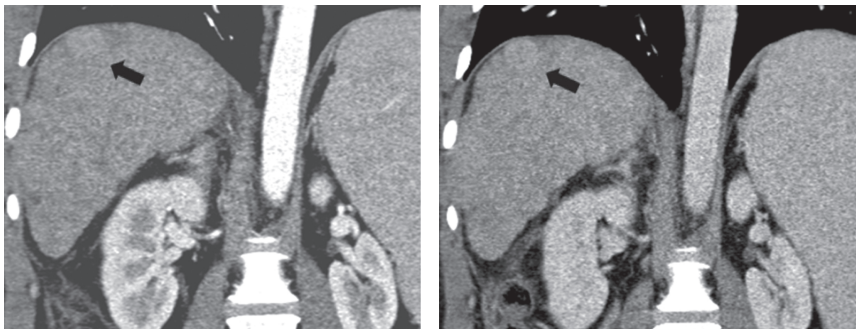

(a) (b)

FIGURE 1.58
Regenerative nodule. (a and b) Postcontrast CT images acquired during arterial and portal-venous phase show a tiny hypervascular subcapsular lesion in liver segment VIII with prolonged enhancement during the portal-venous phase (arrow).

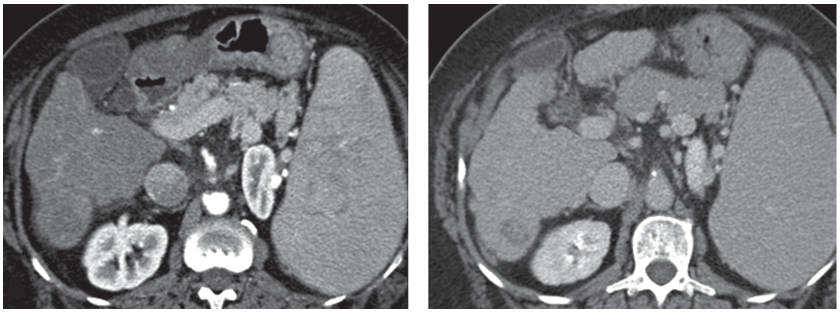

(a) (b)

FIGURE 1.59
Dysplastic nodule. (a) Postcontrast CT image during arterial phase reveals any focal live lesion. (b) Postcontrast CT image during delayed phase (3 minutes) show a hypoattenuating focal liver lesion in liver segment V, which was confirmed to be a dysplastic nodule at liver biopsy.

The increasingly dedifferentiated nodules appear more markedly enhanced on early arterial phase images obtained after the intravenous injection of a contrast agent, with more pronounced washout on venous phase images and equilibrium phase images [158]. The major shift in angiogenesis typically occurs during the transition from low-grade to high-grade dysplasia.

Although the term siderotic nodule is not included in the International Working Party lexicon, it is mentioned here because it appears commonly in the radiology literature. The term was coined by radiologists to describe cirrhosis-associated nodules with high levels of endogenous iron.

1.15.2 Steatosis

Steatosis or fatty change is an excessive accumulation of triglycerides within the hepatocytes [159]. Several toxic and metabolic disorders may produce it such as alcohol abuse, obesity, diabetes mellitus, hepatitis, and drugs. This is generally a reversible change, but it is often undetectable at clinical or laboratory examination.

Fatty change can have a correspondingly variable appearance on images with patterns of fatty liver such as diffuse and uniform, focal, multifocal, and confusing.

At unenhanced MDCT, fatty infiltration results in a lowering of the liver attenuation. The normal liver has an attenuation of about 8 HU greater than that of the spleen [160,161]. Mild steatosis can be diagnosed when the liver attenuation is slightly less than that of the spleen; marked steatosis leads in an attenuation value lower than that of the intrahepatic blood vessels (Figure 1.60).

Although fatty change may be diagnosed also on contrast-enhanced MDCT, postcontrast images evaluation is less reliable and specific. After contrast medium administration, significant fatty infiltration can be depicted if liver attenuation in less than that of muscle or if it has an attenuation value of at least 25 HU lower than that of the spleen [162].

Focal fatty infiltration, perivascular fat distributions, and residual foci of unaffected liver parenchyma surrounded by fatty infiltration may all be confused with neoplastic lesions at MDCT. Therefore, the identification of specific findings is crucial to achieve a correct diagnose.

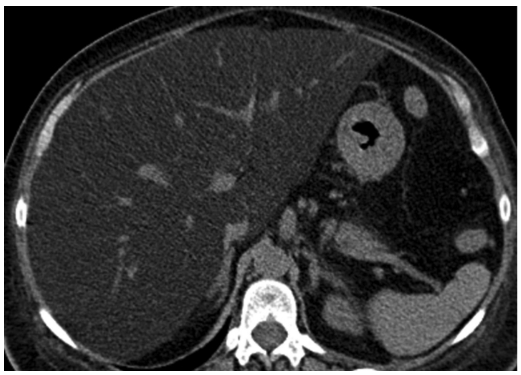

FIGURE 1.60
Liver steatosis. Unenhanced CT image shows a lower attenuation of liver parenchyma compared to that of spleen. Note the clear visualization of intrahepatic liver vessels.

Focal fatty infiltration commonly has a segmental or lobar distribution. These often irregularly shaped lesions typically extend to liver capsule, without associated bulging of liver contour. Moreover, vessels coursing through the area of abnormality are not displaced common locations or fatty infiltrations are in the anterior part of the segment IV, adjacent to the falciform ligament [163].

1.15.3 Hemochromatosis

The term hemochromatosis refers to iron overload disorders; it can be classified as (1) primary, when it origins from a genetic disturbance [human leukocyte antigen) that promotes the increase of iron absorption, or (2) secondary to chronic disease or multiple transfusions. Hemochromatosis can lead to chronic liver disease, cirrhosis, and often HCC [164]. Basically, iron is stored in the reticuloendothelial cells; an iron overload is accumulated within the hepatocytes producing inflammation and liver damage. Unenhanced MDCT shows a

homogenous increase in the attenuation of the hepatic parenchyma to 70 HU or more (Figure 1.61) [165,166]. CT has low sensitivity (63%) and high specificity (96%) for the diagnosis of iron over load. Certain conditions, such as associated steatosis, can reduce the sensitivity still further reducing the hepatic parenchyma attenuation [167]. Other factors, such as Wilson disease, colloidal gold treatment, and long-term administration of amiodarone, also increase the liver attenuation, which decrease the diagnostic specificity of CT. It has been shown that a positive linear correlation exists between CT attenuation and iron overload at both "single energy" CT and "dual energy CT." Moreover, because of the high atomic number of iron, the increase of hepatic parenchyma attenuation can be better appreciated with a lower kVp (80) than conventional kVp (120). [168] In advanced stage of hemocrhomatosis, liver shows typical pattern of cirrhosis, postcontrast acquisitions are useful to avoid the presence of liver neoplasms.

1.15.4 Wilson Disease

Hepatolenticular degeneration, more commonly known as Wilson disease, is an autosomal recessive disorder characterized by increased intestinal uptake of copper and subsequent deposition in the liver, basal ganglia, cornea (Kayser–Fleischer rings), and other tissues. It can manifest as acute and even fulminant hepatitis or with rapid progression to liver cirrhosis: progression to HCC is extremely rare. Patients with Wilson disease present low level of ceruloplasmin. As well as liver hemochromatosis, deposition of copper in the liver determines an increasing of liver attenuation. This finding is variable, however, in part because the associated fatty infiltration decreased liver attenuation, preventing any appreciable increase in attenuation. Spectrum of imaging injury is nonspecific; changes of fatty infiltration or cirrhosis are indistinguishable from those of other entities [126,169,170].

1.16 Local Treatment

Local-regional treatment play a key role in the management of HCC and recently also for treatment of liver metastases. Image-guided tumor ablation is recommended in patients with early stage HCC; moreover, it has been shown that it is the treatment of choice for lesion smaller than 2 cm compared to liver resection [171]. Radiofrequency (RF) ablation has shown superior response and greater survival benefit to other percutaneous technique such as ethanol injection.

After the procedure, CT examination reveals a well-defined, delineated, rounded hypodense area without contrast enhancement after contrast material injection. The area of RF-induced coagulated tissue forms a necrotic "scar" that usually shrinks with time, but most often very slowly (Figure 1.62) [172].

During the arterial phase, a thin peripheral rim related to inflammatory alteration is usually visible, sometimes a wedge-shaped peripheral area due to a transitory arteroportal shunt is also appreciable. Local regrowth shows the same radiological findings of primary tumor (Figure 1.63) [173].

Transcatheterarterial chemoembolization (TACE) is the standard of care for patients with multinodular HCC out of criteria for liver transplantation in an intermediate stage of disease. A limit of CT in the evaluation of HCC post-TACE is the high density of high-iodized oil within the tumor and its artifact. Embolic microspheres, which

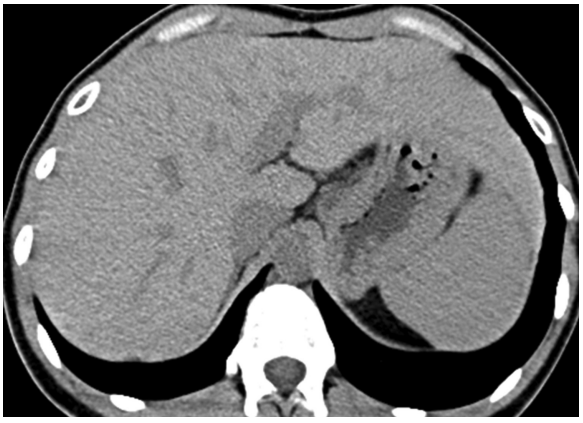

FIGURE 1.61
Liver hemochromatosis. Unenhanced CT image shows diffuse, marked increased attenuation (higher than that of the spleen) secondary to iron deposition.

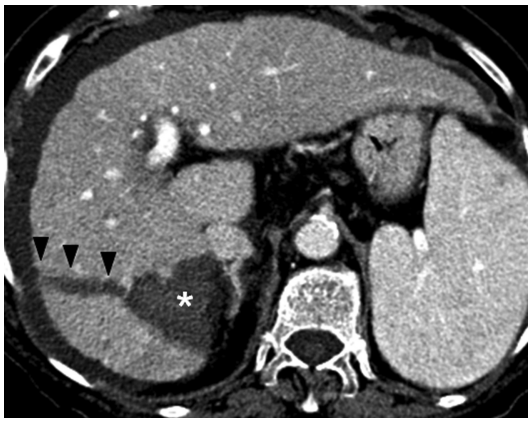

FIGURE 1.62
Radiofrequency ablation of HCC. Postcontrast image acquired on portal-venous phase shows a large hypoattenuating area in liver segment VI without contrast enhancement. Note the "ghost" of the lesion (asterisk) and the track released by the needle (arrowheads). (Courtesy of M. Bezzi, MD.)

have the ability to release a drug in a controlled and sustained fashion, have been shown to substantially increase the safety and efficacy of TACE in comparison to conventional ethiodized oil-based regimens (Figure 1.64).

1.17 Complication Post-Liver Transplantation

Liver transplantation is currently an accepted first-line treatment in patients with end-stage acute or chronic liver disease, but postoperative complications may limit the long-term success of transplantation. It is important for the radiologist to be aware of the most common anastomotic techniques and expected postoperative imaging findings [174,175].

Posttransplantaion complications are broadly classified into vascular, biliary, and other disorders. Vascular complications include hepatic artery thrombosis-stenosis, pseudoaneurysm, hepatic infarct, and portal vein, IVC or hepatic veins thrombosis-stenosis. After rejection, vascular complications are the most common cause of graft failure and should be considered in patients with liver failure, bile leak, and abdominal bleeding septicemia [176]. Biliary complications include bile duct obstruction, anastomotic and nonanastomotis stenosis, bile leak, biloma, cholangitis, and biliary necrosis. Other complications of liver transplantation include hematoma, abscess, infection, recurrent malignancy, and lymphoproliferative disorder. Hepatic artery stenosis-thrombosis is the most common vascular complication occurring in 2%–12% of cases, vascular stenosis is usually seen at anastomotic level as a focal narrowing [177,178]. Three-dimensional reconstruction of CT angiographic data allows reliable identification of this finding (Figure 1.65). Hepatic artery thrombosis and stenosis can lead to biliary ischemia, since the hepatic artery is the only vascular supply to bile ducts. Hepatic artery pseudoaneurysm is an uncommon complication that generally develops at the site of anastomosis or a complication of angioplasty. Treatment options for an extrahepatic pseudoaneurysm include surgical resection, embolization, and exclusion with stent placement. Contrast-enhanced CT shows a focal lesion with central enhancement that followed arterial blood-pool attenuation (Figure 1.66).

Portal vein complications following liver transplantation are relatively unusual, occurring in 1%–3% of cases and results from faulty surgical technique, vessel misalignment, and differences in caliber of anastomoted vessels.

Although in less graphic manner compared with MR-cholangiopancreatography, CT can also show biliary complications, which occur in an estimated 25% of liver transplantation recipients, usually within the first 3 months after transplantation.

Biliary complications include leak, stricture, obstruction, and stone formation (Figure 1.67). Transplant recipients have external biliary drainage catheters (T-tube) in the

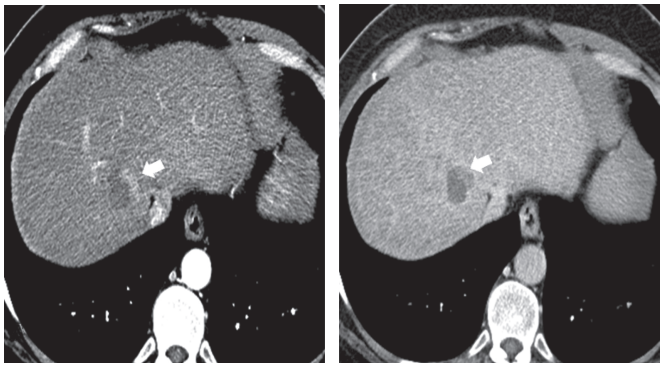

(a) (b)

FIGURE 1.63
Hepatocellular carcinoma recurrence after RF ablation. (a and b) CT images acquired during the arterial and delayed phases (DPs) show a tiny hypervascular lesion with wash-out during the DP, located in the medial margin of the treated lesion.

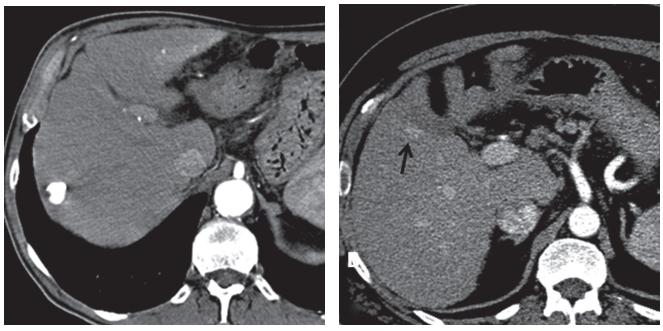

(a) (b)

FIGURE 1.64
Hepatocellular carcinoma treated with TACE. (a) Postcontrast CT image of HCC treated with iodized oil show the high attenuation of the lesion where is difficult detect disease recurrence. (b) TACE performed with DC-beads allows the identification of a small hypervascular peripheral lesion due to disease recurrence.

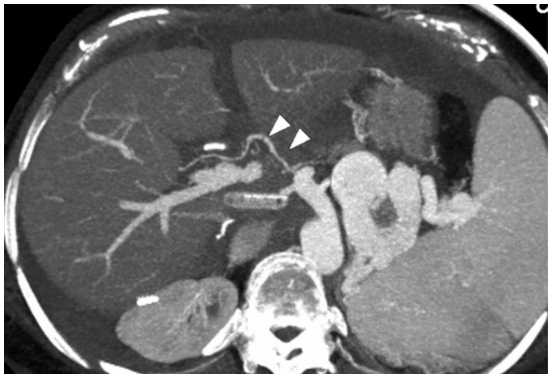

FIGURE 1.65
Complication of liver transplantation. Axial MIP image shows marked stenosis of the transplant hepatic artery at the anastomosis (arrowheads).

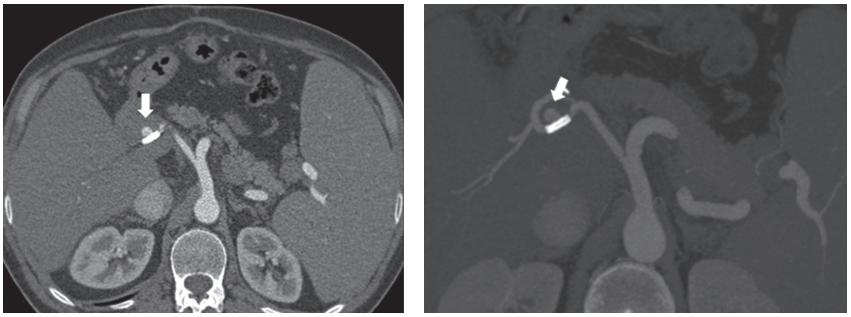

(a) (b)

FIGURE 1.66
Complication of liver transplantation. (a and b) Postcontrast CT image during the arterial phase and its MIP reconstruction on axial plane revealed an extrahepatic artery pseudoaneurysm at vascular anastomosis treated with endovascular stent. Note that the aneurysm is not completely excluded (arrow).

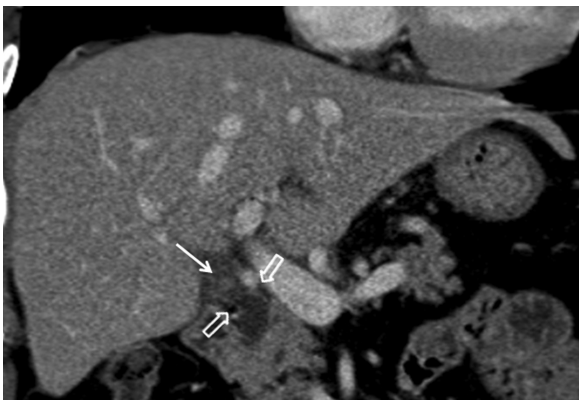

FIGURE 1.67
Complication of liver transplantation. Coronal postcontrast CT image shows a biliary stricture at anastomosis level (open arrows). Note the presence of a bile duct stone (arrow).

postoperative period, so it is fast and easy to perform cholangiography to determine the state of the biliary system when a complication is suspected. The choledochocholedochostomy is the type of biliary anastomosis that is most frequently employed, accompanying a cholecystectomy.

Patients are also at increased risk for developing malignancy, especially non–Hodgkin lymphoma and squamous cell skin cancer because of immunosuppressive therapy [3]. Lymphoma can involve any organ, including the liver graft itself, where it is seen as multiple hypoattenuating nodules. In patients with a neoplasm treated with liver transplantation (HCC, CCC) the primary tumor can recur in the graft or at any other location.

References

1. Couinaud C. *The Liver: Anatomical and Surgical Studies*. Paris, France: Masson, 1957; 9–12.
2. Bismuth H. Surgical anatomy and anatomical surgery of the liver. *World J Surg* 1982; 6: 3–8.
3. Catalano OA, Singh AH, Uppot RN et al. Vascular and biliary variants in the liver: implications for liver surgery. *Radiographics* 2008; 28: 359–378.
4. Makuuchi M, Hasegawa H, Yamazaki S et al. The inferior right hepatic vein ultrasonic demonstration. *Radiology* 1983; 148: 213–217.
5. Marin D, Catalano C, De Filippis G et al. Detection of hepatocellular carcinoma in patients with cirrhosis: added value of coronal reformations from isotropic voxel with 64-MDCT. *Am J Roentgenol* 2009; 192: 180–187.
6. Maetani YS, Ueda M, Haga H et al. Hepatocellular carcinoma in patients undergoing living-donor liver transplantation. *Intervirology* 2008; 51: 46–51.
7. Abdelmoumene A, Chevallier P, Charlon M et al. Detection of liver metastases under 2 cm: comparison of different acquisition protocols in four row multidetctor-CT (MDCT). *Eur Radiol* 2005; 15: 1881–1887.
8. Bae KT. Intravenous contrast medium administration and scan timing at CT. consideration and approaches. *Radiology* 2010; 256: 32–61.
9. Heiken JP, Brink JA, McClennan BL et al. Dynamic incremental CT: effect of volume and concentration of contrast material and patient weight on hepatic enhancement. *Radiology* 1995; 195(2): 353–357.
10. Yamashita Y, Komohara Y, Takahashi M et al. Abdominal helical CT: evaluation of optimal doses of intravenous contrast material—a prospective randomized study. *Radiology* 2000; 216(3): 718–723.
11. Kondo H, Kanematsu M, Goshima S et al. Abdominal multidetector CT in patients with varying body fat percentages: estimation of optimal contrast material dose. *Radiology* 2008; 249(3): 872–877.
12. Tello R, Seltzer SE, Polger M et al. A contrast agent delivery nomogram for hepatic spiral CT. *J Comput Assist Tomogr* 1997; 21(2): 236–245.
13. Yanaga Y, Awai K, Nakaura T et al. Optimal contrast dose for depiction of hypervascular hepatocellular carcinoma at dynamic CT using 64-MDCT. *AJR Am J Roentgenol* 2008; 190(4): 1003–1009.
14. Foley WD, Mallisee TA, Hohenwalter MD et al. Multiphase hepatic CT with a multirow detector CT scanner. *AJR Am J Roentgenol* 2000; 175(3): 679–685.

15. Goshima S, Kanematsu M, Kondo H et al. MDCT of the liver and hypervascular hepatocellular carcinomas: optimizing scan delays for bolus-tracking techniques of hepatic arterial and portal venous phases. *AJR Am J Roentgenol* 2006; 187(1): W25–W32.
16. Yanaga Y, Awai K, Nakayama Y et al. Optimal dose and injection duration (injection rate) of contrast material for depiction of hypervascular hepatocellular carcinomas by multidetector CT. *Radiat Med* 2007; 25(6): 278–288.
17. Sultana S, Awai K, Nakayama Y et al. Hypervascular hepatocellular carcinomas: bolus tracking with a 40-detector CT scanner to time arterial phase imaging. *Radiology* 2007; 243(1): 140–147.
18. Schindera ST, Nelson RC. Hepatobiliary imaging by MDCT Springer, 2008.
19. Baron RL. Understanding and optimizing use of contrast material for CT of the liver. *AJR Am J Roentgenol* 1994; 163(2): 323–331.
20. Hollett MD, Jeffrey RB Jr, Nino-Murcia M et al. Dual-phase helical CT of the liver: value of arterial phase scans in the detection of small (< or = 1.5 cm) malignant hepatic neoplasms. *AJR Am J Roentgenol* 1995; 164(4): 879–884.
21. Oliver JH 3rd, Baron RL. Helical biphasic contrast-enhanced CT of the liver: technique, indications, interpretation, and pitfalls. *Radiology* 1996; 201(1): 1–14.
22. Oliver JH 3rd, Baron RL, Federle MP, Rockette HE Jr. Detecting hepatocellular carcinoma: value of unenhanced or arterial phase CT imaging or both used in conjunction with conventional portal venous phase contrast-enhanced CT imaging. *AJR Am J Roentgenol* 1996; 167(1): 71–77.
23. Mitsuzaki K, Yamashita Y, Ogata I et al. Multiple-phase helical CT of the liver for detecting small hepatomas in patients with liver cirrhosis: contrast-injection protocol and optimal timing. *AJR Am J Roentgenol* 1996; 167(3): 753–757.
24. Lim JH, Choi D, Kim SH et al. Detection of hepatocellular carcinoma: value of adding delayed phase imaging to dual-phase helical CT. *AJR Am J Roentgenol* 2002; 179(1): 67–73.
25. Lacomis JM, Baron RL, Oliver JH 3rd et al. Cholangiocarcinoma: delayed CT contrast enhancement patterns. *Radiology* 1997; 203(1): 98–104.
26. Johnson TR, Krauss B, Sedlmair M et al. Material differentiation by dual energy CT: initial experience. *Eur Radiol* 2007 Jun; 17(6): 1510–1517.
27. Kalender WA. CT: the unexpected evolution of an imaging modality. *Eur Radiol* 2005 Nov; 15 Suppl 4: D21–D24.
28. Kalender WA, Perman WH, Vetter JR, Klotz E. Evaluation of a prototype dual-energy computed tomographic apparatus. I. Phantom studies. *Med Phys* 1986 May–Jun; 13(3): 334–339.
29. Graser A, Johnson TR, Chandarana H et al. Dual energy CT: preliminary observations and potential clinical applications in the abdomen. *Eur Radiol* 2009 Jan; 19(1): 13–23. Review.
30. Coursey CA, Nelson RC, Boll DT et al. Dual-energy multidetector CT: how does it work, what can it tell us, and when can we use it in abdominopelvic imaging? *Radiographics* 2010 Jul-Aug; 30(4): 1037–1055.
31. Yeh BM, Shepherd JA, Wang ZJ et al. Dual-energy and low-kVp CT in the abdomen. *AJR Am J Roentgenol* 2009 Jul; 193(1): 47–54. Review.
32. Silva AC, Morse BG, Hara AK et al. Dual-energy (spectral) CT: applications in abdominal imaging. *Radiographics* 2011 Jul-Aug; 31(4): 1031–1046; discussion 1047–1050.
33. Mettler FA Jr, Huda W, Yoshizumi TT et al. Effective Doses in Radiology and diagnostic nuclear medicine: a Catalog; Fred. *Radiology* 2008 Jul; 248(1): 254–263.
34. ICRP. *Recommendations of the International Commission on Radiological Protection (Users Edition)*. ICRP Publication 103. Ann. ICRP 2007; 37: 2–4.
35. Marin D, Nelson RC, Rubin GD et al. Body CT: technical advances for improving safety. *AJR Am J Roentgenol* 2011 Jul; 197(1): 33–41.
36. Barrett T, Bowden DJ, Shaida N et al. Virtual unenhanced second generation dual-source CT of the liver: is it time to discard the conventional unenhanced phase? *Eur J Radiol* 2012; 81: 1438–45.
37. Zhang LJ, Peng J, Wu SY et al. Liver virtual non-enhanced CT with dual-source, dual-energy CT: a preliminary study. *Eur Radiol* 2010 Sep; 20(9): 2257–2264.
38. Marin D, Nelson RC, Samei E et al. Hypervascular liver tumors: low tube voltage, high tube current multidetector CT during late hepatic arterial phase for detection—initial clinical experience. *Radiology* 2009 Jun; 251(3): 771–779.
39. McNitt-Gray MF. AAPM/RSNA physics tutorial for residents: topics in CT, radiation dose in CT, Michael F. *RadioGraphics* 2002; 22: 1541–1553.
40. Hara AK, Paden RG, Silva AC et al. Iterative reconstruction technique for reducing body radiation dose at CT: feasibility study. *AJR Am J Roentgenol* 2009 Sep; 193(3): 764–771. Erratum in: *AJR Am J Roentgenol* 2009 Oct; 193(4): 1190.
41. Martinsen ACT, Sæther HK. Iterative reconstruction reduces abdominal CT dose. *EURR*-5493; 1–5.
42. Mitsumori LM, Shuman WP, Busey JM et al. Adaptive statistical iterative reconstruction versus filtered back projection in the same patient: 64 channel liver CT image quality and patient radiation. *Eur Radiol*. doi 10.1007/s00330-011-2186-3.
43. Schindera ST, Diedrichsen L, Müller HC et al. Iterative reconstruction algorithm for abdominal multidetector CT at different tube voltages: assessment of diagnostic accuracy, image quality, and radiation dose in a phantom study. *Radiology* 2011 Aug; 260: 454–62.
44. Marin D, Nelson RC, Schindera ST et al. Low-tube-voltage, high-tube-current multidetector abdominal CT: improved image quality and decreased radiation dose with adaptive statistical iterative reconstruction algorithm, initial clinical experience. *Radiology* 2010 Jan; 254(1): 145–153.
45. Fischer MA, Reiner CS, Raptis D et al. Quantification of liver iron content with CT-added value of dual-energy. *Eur Radiol* 2011 Aug; 21(8): 1727–1732. Epub 2011 Apr 7.
46. Joe E, Kim SH, Lee KB et al. Feasibility and accuracy of dual-source dual-energy CT for noninvasive determination of hepatic iron accumulation. *Radiology* 2012 Jan; 262(1): 126–135. Epub 2011 Nov 21.

47. Van Sonnenberg E, Wroblicka JT, D'Agostino HB et al. Symptomatic hepatic cysts. Percutaneous drainage and sclerosis. *Radiology* 1994; 190: 387–392.
48. Mortelè KJ, Ros PR. Cystic focal liver lesions in the adult: differential CT and MR imaging features. *Radiographics* 2001; 21: 895–910.
49. Brancatelli G, Federle MP, Vilgrain V et al. Fibroplolycystic liver disease: CT and MR imaging findings. *Radiographics* 2005; 25: 659–670.
50. Lewis KH, Chezmar JL. Hepatic metastases. *Magn Reson Imaging Clin N Am* 1997; 5: 241–253.
51. SugawaraY, Yamamoto J, Yamasaki S et al. Cystic liver metastases from colorectal cancer. *J Surg Oncol* 2000; 74: 148–152.
52. Barnes PF, DeCock KM, Reynolds TN, Ralls PW. A comparison of amebic and pyogenic abscess of the liver. *Medicine* 1987; 66: 472–483.
53. Huang CJ, Pitt HA, Lipsett PA et al. Pyogenic hepatic abscess. *Ann Surg* 1996; 223: 600–609.
54. Mortele KJ, Segatto E, Ros PR. The infected liver: radiologic-pathologic correlation *Radiographics* 2004; 24: 937–955.
55. Pitt HA. Surgical management of hepatic abscesses. *World J Surg* 1990; 14: 498–504.
56. Jeffreey RB Jr, Tolentino CS, Chang CF, Federle MP. CT of small pyogenic hepatic abscesses: the cluster sign. *Am J Roentgenol* 1988; 151: 487–489.
57. Van Sonnenberg E, Mueller PR, Schiffman HR et al. Intrahepatic amebic abscesses: indications for and results of percutaneous catheter drainage. *Radiology* 1985; 156: 631–635.
58. Samuelson J, Von Lichtenberg F. Infectious diseases. In: Cotran RS, Kumar V, Robbins SL eds. *Pathologic Basis of Disease*. 5th ed. Philadelphia, PA: Saunders, 1994; 305–377.
59. Radin DR, Ralls PW, Colletti PM, Halls JM. CT of amebic liver abscess. *AJR Am J Roentgenol* 1988; 150: 1297–1301.
60. Suwan Z. Sonographic findings in hydatid disease of the liver: comparison with other imaging methods. *Ann Trop Med Parasitol* 1995; 89: 261–269.
61. Mergo PG, Ros PB. MR Imaging of inflammatory disease of the liver. *Magn Reson Imaging Clin N Am* 1997; 5: 367–376.
62. Beggs I. The radiology of hydatid disease. *Am J Roentgenol* 1985 145: 539–548.
63. Kalovidouris A, Pissiotis C, Pontifex G et al. CT characterization of multivesicular hydatid cysts. *J Comput Assisted Tomogr* 1986; 10: 428–431.
64. Pedrosa I, Saiz A, Arrazola J et al. Hydatid disease. Radiologic and pathologic features and complications. *Radiographics* 2000; 20: 795–817.
65. Horton KM, Bluemke DA, Hrban RH et al. CT and MR imaging of benign hepatic and biliary tumors. *Radiographics* 1999; 19: 431–451.
66. Semelka R, Hussain SM, Marcos HB, Woosley JT. Biliary hamartomas: solitary and multiple lesion shown on current MR technique including gadolinium enhancement. *J Magn Reson Imaging* 1999; 10: 196–201.
67. Choi BI, Lim JH, Han MC et al. Biliary cystadenoma and cystadenocarcinoma: CT and ultrasonography findings. *Radiology* 1989; 171: 57–61.
68. Palacios E, Shannon M, Solomon C, Guzman M. Biliary cystadenoma: ultrasound, CT, and MRI. *Gastrointest Radiol* 1990; 15: 313–316.
69. Craig J, Peters R, Edmonson H. *Tumors of the Liver and Intrahepatic Bile Ducts (Second Series)*. Atlas of tumor pathology, vol fascicle 26. Washington, DC: Armed Forces Institute of Pathology, 1989.
70. Hussain SM, Terkivatan T, Zondervan PE et al. Focal nodular hyperplasia: findings at state-of-art MR imaging, US, CT, and pathologic analysis. *Radiographics* 2004; 24: 3–17.
71. Welch TJ, Sheedy PF II, Johnson CM et al. Focal nodular hyperplasia and hepatic adenoma: comparison of angiography, CT, US and scintigraphy. *Radiology* 1985; 156: 593–595.
72. Mortele KJ, Praet M, Van Vlierberghe H et al. CT and MR imaging findings in focal nodular hyperplasia of the liver: radiologic-pathologic correlation. *AJR Am J Roentgenol* 2000; 175: 687–692.
73. Shamsi K, De Shepper A, Degryse H, Deckers F. Focal nodular hyperplasia of the liver: radiologic findings. *Abdom Imaging* 1993; 18: 32–38.
74. Brancatelli G, Federle MP, Katyal S, Kapoor V. Hemodinamic characterization of focal nodular hyperplasia using three-dimensional volume-rendered multidetector CT angiography. *AJR Am J Roentgenol* 2002; 179: 81–85.
75. Choi CS, Freeny PC. Triphasic helical CT of hepatic focal nodular hyperplasia: incidence of atypical findings. *AJR Am J Roentgenol* 1998; 170: 391–395.
76. Kerlin P, Davis GL, McGill DB et al. Hepatic adenoma and focal nodular hyperplasia: clinical, pathologic, and radiologic features. *Gastroenterology* 1983; 84: 994–1002.
77. Ichikawa T, Federle MP, Grazioli L, Nalesnik M. Hepatocellular adenoma: multiphasic CT and histopathologic findings in 25 patients. *Radiology* 2000; 214: 861–868.
78. Grazioli L, Federle MP, Brancatelli G et al. Hepatic adenoma: imaging and pathologic findings. *Radiographics* 2001; 21: 877–892.
79. Ruppert-Kholmayr AJ, Uggowitzer MM, Kugler C et al. Focal nodular hyperplasia and hepatocellular adenoma of the liver, differentiation with multiphasic helical CT. *AJR Am J Roentgenol* 2001; 176: 1493–1498.
80. Grazioli L, Morana G, Kirchin MA, Schneider G. Accurate differentiation of focal nodular hyperplasia from hepatic adenoma at gadobenate dimeglumine-emhanced MR imaging: prospective study. *Radiology* 2005; 236: 166–177.
81. Wright TL, Venook AP, Millward-Sadler GH. Hepatic tumors. In: Millward-Sadler GH, Wright R, Arthur MJOP, eds. *Wrght's Liver and Biliary Disease*. vol 2, 3rd ed. Philadelphia, PA: WB Saunders, 1992; 1079–1121.
82. Belli L, De Carlis L, Beati S et al. Surgical treatment of syntomatic giant hemangiomas of the liver. *Surg Gynecol Obstet* 1992; 174: 474–478.
83. Whitehouse RW. Computed tomography attenuation measurements for the characterization of hepatic hemangiomas. *Br J Radiol* 1991; 64: 1019–1022.
84. Quinn SF, Benjamin GG. Hepatic cavernous hemangiomas: simple diagnostic sign with dynamic bolus CT. *Radiology* 1992; 182: 545–548.

85. Hanafusa K, Ohashi I, Himeno Y et al. Hepatic hemangioma: findings with two phase CT. *Radiology* 1995; 196: 465–469.
86. Wachsberg RH, Cho KC, Adekosan A. Two leiomyomas of the liver in an adult with AIDS: CT and MR appearance. *J Comput Assist Tomogr* 1994; 18: 156–157.
87. Marin D, Catalano C, Rossi M et al. Gadobenate dimeglumine-enhanced MR imaging of primary leiomyoma of the liver. *J Magn Reson Imag* 2008; 28: 755–758.
88. Herzberg AJ, MacDonald JA, Tucker JA et al. Primary leiomyoma of the liver. *Am J Gastroenterol* 1990; 85: 1642–5.
89. Bergeron P, Oliva VL, Lalonde L et al. Liver angiomyolipoma: classic and unusual presentations. *Abdom Imaging* 1994; 19: 543–545.
90. Chang JC, Lee YW, Kim HJ. Preoperative diagnosis of angiomyolipoma of the liver. *Abdom Imaging* 1994; 19: 546–548.
91. World Health Organization. mortality database. Available from: http//www.who.int/whosis/en (2010)
92. Bosch FX, Ribes J, Diaz M, Cleries R. Primary liver cancer: worldwide incidence and trends. *Gastroenterology* 2004; 127: 5–16.
93. Libbrecht L, Bielen D, Verslype C et al. Focal lesions in cirrhotic explant livers: pathological evaluation and accuracy of pretransplantation imaging examinations. *Liver Transpl* 2002; 8: 749–761.
94. Boone JM. Multidetector CT: opportunities, challenges, and concerns associated with scanners with 64 or more detector rows. *Radiology* 2006; 241: 334–337.
95. Marin D, Catalano C, De Filippis G et al. Detection of hepatocellular carcinoma in patients with cirrhosis: added value of coronal multiplanar reformations from isotropix voxel with 64-MDCT. *AJR Am J Roengenol* 2009; 192: 775–782.
96. Bruix J, Sherman M, Llovet JM et al. EASL panel of experts on HCC. Clinical management of hepatocellular carcinoma. Conclusions of the Barcelona-2000 EASL conference. European association for the study of the liver. *J Hepatol* 2001; 35: 421–430.
97. Baron RL, Oliver JH III, Confer S et al. Screening cirrhosis for hepatocellular carcinoma (HCC) with helical contrast CT: specificity. *Radiology* 1997; 2005: 143.
98. Kutami R, Nakashima Y, Nakashima O et al. Pathomorphologic study on the mechanism of fatty change in small hepatocellular carcinoma of humans. *J Hepatol* 2000; 33: 282–289.
99. Iannaccone R, Laghi A, Catalano C et al. Hepatocellular carcinoma of unenhanced and delayed phase multi detector row helical CT in patients with cirrhosis. *Radiology* 2005; 234: 460–467.
100. Lim JH, Choi D, Kim SH et al. Detection of hepatocellular carcinoma: value of adding delayed phase to dual-phase helical CT. *AJR Am J Roentgenol* 2002; 179: 67–73.
101. Hawang GJ, Kim MJ, Yhoo HS, Lee JT. Nodular hepatocellular carcinomas: detection with arterial-, portal- and delayed-phase images at spiral CT. *Radiology* 1997; 202: 383–388.
102. Kim SE, Lee HC, Shim JH et al. Noninvasive diagnostic criteria for hepatocellular carcinoma in hepatic masses larger than 2 cm in a hepatitis B virus-endemic area. *Liver Int* 2011; 31: 1469–1477.
103. Luca A, Caruso S, Milazzo M et al. Multidetector-row computed tomography (MDCT) for the diagnosis of hepatocellular carcinoma in cirrhotic candidates for liver transplantation: prevalence of radiological vascular pattern and histological correlation with liver explants. *Eur Radiolo* 2010; 20: 898–907.
104. Iannaccone R, Piacentini F, Murakami T et al. Hepatocellular carcinoma in patients with nonalcoholic fatty liver disease: helical CT and MR findings with clinical pathologic comparison. *Radiology* 2007; 243: 422–430.
105. Kim TK, Choi BI, Han JK et al. Peripheral cholangiocarcinoma of the liver: two phase Ct findings. *Radiology* 1997; 204: 539–543.
106. Vallas C, Guma A, Puig I et al. Intrahepatic cholangiocarcinoma: CT evaluation 2000. *Abdom Imaging* 2000; 25: 490–496.
107. Keogan MT, Seabourn JT, Paulson EK et al. Contrast-enhanced CT of intrahepatic and hilar cholangiocarcinoma: delay time for optimal imaging. *AJR Am J Roentgenol* 2004; 169: 1493–1499.
108. Han JK, Choi BI, Kim AY et al. Cholangiocarcinoma: pictorial essay of CT and cholangiographic findings. *Radiographics* 2002; 22: 173–187.
109. Menias OC, Venkastewar RS, Srinivasa RP et al. Mimics of cholangiocarcinoma: spectrum of disease. *Radiographics* 2008; 28: 1115–1129.
110. Nino-Murcia M, Olcott EW, Jeffrey RB Jr et al. Focal liver lesions: pattern-based classification scheme for enhancement at arterial phase. *Radiology* 2000; 215: 746–751.
111. Soyer P, Poccard M, Boudiaf M et al. Detection of hypovascular metastases at triple phase helical CT: sensitivities of phases and comparison with surgical and histopathologic findings *Radiology* 2004; 231: 413–420.
112. Miller FH, Butler FS, Hoff FL et al. Using triphasic helical CT to detect focal hepatic lesions in patient with neoplasms. *AJR Am J Roentgenol* 1998; 171: 643–649.
113. Ch'en IY, Katz DS, Jeffrey RB Jr et al. Do arterial phase improve detection and characterization of colorectal liver metastases? *J Comput Assist Tomogr* 1997; 21: 391–397.
114. Valls C, Andia E, Sanchez A et al. Hepatic metastases from colorectal cancer: preoperative detection and assessment of respectability with helical CT. *Radiology* 2001; 218: 55–60.
115. Stoupis C, Taylor HM, Paley MR et al. The rocky liver: radiologic pathologic correlation of calcified hepatic masses. *Radiographics* 1998; 18: 675–685.
116. Khalil HI, Patterson SA, Panicek DM. Hepatic lesions deemed to small to characterize at CT: prevalence and importance in women with breast cancer. *Radiology* 2005; 235: 872–878.
117. Blake SP, Wersinger K, Atkins MB, Raptopoulos V. Liver metastases from melanoma: detection with multiphasic contrast-enhanced CT. *Radiology* 1999; 213: 92–96.
118. Bressler EL, Alpern MB, Glazer GM et al. Hypervascular hepatic metastases: CT evaluation. *Radiology* 1987; 162: 49–51.
119. Ward J, Robinson PJ, Guthrie A et al. Liver metastases in candidates for hepatic resection: comparison of helical CT and gadolinium and SPIO-enhanced MR Imaging. *Radiology* 2005; 237: 170–180.

120. Del Frate C, Bazzocchi M, Mortele KJ et al. Detection of liver metastases: comparison of gadobenate dimeglumine–enhanced and ferumoxides-enhanced MR imaging examinations. *Radiology* 2002; 225(3): 766–772.
121. Petersein J, Spinazzi A, Giovagnoni A et al. Focal liver lesions: evaluation of the efficacy of gadobenate dimeglumine in MR imaging—a multicenter phase III clinical study. *Radiology* 2000 June; 215(3): 727–736.
122. Weis JC, Enzinger FM. Epithelioid hemangioendothelioma: a vascular tumor often mistaken for a carcinoma. *Cancer* 1982; 50: 970–981.
123. Keslar PJ, Buck JL, Selby DM. Infantile hemangioendothelioma revisited. *Radiographics* 1993; 13: 657–670.
124. Buetow PC, Buck JL, Ros PR, Goodman Z. Malignant vascular tumors of the liver: radiologic pathologic correlation. *Radiographics* 1994; 14: 153–166.
125. Miller JW, Dodd GD III, Federle MP, Baron RL. Epithelioid Hemangioendothelioma of the liver: imaging findings with pathologic correlation. *AJR Am J Roentgenol* 1992; 159: 53–7
126. Federle MP. *Diagnostic Imaging. Abdomen*. Salt Lake City, Utah: Amirsys, 2004.
127. Locker GY, Doroshow JH, Zwelling LA et al. The clinical features of hepatic angiosarcoma: a report a for cases and e review of the English literature. *Medicine* 1979; 58: 48–64.
128. Itai Y, Teraoka T. Angiosarcoma of the liver mimicking cavernous hemangioma on dynamic CT. *J Comput Assist Tomogr* 1989; 13: 910–912.
129. Koyama T, Fletcher JG, Johnson CD et al. Primary hepatic angiosarcoma: findings at CT and MR imaging. *Radiology* 2002; 24: 87–104.
130. Sanders ML, Botet JF, Straus DJ et al. CT of primary lymphoma of the liver. *AJR Am J Roentgenol* 1989; 152: 973–976.
131. Gazelle GS, Lee MJ, Hahan PF et al. US, CT and MRI of primary and secondary lymphoma of the liver. *J Comput Assist Tomogr* 1994; 18: 412–415.
132. Janssen HL, Garcia-Pagan JC, Elias E et al. Budd-Chiari syndrome; a review by an expert panel. *J Hepatol* 2003; 38: 364–371.
133. Bogin V, Marcos A, Shaw-Stiffel T. Budd-Chiari syndrome: in evolution. *Eur J Gastroenterol Hepatol* 2005; 17: 33–35.
134. Mathieu D, Vasile N, Menu Y et al. Budd-Chiari syndrome: dynamic CT. *Radiology* 1987; 165: 409–413.
135. Brancatelli G, federle MP, Grazioli L et al. Benign regenerative nodules in Budd-Chiari syndrome and other vascular disorders of the liver: radiologic-pathologic and clinical correlation. *Radiographics* 2002; 22: 847–862.
136. Erden A. Budd-Chiari syndrome: a review of imaging findings. *Eur J Radiolo* 2007; 61: 44–56.
137. Moulton JS, Miller BL, Dood III GD et al. Passive hepatic congestion in heart failure: CT abnormalities. *Am J Roentgenol* 1988; 151: 939–942.
138. Gore RM, Mathieu DG, White EM et al. Passive hepatic congestion: cross-sectional imaging features. *Am J Roentgenol* 1994; 162: 71–75.
139. Torabi M, Hosseinzaldeh K, Federle MP. CT of non neoplastic hepatic vascular and perfusion disorders. *Radiographics* 2008; 28: 1967–1982.
140. Kjeldsen AD, Vase P, Green A. Hereditary haemorragic telangiectasia: a population-based study of prevalence and mortality in Danish patients. *J Intern Med* 1999;245:31–33.
141. Dakeishi M, Shioya T, Wada Y et al. Genetic epidemiology of hereditary hemorragic telangiectasia in a local community in the northern part of Japan. *Hum Mutat* 2002; 19: 140–148.
142. Guttmacher AE, Marchuk DA, White RI Jr. Hereditary hemorrhagic telangiectasia. *N Engl J Med* 1995; 333: 918–924.
143. Memeo M, Stabile Ianora MM, Scardapane A et al. Hepatic involvement in hereditary hemorragic telangiectasia: CT findings. *Abdom Imaging* 2004; 29: 211–220.
144. Yu JS, Kim KW, Sung KB et al. Small arterial-portal venous shunts: cause of pseudolesions at hepatic imaging. *Radiology* 1997; 203: 737–742.
145. Kim TK, Choi BI, Han JK et al. Non tumorous arterioportal shunt mimicking hypervascular tumor in cirrhotic liver: two phase spiral CT findings. *Radiology* 1998; 208: 597–603.
146. Siddiki H, Doherty MG, Fletcher JG et al. Abdominal findings in hereditary hemorragic Telangiectasia: pictorial essay in 2D and 3D findings with isotropic multiphase CT. *Radiographics* 2008 Jan-Feb; 28(1): 171–184.
147. Holbert BL, Baron RL, Dodd GD 3rd. Hepatic infarction caused by arterial insufficiency: spectrum and evolution oc CT findings. *AJR Am J Roentgenol* 1996; 166: 815–820.
148. Brenner DA, Atcom JM. Pathogenesis of hepatic fibrosis. In: Kaplowitz, ed. *Liver and biliary disease*. Baltimore, MD: Williams & Wilkins, 1992; 118–129.
149. Waller RM, Olive TW, McCain AH et al. Computed tomography and sonography of hepatic cirrhosis and portal hypertension. *Radiology* 1984; 4: 677–715.
150. Ito K, Mitchell DG, Gabata T et al. Enlargement of hiler periportal space: a sign of early cirrhosis in MR imaging. *J Magn Reson Imag* 2000; 11: 136–140.
151. Okazaki H, Ito K, Fujita K et al. Discrimination of alcoholic from virus-induced cirrhosis on MR imaging. *Am J Roentgenology* 2000; 175: 1677–1681.
152. Harbin WP, Robert NJ, Ferrucci JT. Diagnosis of cirrhosis based on regional changes in hepatic morphology. *Radiology* 1980; 135: 273–283.
153. Terminology of nodular hepatocellular lesions. International working party. *Hepatology* 1995; 22: 983–993.
154. Coleman WB. Mechanisms of human hepatocarcinogenesis. *Curr Mol Med* 2003; 3: 573–588.
155. Bruix J, Scherman M. Management of hepatocellular carcinoma: an update. *Hepatolgoy* 2011; 53: 1020–1022.
156. Roncalli M, Roz E, Coggi G et al. The vascular profile of regenerative and dysplastic nodules of the cirrhotic liver: implications for diagnosis and classification. *Hepatology* 1999; 30: 1174–1178.
157. Choi BI, Han JK, Hong SH et al. Dysplastic nodules of the liver: imaging findings. *Abdom Imaging* 1999; 24: 250–257.

158. Park YN, Yang CP, Fernandez GJ et al. Neoangiogenesis and sinusoidal "capillarization" in dysplastic nodules of the liver. *Am J Surg Pathol* 1998; 22: 656–662.
159. Alpers DH, Sabesin M. Fatty liver: biochemical and clinical aspects. In: Shiff L, Schiff ER, eds. *Disease of the Liver*. Philadelphia, PA: JB Lippincott Co, 1982; 813.
160. Piekarsky J, Goldberg HI, Royal SA et al. Difference between liver and spleen CT numbers in the normal adult: its usefulness in predicting the presence of diffuse liver disease. *Radiology* 1980; 137: 727–729.
161. Stephens DH, Sheedy PF, Hattery RR et al. Computed tomography of the liver. *AJR Am J Roentgenol* 1977; 128: 579–590.
162. Alpern MB, Lawson TL, Foley WD et al. Focal hepatic masses and fatty infiltration detected by enhanced dynamic CT. *Radiology* 1986; 158: 45–49.
163. Hamer OW, Aguirre DA, Casola G, Sirlin CB. Imaging features of perivascular fatty infiltration of the liver: initial observations. *Radiology* 2005; 237: 159–169.
164. Bradbear RA, Bain C, Siskind V et al. Cohort study of internal malignancy in genetic hemochromatosis and other chronic nonalcoholic diseases. *J Natl Cancer Inst* 1985; 75: 81–84.
165. Chezmar JL, Nelson RL, Malko JA et al. Hepatic iron overload: diagnosis and quantification by non invasive imaging. *Gastrointest Radiol* 1990; 15: 27–31.
166. Guyader D, Gandon Y, Dugnier Y et al. Evaluation of computed tomography in the assessment of hepatic iron overload. *Gastroenterology* 1989; 97: 747–753.
167. Howard JM, Ghent CN, Carey LS et al. Diagnostic efficacy of hepatic computed tomography in the detection of iron overload. *Gastroenterology* 1983; 84: 209–215.
168. Baron RL, Gore RM. Diffuse liver disease. In: Gore RM, Levine MS, eds. *Testbook of Gastrointestinal Radiology*. 1994; 191: 123–128.
169. Boll TD, Merkel EM. Diffuse liver disease: strategies for hepatic CT and MR imaging. *Radiographics* 2009; 29: 1591–1614.
170. Mergo PJ, Ros PR, Buetow PC. Diffuse disease of the liver: radiologic-pathologic correlation. *Radiographics* 1994; 14: 1291–1307.
171. Livraghi T, Meloni F, Di Stasi M et al. Sustained complete response and complications rates after radiofrequency ablation of early hepatocellular carcinoma in cirrhosis: is resection still the treatment of choice? *Hepatology* 2008; 47: 82–89.
172. Dromain C, de Baere T, Elias D et al. Hepatic tumors treated with percutaneous radio-frequency ablation: CT and MR imaging follow up. *Radiology* 2002; 223: 255–262.
173. Lencioni R, Crocetti L. Local-regional treatment of hepatocellular carcinoma. *Radiology* 2012; 262: 43–58.
174. Caiado AHM, Blasbalg R, Marcelino ASZ et al. Complications of liver transplantation: multimodality imaging approach. *Radiographics* 2007; 27: 1401–1417.
175. Singh AK, Nachiappan AC, Verma HA et al. Postoperative imaging in liver transplantation what radiologists should know. *Radiographics* 2010; 30: 339–351.
176. Nghiem HV. Imaging of hepatic transplantation. *Radiol Clin North Am* 1998; 36(2): 429–443.
177. Ito K, Siegelman ES, Stolpen AH, Mitchell DG. MR imaging of complication after liver transplantation. *AJR Am J Roentgenol* 2000; 175: 1145–1149.
178. Quiroga S, Sebastià MC, Margarit C et al. Complication after orthotopic liver transplantation: spectrum of findings with helical CT. *Radiographics* 2001; 21: 1085–1102.

2

Gallbladder and Bile Ducts

R. Brooke Jeffrey

CONTENTS

2.1 Introduction and Clinical Overview

Disorders of the gallbladder and bile ducts are among the most prevalent diseases in the developed world, and each year in the United States, cholecystectomy is among the most common of all abdominal surgical procedures [1]. Nevertheless, a broad spectrum of inflammatory, neoplastic, traumatic, and congenital disorders may involve the gallbladder and bile ducts. A tailored diagnostic approach is required for optimal diagnosis, using a variety of noninvasive and invasive imaging techniques. Fortunately, there are multiple imaging modalities that may provide clinically important information regarding biliary abnormalities, and each has its own strengths and limitations in the assessment of biliary pathology. These modalities include ultrasound, computed tomography (CT), magnetic resonance imaging (MRI), magnetic resonance cholangiopancreatography (MRCP), biliary scintigraphy, endoscopic retrograde cholangiopancreatography (ERCP), transhepatic cholangiography, and positron emission tomography.

The most common indication for biliary imaging is the investigation of the patient with right upper quadrant (RUQ) pain and possible biliary colic or cholecystitis. In this clinical setting, ultrasound is the diagnostic imaging method of choice, due to its high accuracy in detecting gallstones and abnormal thickening of the gallbladder wall [2,3]. Similarly, in patients with jaundice, ultrasound of the bile ducts is often performed as a screening study to differentiate biliary obstruction from cholestasis related to hepatocellular disease. In many instances, however, further diagnostic information beyond that provided by screening sonography must be obtained to appropriately manage the patient. Not uncommonly, a combination of CT, biliary scintigraphy, and MRCP is used to provide additional diagnostic information, particularly in patients with common duct stones, complex cholecystitis, pericholecystic abscesses, and/or gallbladder perforation [4–7].

In patients with suspected gallbladder or biliary tract neoplasms, CT, MR, and ERCP are the mainstays of diagnosis to accurately stage the full extent of intrahepatic and extrahepatic diseases [8–10]. CT and MRI are particularly valuable in identifying liver metastases and periportal or retroperitoneal adenopathy. In patients with biliary neoplasms who have been treated surgically, CT is the mainstay for diagnosis of postoperative surveillance and identification of complications such as RUQ and perihepatic abscesses [8–10].

In patients with inflammatory diseases of the intraheptic or extrahepatic bile ducts, MRCP and ERCP play primary roles in identifying areas of strictures or associated cholangiocarcinomas [11–13]. CT may detect discontinuous areas of ductal obstruction to suggest the diagnosis, but is often inadequate to provide precise anatomic detail of the subtle ductal abnormalities [14–16].

2.2 Normal Biliary Anatomy on CT

The gallbladder is a pear-shaped organ that lies in the main lobar fissure of the liver, dividing the right and left lobes [17,18]. Anatomists and surgeons typically divide the gallbladder into four segments: fundus, body, infundibulum (Hartmann's pouch), and neck. The cystic duct containing spiral valves attaches the gallbladder to the common bile duct. In a fasting patient, the gallbladder typically contains 40–50 mL of bile, which on CT is equal attenuation to water (<10 Hounsfield units [HU]).

On CT, the normal gallbladder wall is less than 3 mm and is of uniform soft-tissue attenuation. Anatomic variations in the configuration of the gallbladder fundus are common and include a folding over the fundus, known as the Phrygian cap. Anatomic variations in the cystic duct insertion to the common duct are important surgically, particularly the long junction of the cystic duct that runs in a parallel course to the common hepatic duct, enveloped by the hepatoduodenal ligament [19]. Stones impacted in this long cystic duct may result in secondary common hepatic duct obstruction, known as the Mirizzi syndrome [20].

The blood supply to the gallbladder is derived from the cystic artery, which is a branch of the right hepatic artery. The cystic artery terminates into superficial and deep branches, which arborize into capillaries at the gallbladder fundus [21]. Because the fundus has the poorest blood supply, it is most often the site of gallbladder ischemia and perforation with prolonged cystic duct obstruction and gangrenous cholecystitis [21]. On CT, the gallbladder is normally surrounded by pericholecystic fat and omentum. An important secondary sign of gallbladder inflammation is fat stranding in the adjacent pericholecystic fat and omentum. Often, the inflamed omentum will act to "wall off" gallbladder perforations and prevent pericholecystic abscesses from leading to generalized peritonitis.

One unique anatomic feature of the gallbladder is that its wall is comprised histologically of a mucosa, lamina propria, smooth muscular layer, and perimuscular connective tissue without a discrete submucosal layer. Furthermore, there is no serosal layer at its point of attachment to the liver along the undersurface of the liver. These two anatomic features facilitate direct invasion of the liver by gallbladder carcinoma.

On CT with thin collimation (3 mm or less), the normal proximal branches of the right and left main bile ducts can be visualized and typically measure less than 2 mm [22]. The common duct on CT in the normal patient is generally less than 7 mm, but may slightly increase with age, and in patients over 50, it is not uncommon to see cross-sectional measurements of 8 mm in patients without biochemical evidence of biliary obstruction. While in most patients the dimensions of the bile duct do not change after cholecystectomy, in a small percentage of patients, the bile duct can measure normally up to 10 mm in cross-sectional diameter, most likely due to loss of intramural elastic tissue [23].

2.3 Optimization of CT Technique for Imaging of the Gallbladder and Bile Ducts

Both the imaging modality selected and precise protocol used in scanning should be tailored to the patient's clinical presentation. To optimally image the liver and biliary system, intravenous contrast is essential for state-of-the-art multi-detector CT. The rate and volume of contrast injection, however, will vary with the clinical indication. In patients whose screening ultrasound examination suggests complicated cholecystitis, CT was performed with a uniphasic acquisition during the portal venous phase [60–70 seconds following onset of intravenous injection) and at an injection rate of 2–4 cc/s, for a total of 120–150 m of nonionic contrast. Thin collimation (0.625–1.25 mm) with either a 16- or 64-slice multi-detector CT is essential to provide a high-quality diagnostic study [6,7]. The thin-collimation scans (0.625 mm) are the foundation of an isotropic data set that is ideal for the performance of sophisticated 2D and 3D reformations, including 3D volume rendering and curved planar reformations.

In patients presenting with jaundice and potential pancreaticobiliary neoplasms, however, a dedicated dual-phase acquisition is performed with both a late arterial scan of the upper abdomen (25–35 seconds after ingestion) and the standard portal venous phase [24–27]. The entire liver and upper abdomen is scanned using a rapid bolus of 4–5 cc/s of contrast injected with a power injector. The arterial-phase acquisition is particularly useful to opacify the hepatic and peripancreatic vasculature to identify hypervascular pancreatic neoplasms

such as neuroendocrine tumors and to demonstrate hypervascular liver metastasis. Portal venous phase acquisitions are essential to identify hypovascular liver metastasis, such as with ductal adenocarcinoma, and venous encasement or occlusion with resultant collateral varices [24,25].

Scirrhous lesions such as cholangiocarcinomas characteristically demonstrate delayed retention of intravenous contrast. A triphasic study comprising late arterial, portal venous, and delayed acquisition is performed in these patients. Delayed imaging at approximately 10 minutes after the onset of intravenous injection is particularly valuable in demonstrating progressive enhancement of intrahepatic extension of a cholangiocarcinoma [24]. This late retention of contrast in areas of intrahepatic extension is thought to be related to the slow diffusion of contrast into the tumor's interstitium and surrounding fibrous tissue [25].

2.4 Pathology of the Gallbladder and Bile Ducts

2.4.1 Calculus Disease

Cholelithiasis is endemic in the Western world and its incidence among adults increases with age. There are significant gender differences, and it is estimated that 20% of women and 8% of men over the age of 40 have gallstones [1]. Overall, it is estimated that 25 million individuals have gallstones in the United States [1].

Sonography is the imaging method of choice to detect gallstones and has been reported to have an accuracy of 96% [26,27]. CT appears to be substantially less sensitive than sonography, particularly for the identification of predominantly cholesterol stones, and has been reported to have a sensitivity of only 75% [6,28,29,30]. Gallstones on CT have a variable size and appearance, largely due to their variable composition of cholesterol, calcium and bilirubin salts, as well as bile acids, fatty acids, and inorganic salts [29]. Gallstones may have a calcified rim, may contain gas, or be of low attenuation on CT. Cholesterol stones may not be visible on CT (Figures 2.1 through 2.3). However, in patients with higher-attenuation biliary sludge, cholesterol stones may be identified as low attenuation, rounded or faceted lesions within the gallbladder. Degeneration of stones with nitrogen gas release that collects in central fissures may result in the "Mercedes Benz" sign, which can be readily appreciated on CT. Overall, because of its lower sensitivity and associated radiation, CT is generally not employed as a primary imaging modality for detection of gallstones.

FOCUS POINTS: VARIABLE CT APPEARANCE OF GALLSTONES

- Pure cholesterol stones invisible in 25% of patients
- Predominantly cholesterol stones may be lower attenuation than biliary sludge
- Gallstones may have homogeneous or rim calcification
- Mixed composition or pigment stones may be of soft-tissue density
- Gas with stones results in "Mercedes Benz" sign

In addition to stones, both sonography and CT may detect viscous bile related to cholestasis, also referred to as sludge (Figure 2.4). Sludge forms when there is precipitation of calcium bilirubinate and cholesterol crystals from a supersaturated solution of bile. Invariably this is related to stasis of the biliary tree in patients who experience prolonged fasting or in patients receiving intravenous total parenteral nutrition who lack a cholecystokinin stimulus to empty their gallbladder. Sludge may result in a fluid–fluid level within the gallbladder, or aggregation of sludge may result in "tumefactive sludge," which appears as an avascular soft-tissue mass [30]. On CT, sludge appears higher than water density depending on the degree of calcium bilirubinate admixture within the sludge and is often greater than 15 HU [6].

Choledocholithiasis in the Western world is almost entirely related to passage of gallstones into the cystic duct and common bile duct. In some patients, this may be entirely symptomatic; however, in other patients it may lead to significant complications such as bacterial cholangitis and/or gallstone pancreatitis. Unlike stones in the gallbladder, stones within the common duct are seen far less frequently with ultrasound, with reported sensitivities ranging from 20% to 75% [31,32]. CT has only slightly higher sensitivity, and thus, if common duct stones are suspected, either MRCP or direct ERCP should be performed [33,34]. It should be noted that small stones may not result in significant biochemical abnormalities or abnormal liver function tests; thus, small stones within the common duct may be entirely asymptomatic [34]. In general, if common duct stones are suspected clinically, unenhanced CT appears to have a higher sensitivity, as the stones appear to be slightly higher in attenuation than adjacent bile (Figure 2.2). Common duct stones may have either a "rim" sign configuration, a "crescent" sign (Figure 2.3), or appear as focal areas of discrete hyperattenuation, particularly on noncontrast scans [33,34]. Contrast-enhanced CT

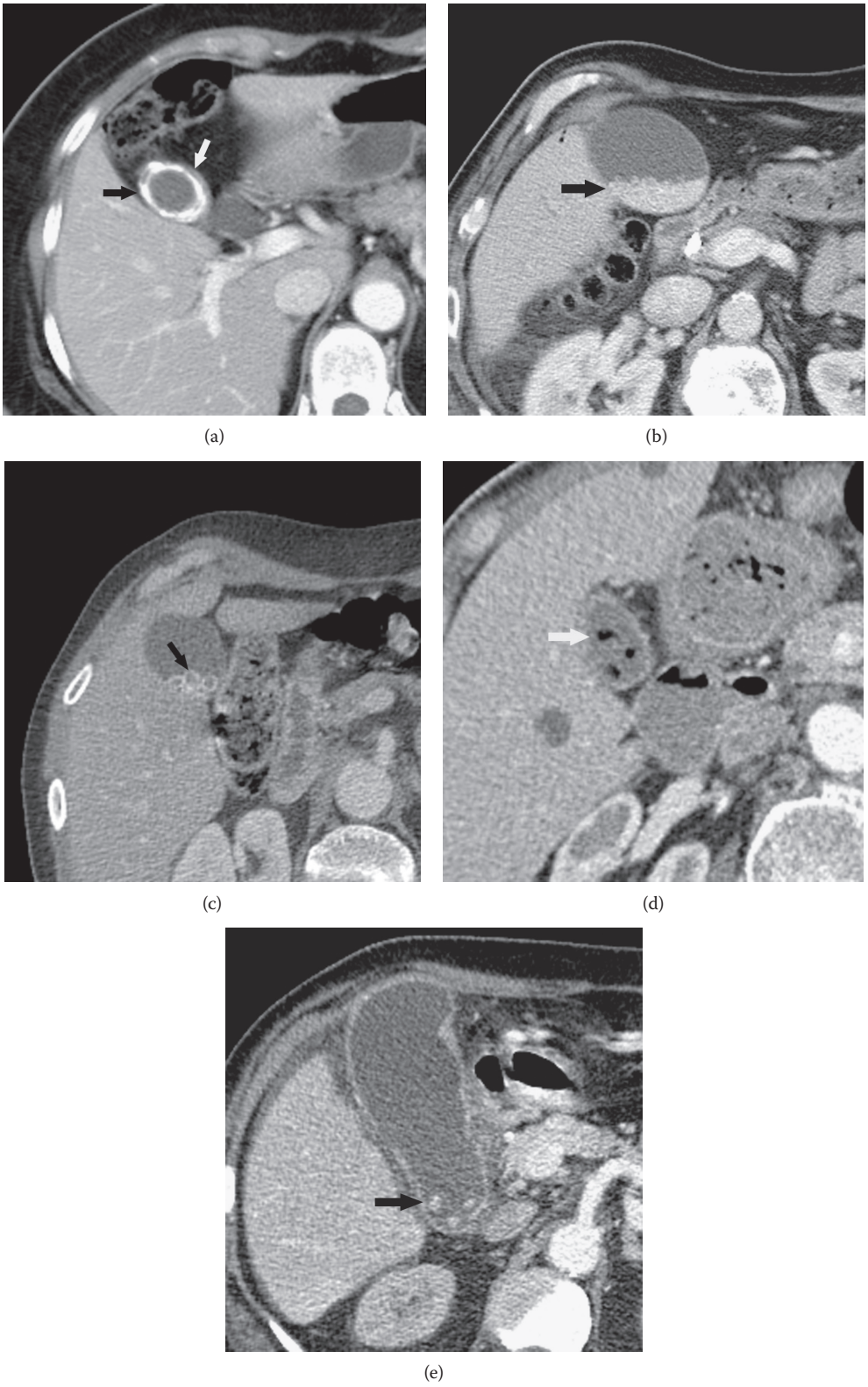

FIGURE 2.1
Variable CT appearance of gallstones. (a) Note large gallstone with calcified peripheral rim (black arrow). Patient had chronic cholecystitis with completely collapsed gallbladder (white arrow = gallbladder wall). (b) Gallstones appear as layer of calcified microliths. Note high-attenuation foci layering dependently in gallbladder from small, calcified stones (arrow). (c) Multiple small, rim-like calcified stones in gallbladder (arrow). (d) Multiple gas-containing stones are identified as low-attenuation foci within gallbladder (arrow). (e) Multiple small, soft-tissue attenuation stones (arrow) are identified in dependent portion of distended gallbladder.

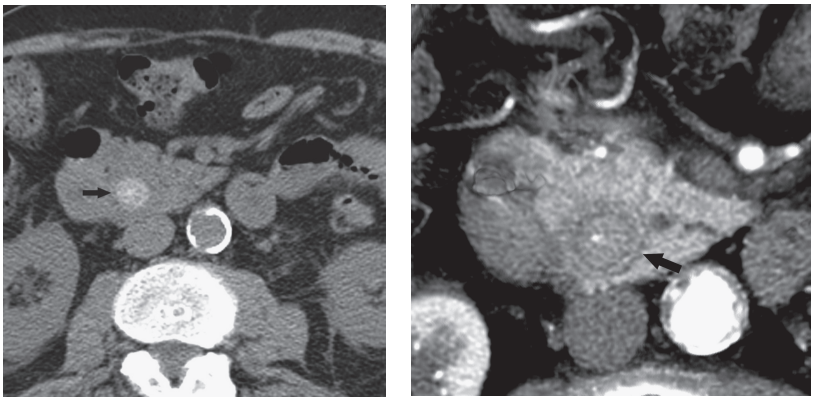

(a) (b)

FIGURE 2.2
Distal common bile duct stone. (a) Noncontrast scan demonstrating high-attenuation stone in distal common bile duct (arrow). (b) Following contrast enhancement stone appears to be of soft-tissue attenuation relative to pancreas, with high-attenuation peripheral rim (arrow) in distal common bile duct.

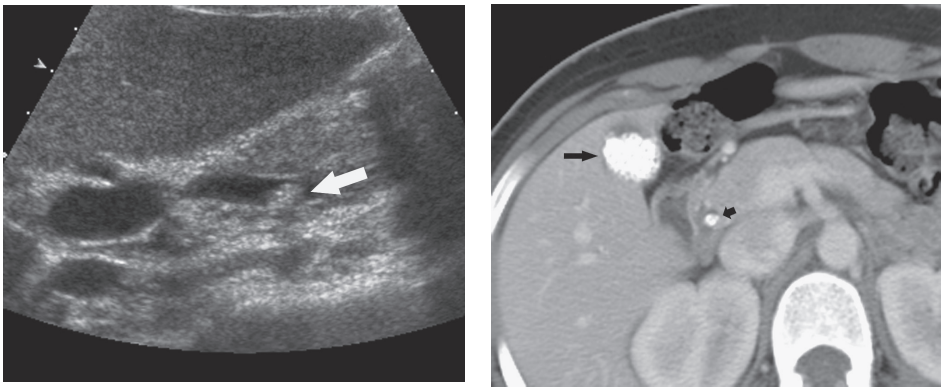

(a) (b)

FIGURE 2.3
Calcified common bile duct stone. (a) Parasagittal sonogram demonstrating common duct stone (arrow). (b) Note on CT multiple calcified gallstones (long black arrow) and calcified distal common duct stone (short black arrow).

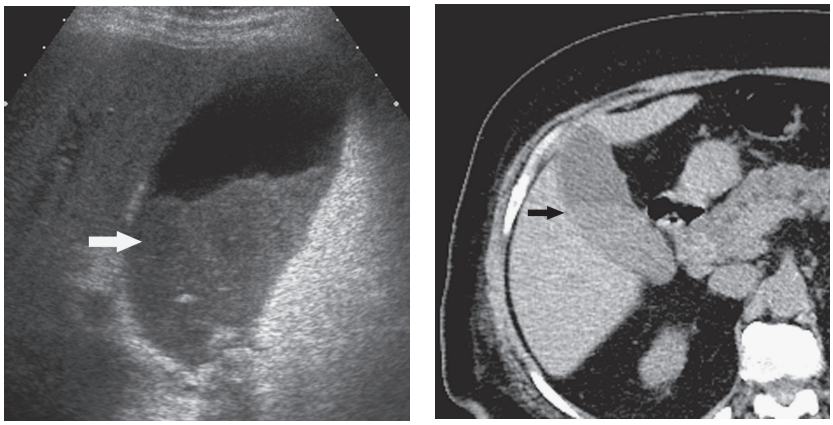

(a) (b)

FIGURE 2.4
Gallbladder sludge on ultrasound and CT. (a) Sagittal sonogram of gallbladder demonstrating layer of particulate debris in dependent portion of gallbladder, representing sludge (arrow). (b) Noncontrast CT in same patient demonstrating higher-attenuation sludge layering dependently in gallbladder (arrow).